U. S. DEPARTMENT OF THE INTERIOR
GEOLOGICAL SURVEY

MICROCRACK POPULATIONS ASSOCIATED WITH A PROPAGATING SHEAR FRACTURE IN GRANITE

By
Diane E. Moore

Open-File Report 93-245

Menlo Park, CA 94025
1993

ABSTRACT

Maps and summary tables are presented of microcracks generated during a brittle faulting experiment on Westerly granite. Granite located well away from the shear fracture in the stressed sample contains twice the crack density of the undeformed granite, and the stress-induced microcracks of the far-field area have a roughly axial orientation consistent with tensile cracks formed in response to loading. Microcrack densities increase markedly in the process zone in front of the fracture tip, and at the tip the densities are over an order of magnitude higher than in the undeformed rock. Microcracks generated within the process zone are predominantly tensile cracks that reflect the stress fields associated with the shear fracture, but some cracks form in response to the physical requirements of extending the fracture. The orientations found for the total crack populations also hold for the grain-boundary and intragranular cracks considered separately. The largest number of cracks and the smallest average crack length were found in the process zone immediately in front of the fracture tip.

Grain-boundary cracks comprise about half the microcrack population of the undeformed granite but only a small proportion of the highly cracked areas in the process zone and adjacent to the shear fracture. The grain-boundary cracks are nevertheless significant in the stressed sample in providing a connected network of cracks. Microcracking in the undeformed granite sample is highly concentrated within and along the boundaries of quartz. Near the shear fracture, intragranular cracks are slightly concentrated in K-feldspar but grain-boundary cracks remain most closely associated with quartz. Comparison of the crack and mineral maps reveals marked crystal-to-crystal variations in crack density that are caused by varying crystallographic orientations relative to the imposed stress fields.

INTRODUCTION

A reconnaissance study of microcracking associated with a developing shear fracture in Westerly granite has been conducted. Preliminary results of this investigation are presented in Moore and Lockner (in preparation). Because of space limitations, only selected data could be included in that paper. The main purpose of this report is to present all of the maps and tables from the investigation, to serve as a data base for Moore and Lockner (in preparation) and for any future papers on this topic. Because this is one of the few studies to date employing direct measurements of crack lengths and orientations, the crack maps are of particular significance in showing the actual distributions of microcracks at various positions around the fracture.

The shear fracture examined in this study comes from a cylinder of Westerly granite, 7.6 cm in diameter and 19.1 cm long, that was used in an experiment at 50 MPa confining pressure in which acoustic emission events were recorded (sample G2 of Lockner et al., 1992a). The shear fracture that formed during the experiment propagated at a low angle to the cylinder axis (about 10° over much of its length, but at larger angles near the point of nucleation), and it ceased to propagate about 3 cm before the end of the cylinder (Figure 1). This sample therefore affords the unusual opportunity to examine the rock in front of the fracture tip, to identify the means by which cracks coalesce to form a through-going fracture.

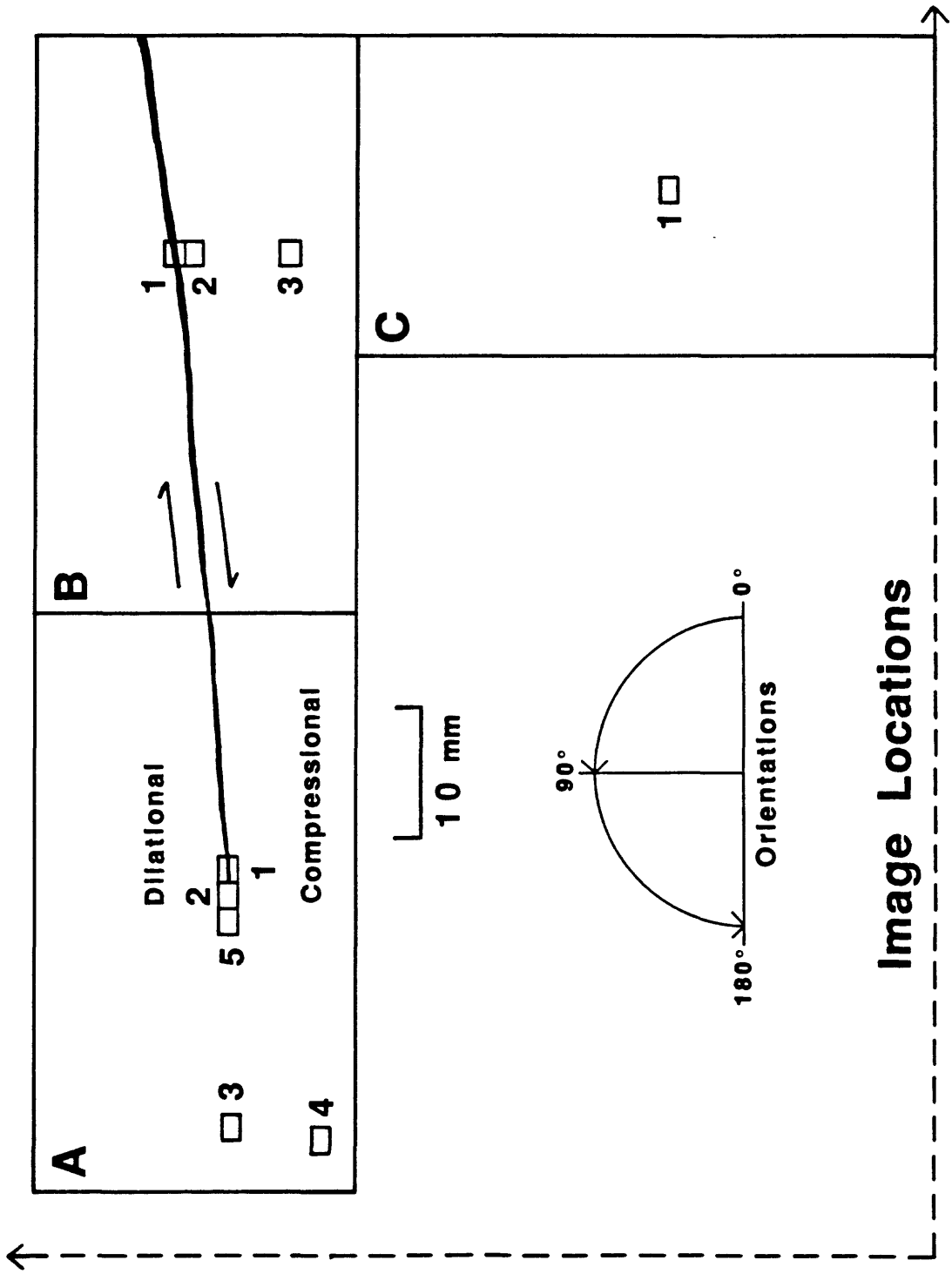

Figure 1. Sample locaties in the large, faulted cylinder, and convention for reporting microcrack orientations. The cylinder was cut in half parallel to the cylinder axis and perpendicular to the fault trace; the dashed lines indicate part of the outline of the halved cylinder. Three polished thin sections, labelled A, B, and C, contain the final 70 mm of the shear fracture, the process zone in front of the fracture tip, and a traverse to one side of the cylinder. For right-lateral shear, the area above this part of the fracture is in a dilational quadrant, and the area below the fracture is in a compressional quadrant.

The acoustic emission results (Lockner et al., 1992a) suggest that the microcracking generated during the experiment can be separated into two stages (Figure 2). During initial loading of the sample, microcracking was distributed throughout the cylinder. After the shear fracture formed, the microcracking became concentrated in a process zone in front of the fracture tip. The process zone migrated across the cylinder along with the propagating fracture. Previous studies (e.g., Hadley, 1976; Tapponnier and Brace, 1976; Kranz, 1979; Wong, 1982; Howarth, 1987) have shown that the stress-induced cracks generated prior to sample failure are principally tensile cracks that have a roughly axial orientation (Figure 2a). If the microcracks generated in the process zone are also predominantly tensile cracks, their orientations should reflect the stress fields associated with the shear fracture, as illustrated in Figure 2b. The changes in orientation of the maximum principal stress around the fracture tip are taken from Pollard and Segall (1987). A major goal of this study was to determine whether or not the actual microcrack orientations in the granite cylinder corresponded to the proposed orientations of Figure 2.

PROCEDURES

The granite cylinder used in the acoustic emission experiment was cut in half parallel to the cylinder axis and perpendicular to the shear fracture. Three polished thin sections were made from one of the half cylinders, as shown in Figure 1. Nine reflected-light images from the three sections were scanned directly into a computer from a microscope. Each image covered an area 2.0 x 1.5 mm in size. Sample numbers assigned to the images combine the letter designation of the thin section with the number of the image in each section: e.g., A-3, B-1. An additional image of the undeformed Westerly granite was collected from a small cylinder that was cored in the same direction into the granite block as the larger cylinder; this image was labelled WPS. Moore and Lockner (in preparation) determined that the 90° orientation of each image (Figure 1) lies within the horizontal plane (ground level) at Westerly quarry.

Open cracks were identified with the microscope and their lengths and orientations were measured on the calibrated computer image using the NIH image-analysis program IMAGE, which is in the public domain. The microcrack data were exported to a spreadsheet program for storage and manipulation. Grain-boundary and intragranular cracks were measured separately; the minerals bounding or containing the cracks were all identified. In cases where a long microcrack consisted of a series of smaller, linked cracks, the individual small cracks were measured and counted separately. Most bent cracks clearly consisted of two cracks that intersected at the bend, but a few bent or curved cracks had no obvious subdivisions. Similarly, some grain-boundary cracks appeared to be continuously open around the corners of a crystal. Hadley (1976) subdivided microcracks that changed orientation by more than 20°, and the same practice was adopted here for the apparently continuous but curved or bent cracks. The reported orientation of a given crack is the average across its length. All of the microcrack data presented in the tables and figures are normalized to a $1 mm^2$ sample area. Repeated measurements of a set of cracks 350-450 μm in length yielded error estimates of less than ±2% for crack lengths and ±1° for their orientations. The error probably increases somewhat for microcracks less than about 20 μm long.

Normal operating magnification under the microscope was 312x; occasional checks were made at 500x. At these magnifications, the smallest resolvable microcracks were about 3 μm long. This is also the minimum crack length that could be measured for the image size scanned into the computer, because the calibrated length of 1 pixel in these images is 3.13 μm. The

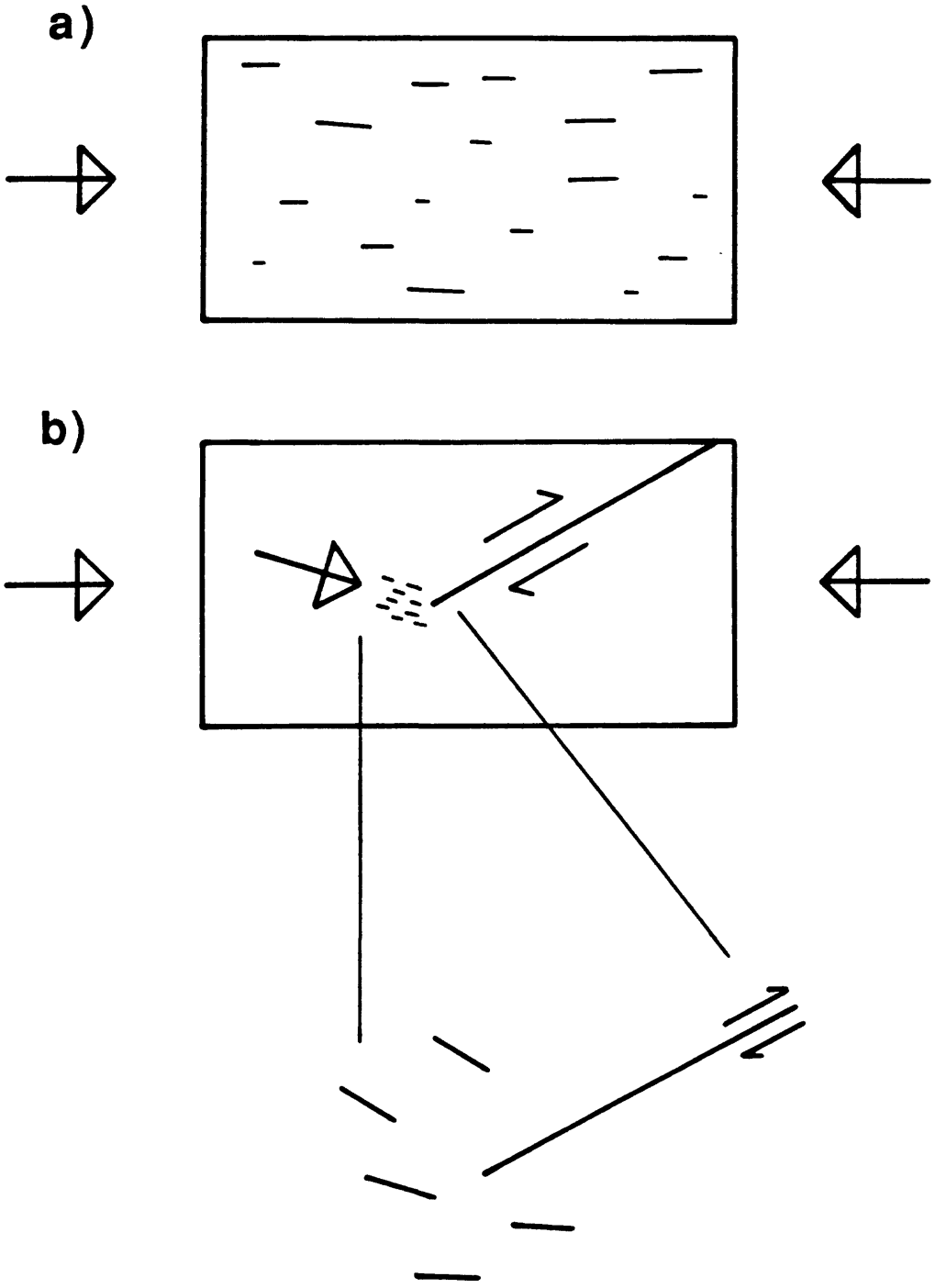

Figure 2. Acoustic emission events recorded during the experiment (Lockner et al., 1992a) indicate that microcracking can be separated into 2 stages: a) an early stage of generally distributed cracking prior to fault formation; and b) a later stage, subsequent to fault initiation, in which cracking was localized in the process zone located directly in front of the fault tip. Any tensile cracks associated with the 2 stages would have the orientations indicated in a) and b). As suggested by the calculated stress fields of Pollard and Segall (1987), tensile cracks on the dilational side of the fault should make a larger angle to the fault plane than those on the compressional side (Figure 1). For a fault strike of 10°, the average orientation of the second-stage microcracks would be 145° (see Figure 1).

length limitations need to be kept in mind, particularly with respect to the crack counts. However, omission of any short cracks in the samples should have only a small effect on the total crack lengths (Wong, 1985).

MINERAL ABUNDANCES AND MAPS

The effects of mineralogy on microcrack populations in both stressed and unstressed granitic rocks have been described in qualitative or semi-quantitative terms (e.g., Peng and Johnson, 1972; Sprunt and Brace, 1974; Tapponnier and Brace, 1976; Kranz, 1979; Wong, 1982; Fredrich and Wong, 1986), but so far no truly quantitative data have been presented. One of the goals of this study was to obtain such quantitative data for Westerly granite. To achieve this purpose, the igneous mineral assemblage contained in each image was identified, and the crystal outlines determined (Figures 3-12). The igneous mineral assemblage consists principally of quartz, plagioclase, and K-feldspar (probably both microcline and orthoclase, which are grouped together in this report), with some biotite and accessory minerals, principally opaques (magnetite and minor pyrite), zircon, apatite, allanite, and sphene. Secondary replacement minerals such as calcite and chlorite were not included in the igneous assemblage (although any cracks contained in the secondary minerals were added to the measurements of total crack density). Similarly, tiny accessory minerals that occur as inclusions in other, larger crystals were not marked, because of their insignificant area and because they are completely isolated within the host crystal and so do not contribute to the network of connected grain boundaries. Muscovite was a special case. Most of the muscovite occurs as small flakes within plagioclase crystals and is obviously a replacement mineral. Such mica flakes were not included in the igneous assemblage. However, some relatively large, separate crystals of muscovite in images A-1 and B-3 were added to the maps.

Traditionally, mineral proportions (modes) of rock samples have been obtained by means of point counts, but for this study the area of each crystal in the mineral maps could also be determined with the image-analysis program. Mineral proportions for each image were obtained using both methods, to compare the results (Table 1). The summed crystal area for a given image was within ±1% of the true area. The sums were adjusted to the actual area of the image before the mineral proportions were calculated. The point counts for the 10 images were made using a relatively coarse 18 x 13 grid that yielded 234 counts per image. Both sets of measurements were made on the mineral maps (Figures 3-12).

The individual point counts gave generally good results for the most abundant minerals, particularly plagioclase and quartz, but the variations were significantly larger for the less abundant minerals. A finer grid spacing for the point counts would improve the correspondence to the area measurements. The average of the 10 images obtained by the 2 methods was almost identical, indicating that using the coarse grid over a larger sample area would also improve the modes obtained from the point counts. The actual time required to make the point counts and the area measurements on the images was roughly the same, but the area measurements are not practical for most modal analyses because of the need to pre-determine the mineral outlines.

A general mode for the Westerly stock was obtained from point counts of 13 thin sections that had been prepared for other studies (Moore et al., 1983, 1987). Those counts were obtained using a uniform 1-mm grid spacing on the variably sized rock chips, which yielded

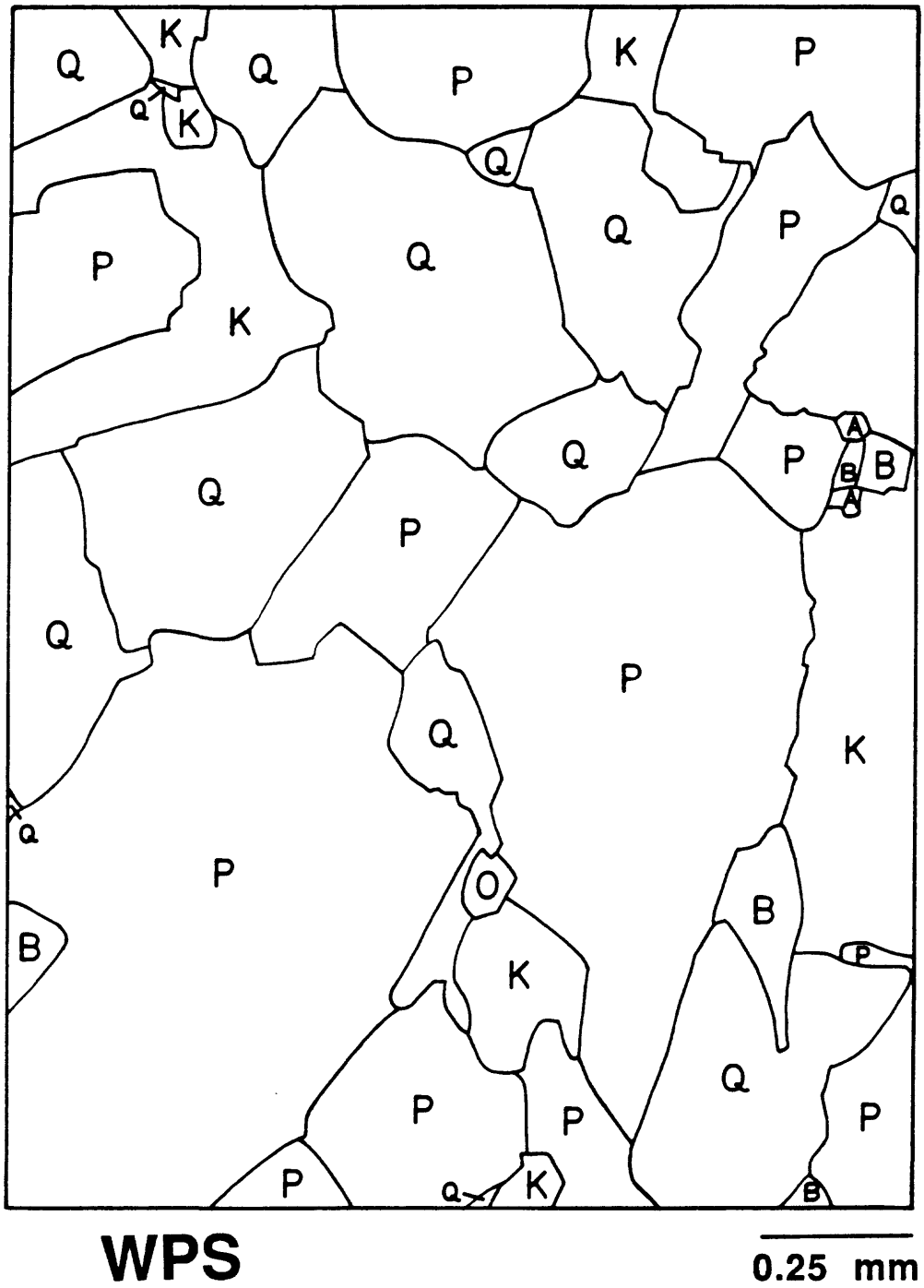

Figure 3. Mineral map of the image obtained from the undeformed sample, WPS. Mineral abbreviations used in Figures 3-12: P = plagioclase; Q = quartz; K = K-feldspar; B = biotite; O = opaques, usually magnetite; M = muscovite; A = apatite; Al = allanite; S = sphene; Z = zircon. Some of the tabular plagioclase crystals are aligned at about 50-60°. Near the upper left-hand corner is a good example of a plagioclase crystal mantled by K-feldspar.

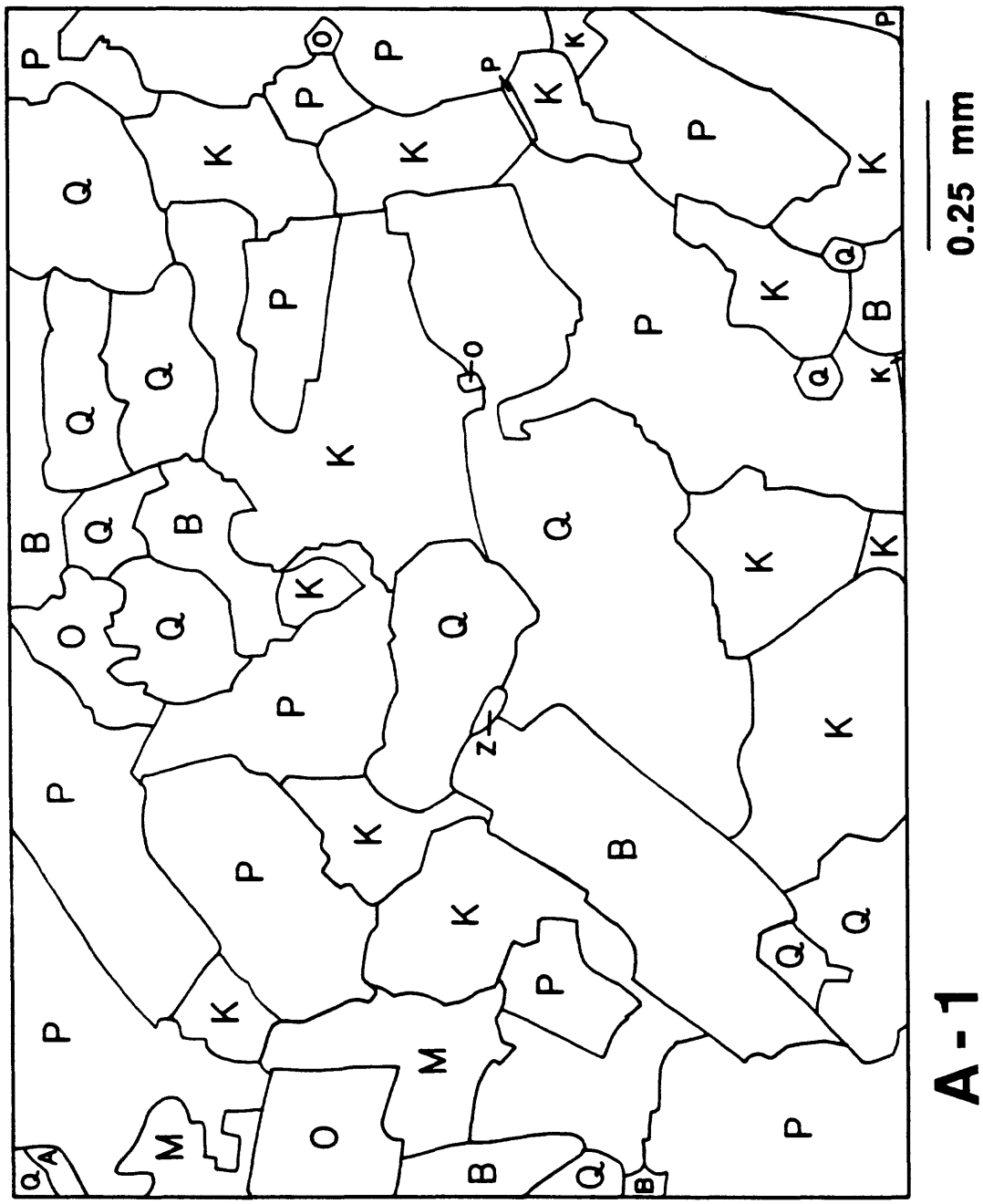

Figure 4a. Mineral map of image A-1, at the fracture tip. The crystals are relatively uniform and relatively small in size, and A-1 has the largest grain-boundary length per unit area of all 10 images. Tabular plagioclase and biotite crystals are aligned towards the upper right-hand corner.

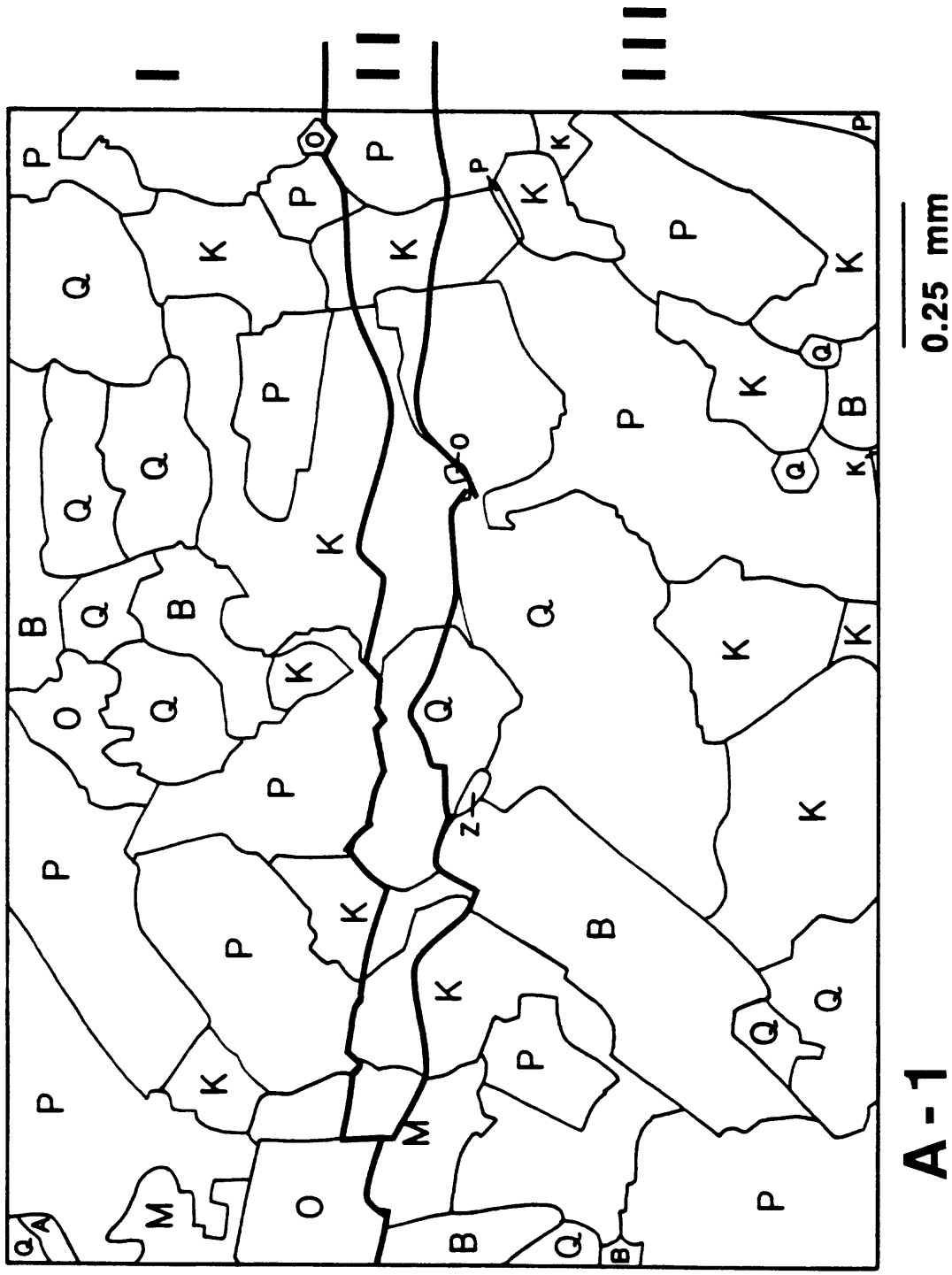

Figure 4b. Heavy lines show how the image A-1 was subdivided into a narrow zone (II) of high crack density surrounding the shear fracture, and wider zones on the dilational (I) and compressional (III) sides. The fracture stopped propagating just in front of the opaque mineral on the left edge of the image.

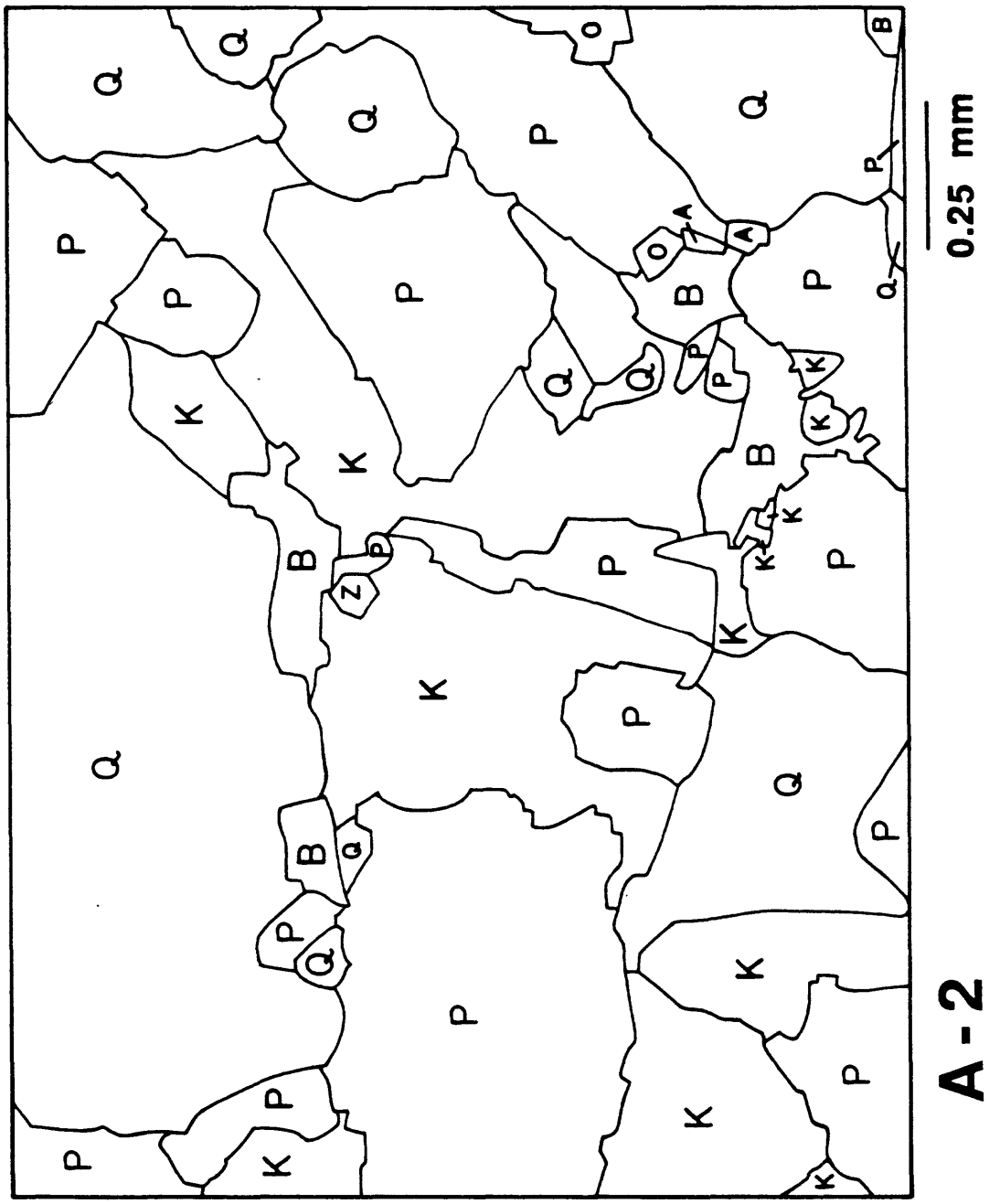

Figure 5a. Mineral map of image A-2, located directly in front of the fracture tip. The image contains a wide range of crystal sizes, but it is dominated by a few large crystals.

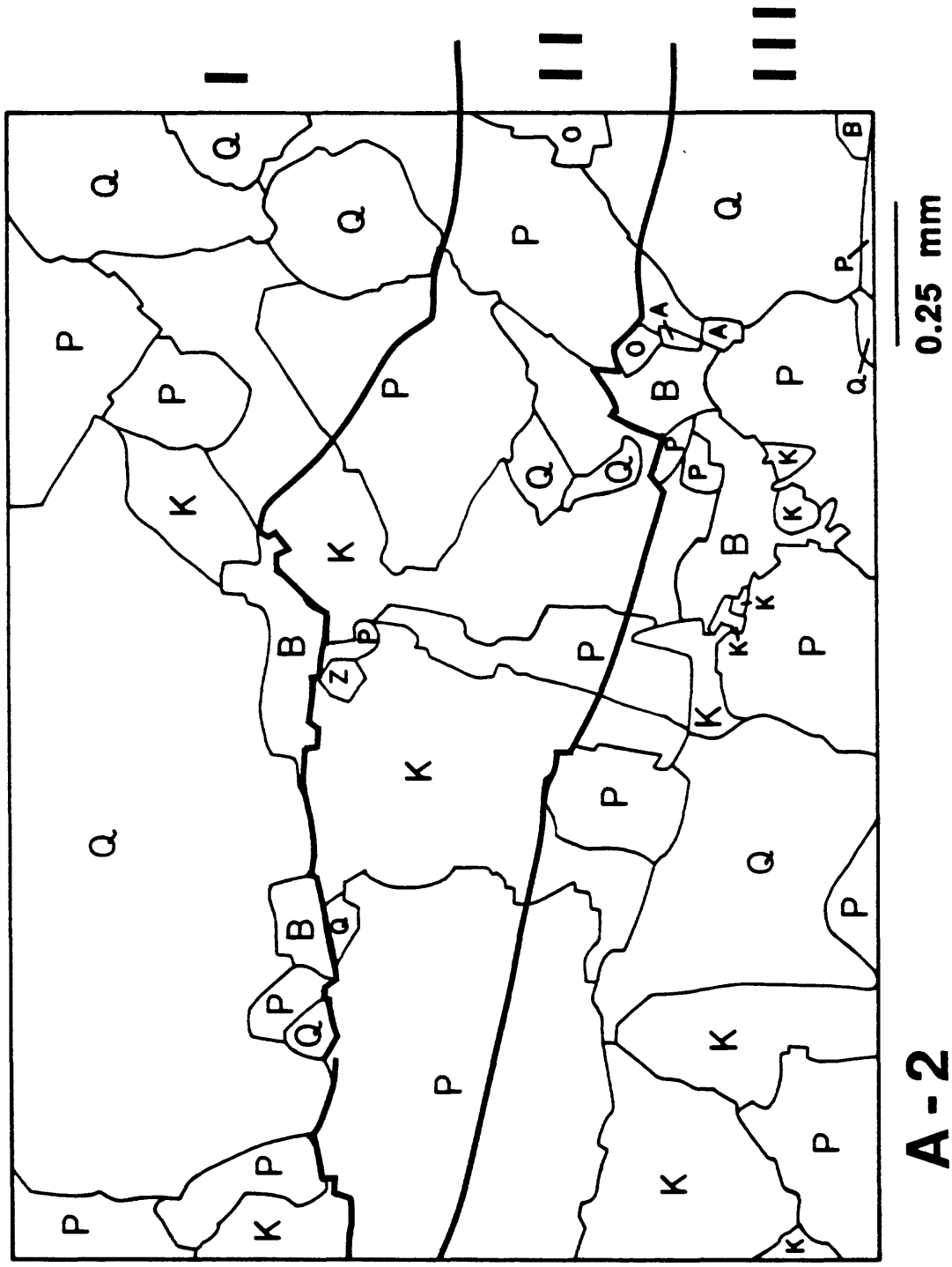

Figure 5b. The heavy lines show how the image A-2 was subdivided into a central zone (II) of higher crack density and less highly cracked zones on the dilational (I) and compressional (III) sides of the fracture. Zone II trends slightly uphill to the left, at an orientation of just over 170°.

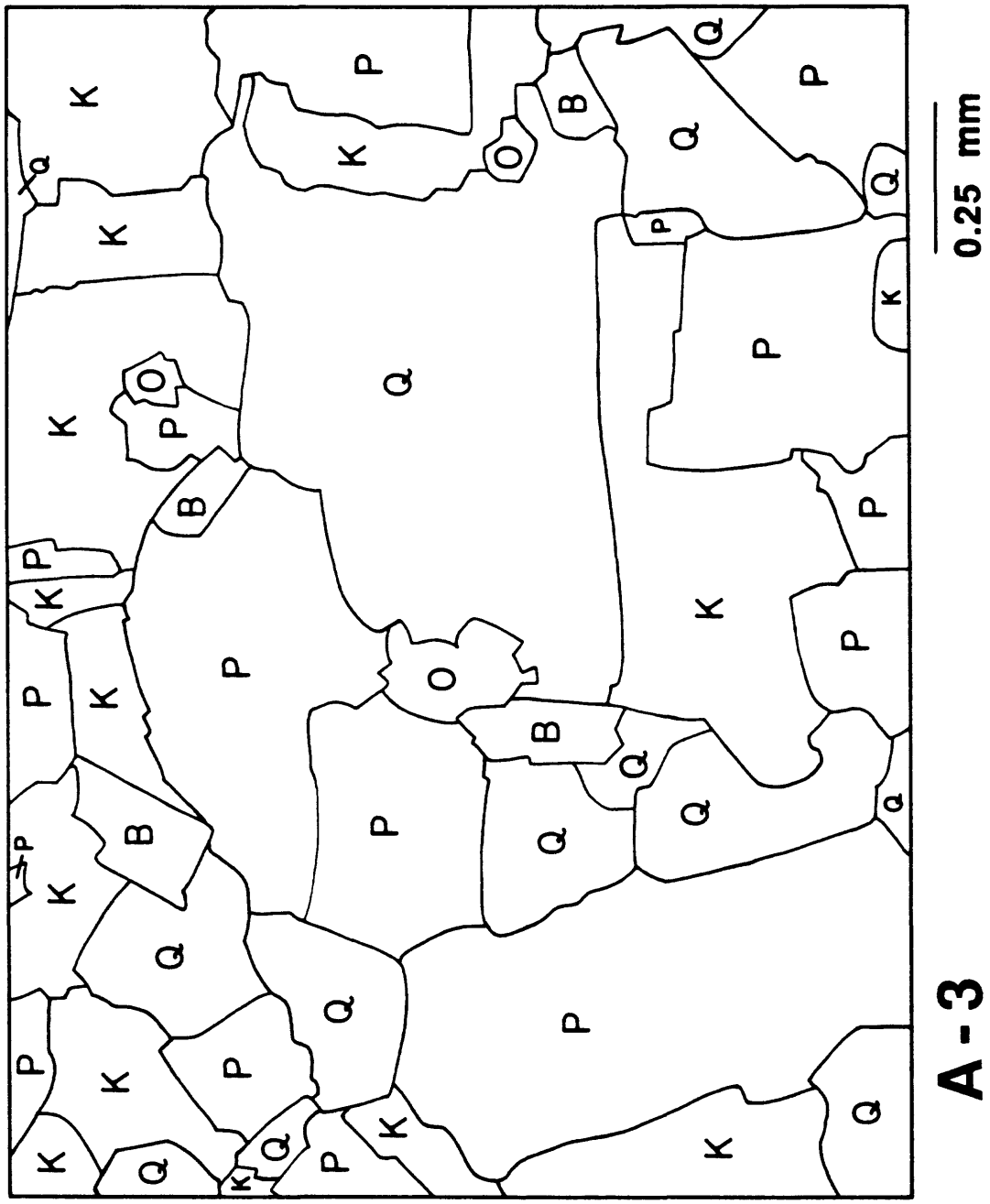

Figure 6. Mineral map of image A-3, located several millimeters in front of the fracture tip. A few large crystals of quartz and feldspar dominate the image. The right-hand side of the image has 3 good examples of plagiolcase with a mantle of K-feldspar.

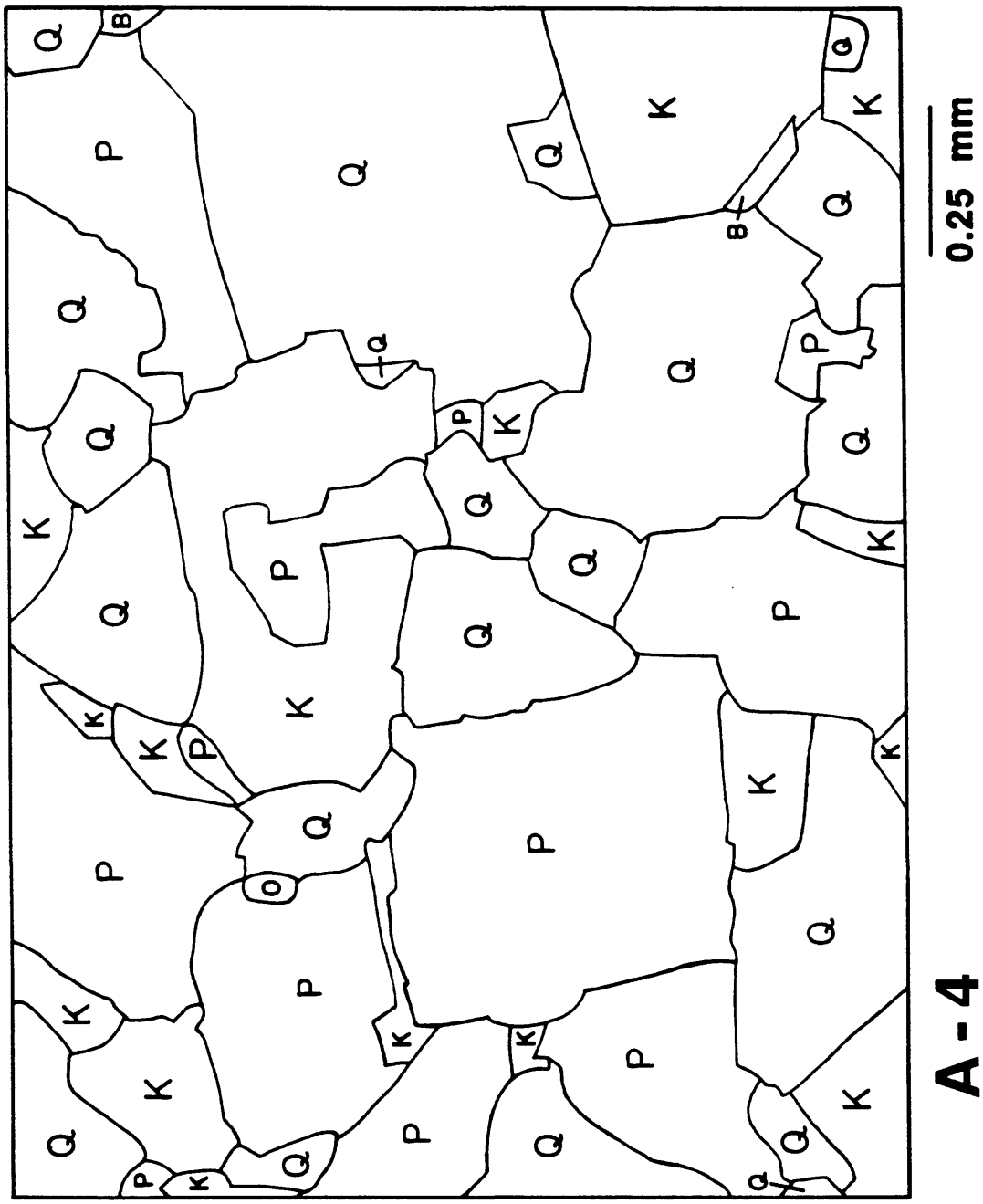

Figure 7. Mineral map of image A-4, located several mm in front and to the side of the fracture tip. An irregularly shaped plagioclase crystal in the center of the image has an extensive K-feldspar mantle.

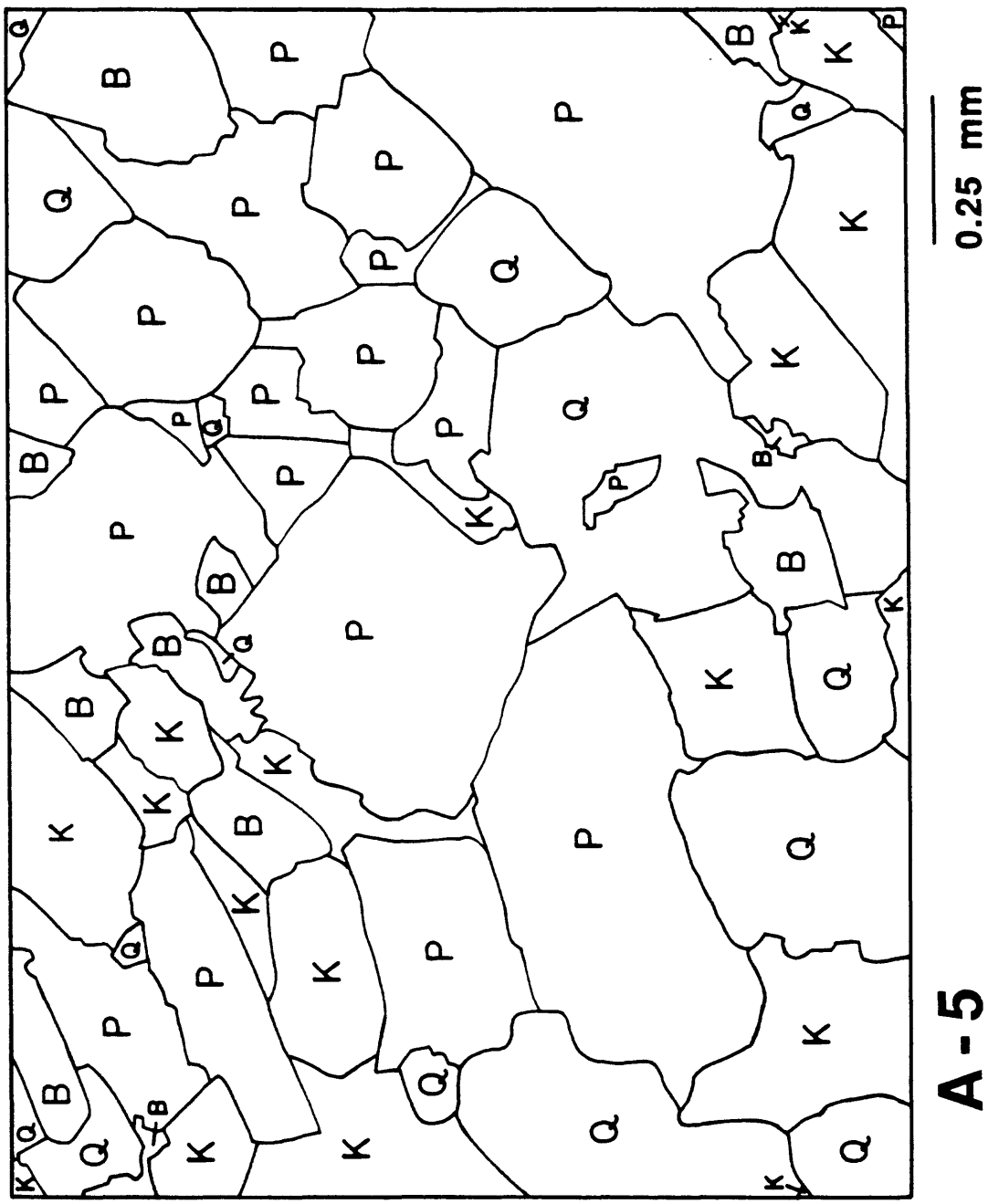

Figure 8. Mineral map of image A-5, from the process zone directly in front of A-2. This image contains many small and a few large crystals.

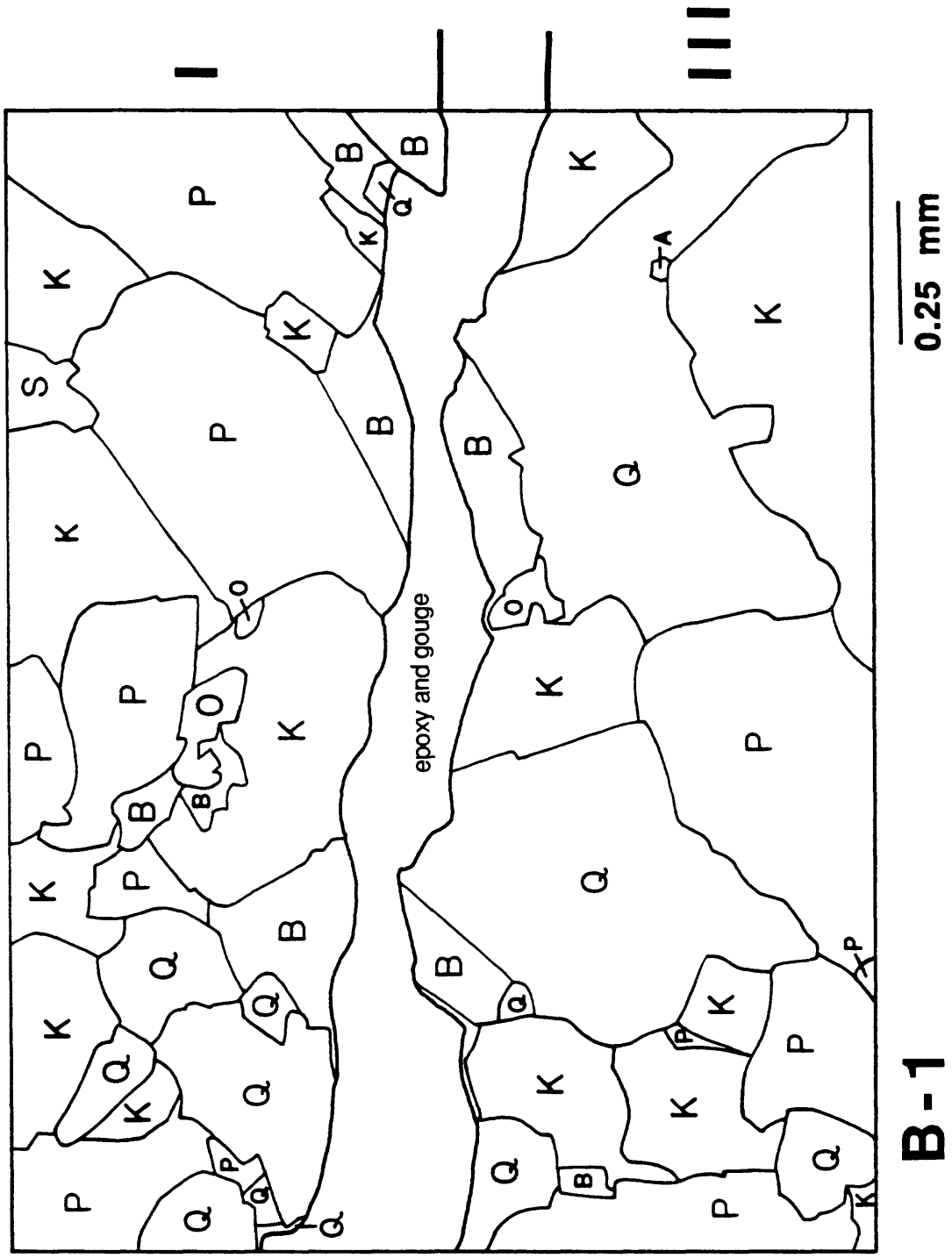

Figure 9. Mineral map of image B-1, which crosses the shear fracture several cm behind the fracture tip. The image was divided into zones on the dilational (I) and compressional (III) sides of the shear fracture. What would be zone II is a band of epoxy and highly crushed granite. Zones I and III represent the more or less intact rock adjacent to the fracture, in which individual cracks could be distinguished.

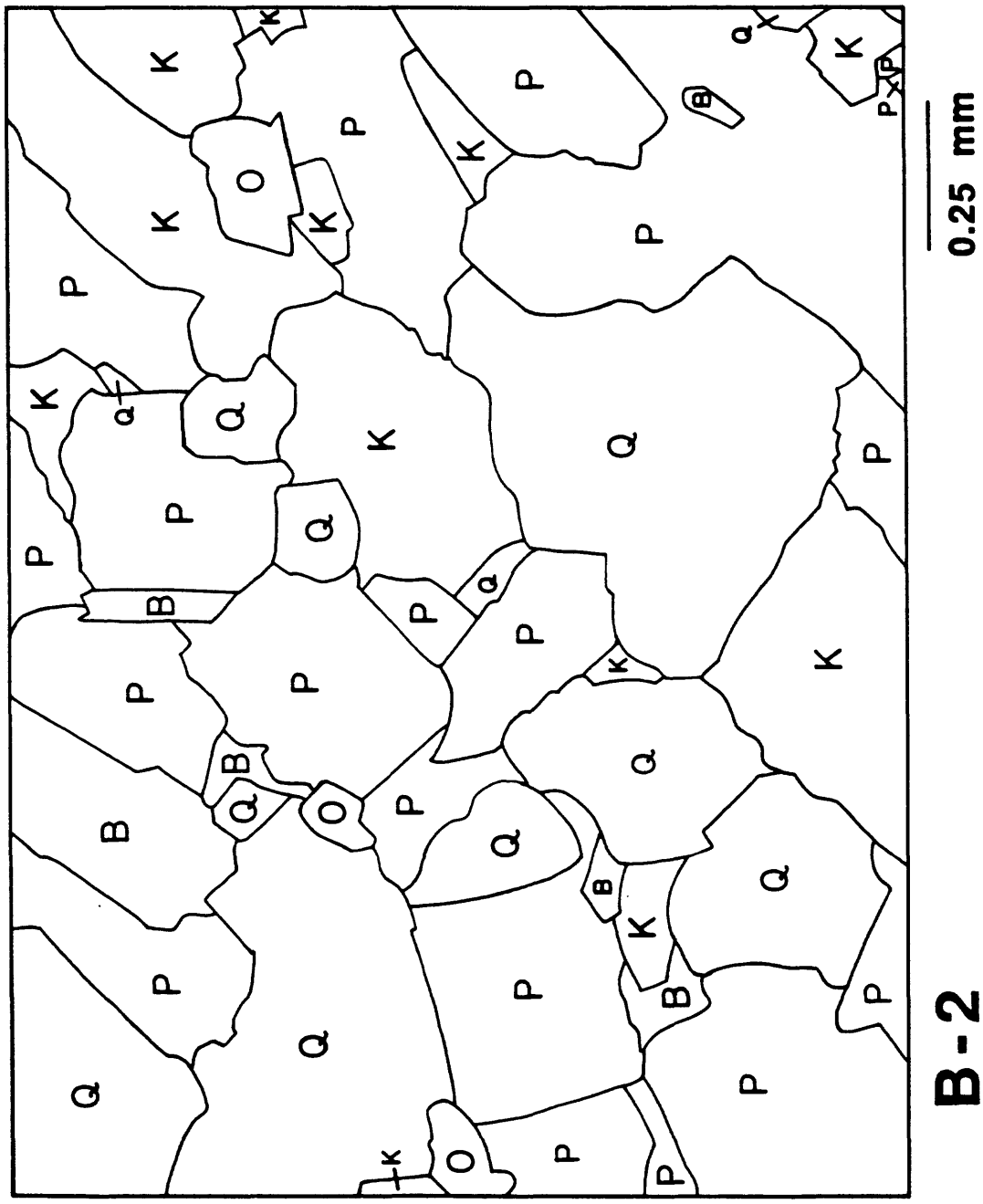

Figure 10. Mineral map of image B-2, located close to the fault on the compressional side. The image contains several aligned, tabular crystals of plagioclase and biotite.

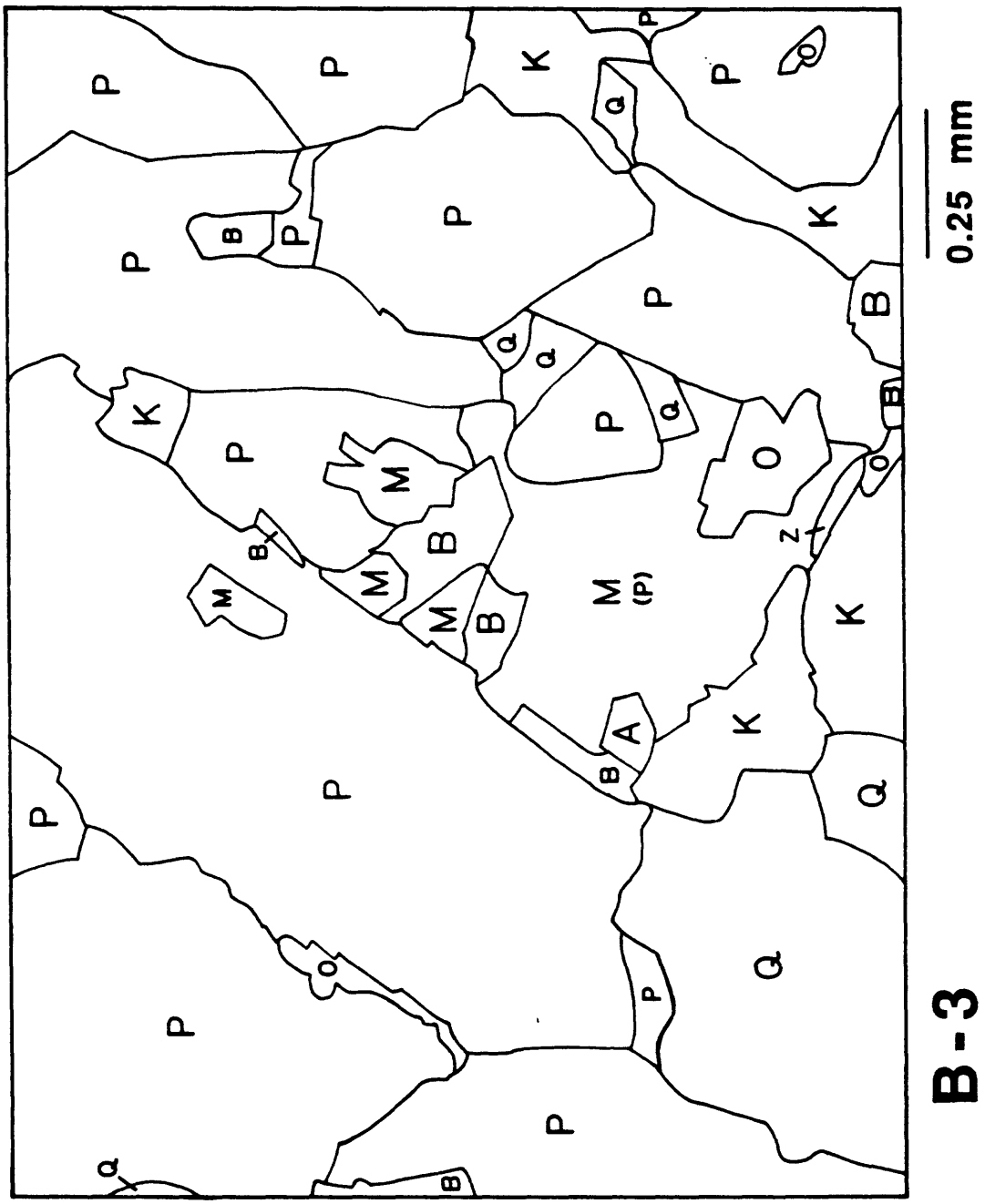

Figure 11. Mineral map of image B-3, located about 8 mm from the fault on the compressional side. This locality contains an unusually large amount of plagioclase, a few large crystals of which dominate the image.

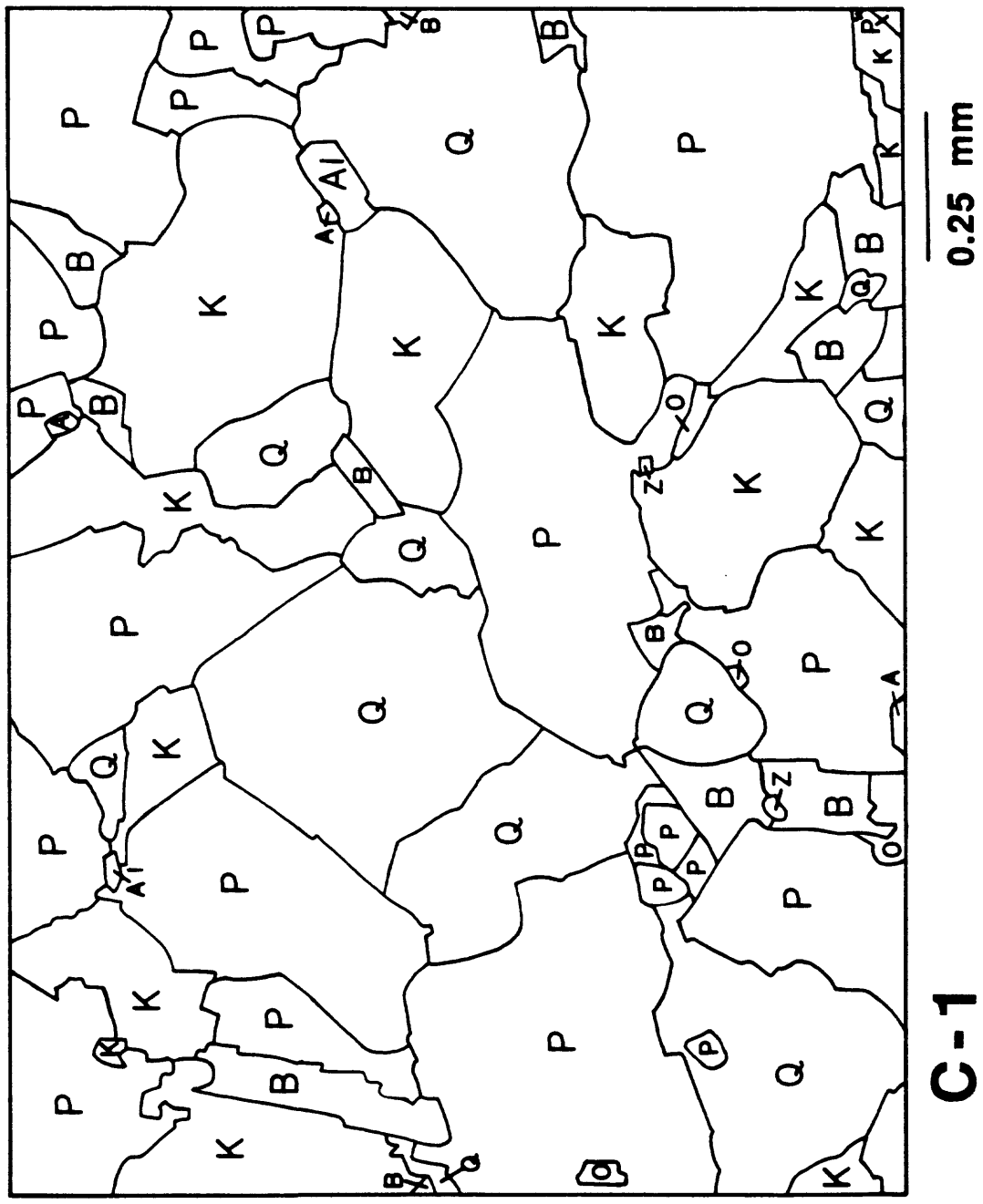

Figure 12. Mineral map of image C-1, located a few cm from the fault on the compressional side. Many small crystals contribute to the large grain-boundary length of this image.

TABLE 1.

Mineral Proportions

	by Point Count					by Area (Computer)				
	Plag	Qtz	Kspr	Biot*	Other	Plag	Qtz	Kspr	Biot*	Other
General**	41.0	25.2	26.3	6.3	1.2					
Images:										
WPS	53.0	31.2	14.5	1.3	0.0	53.7	31.3	13.0	2.0	0.0
A-1	34.2	21.4	26.5	14.1	3.8	34.7	22.3	27.7	12.0	3.3
A-2	31.6	36.8	26.9	3.4	1.3	34.3	35.3	26.7	3.0	0.7
A-3	37.2	28.6	29.5	2.6	2.1	37.7	31.0	26.7	3.0	1.6
A-4	37.6	44.8	17.1	0.5	0.0	36.0	44.0	19.3	0.7	0.0
A-5	51.7	21.4	18.8	8.1	0.0	49.0	22.1	21.2	7.7	0.0
B-1	31.8	29.2	28.8	9.2	1.0	32.6	28.8	30.4	6.6	1.6
B-2	44.9	29.9	18.4	4.7	2.1	45.3	29.7	18.3	4.7	2.0
B-3	71.4	9.4	6.4	10.7	2.1	69.7	10.0	8.0	10.0	2.3
C-1	48.3	22.2	23.1	6.0	0.4	47.7	23.3	23.0	5.3	0.7
Average	44.2	27.5	21.0	6.0	1.3	44.1	27.8	21.4	5.5	1.2

* Includes muscovite in A-1 and B-3

** Average of 13 point counts of laboratory stock

400-750 counts per thin section. Overall, the general average is very similar to the average of the 10 images obtained by either method (Table 1). The relative abundances of plagioclase and K-feldspar do differ slightly, but some variations are to be expected given the very different sample areas covered by the 2 averages. The modes of the individual images are much more variable, and image B-3, in particular, is very enriched in plagioclase compared to the average of the laboratory stock. Westerly granite is a relatively uniform, medium-grained rock, with a range in grain size of about 0.05 mm to 2 mm. For a 3 mm^2 sample area, however, this range is extreme. A few large crystals of quartz and plagioclase dominate images such as A-2 (Figure 5) and B-3 (Figure 11). The average grain size also varies from site to site; compare, for example, WPS (Figure 3) with A-1 (Figure 4). Because of these variations, such small sample areas will generally not be completely representative of the overall rock compositiom.

The mineral maps also reveal a preferred orientation defined by tabular crystals of plagioclase and flakes of biotite, trending up to the right at 40° to 70°. The alignment is best seen in WPS (Figure 3), A-1 (Figure 4), B-2 (Figure 10), and B-3 (Figure 11). This mineral fabric corresponds to the igneous flow structure that has been described at some of the Westerly quarries (Dale, 1923).

GRAIN BOUNDARIES

The grain boundaries warrant separate consideration, because they comprise a through-going network in the rock. The degree to which they are cracked will correspondingly have a significant effect on rock properties such as permeability, electrical resistivity, and seismic velocity. Tables 2 and 3 summarize the grain-boundary data for each image, relative to orientation. The total grain-boundary lengths in Table 3 are the sums of all the mineral outlines in Figures 3-12. The proportion of grain boundaries that are cracked in each image is presented in Figure 13, to illustrate the variations around the sample. Sixty percent of the grain boundaries in the undeformed sample are cracked. The percentages are the same or higher throughout the stressed sample, with the greatest degree of cracking found along the shear fracture. The results suggest an 80% ceiling to the proportion of grain boundaries that will be cracked in the stressed sample, excluding the crushed areas within the fault itself.

As described previously, the two cylinders examined in this study were cored vertically into the granite block, but their circular cross sections were not oriented relative to the sides of the block before coring. The thin sections from the two cylinders could therefore show different vertical slices through the granite blocks, and the orientations of any pre-existing, inclined cracks will vary with the direction that they are cut by the plane of the thin section. In order to ascertain whether or not the crack orientations in WPS and the stressed sample can be compared, some way of determining the relative match (or mis-match) of the thin sections must be found. The flow structure that was identified in the mineral maps provides the means of comparison.

The orientation of the tabular plagioclase crystals in WPS (Figure 3) looks to be generally similar to the fabric in some of the other mineral maps; the actual orientations can be found in Table 3. Image WPS has a local maximum of crack length at 50-60°, corresponding to the trend of the flow structure in that image. In the stressed sample, 4 images also have a maximum at 50-60°, 3 have it at 40-50°, and the other 2 at 60-70°. The results indicate some site-to-site variations in the orientation of the flow structure in the large cylinder, but the average alignment is the same as in WPS. This suggests that the orientations of the thin

TABLE 2.

Cracked Grain Boundaries
[Length (μm) per square millimeter]

Orientation	WPS	A-1	A-2	A-3	A-4	A-5	B-1	B-2	B-3	C-1
0-9°	100	642	521	547	377	198	287	289	170	434
10-19°	242	456	323	251	306	546	410	306	255	391
20-29°	172	234	108	219	349	591	314	315	128	147
30-39°	88	420	377	134	201	341	634	346	84	407
40-49°	224	294	329	387	141	999	362	293	284	374
50-59°	564	499	378	158	414	324	405	792	116	281
60-69°	297	403	171	150	351	167	238	106	497	99
70-79°	218	152	519	124	253	195	158	93	203	328
80-89°	204	267	300	329	356	221	164	252	247	294
90-99°	384	737	413	376	225	359	248	420	507	415
100-109°	156	369	259	379	360	273	379	194	292	272
110-119°	334	397	174	430	277	348	436	203	199	297
120-129°	96	129	174	153	104	349	250	32	201	263
130-139°	219	321	320	152	226	262	381	422	161	160
140-149°	55	238	386	310	181	293	167	410	153	192
150-159°	74	283	442	227	367	291	241	229	190	259
160-169°	143	412	311	68	226	270	370	331	269	179
170-179°	45	628	436	436	401	223	292	262	229	209
Sum	3615	6881	5941	4830	5115	6250	5736	5295	4185	5001

TABLE 3.

Total Grain Boundaries
[Length (μm) per square millimeter]

Orientation	WPS	A-1	A-2	A-3	A-4	A-5	B-1	B-2	B-3	C-1
0-9°	255	730	658	1017	614	241	338	396	311	725
10-19°	406	511	349	367	675	821	535	436	310	605
20-29°	303	324	162	337	374	759	374	427	266	347
30-39°	225	524	501	354	380	474	724	579	139	534
40-49°	289	535	406	529	157	1197	398	540	446	622
50-59°	713	590	536	206	458	584	630	1191	512	429
60-69°	597	740	186	300	424	195	343	170	721	202
70-79°	334	241	667	207	331	299	248	105	308	467
80-89°	398	499	481	456	476	303	232	364	491	458
90-99°	498	830	605	532	472	600	400	499	565	688
100-109°	242	485	298	538	548	374	535	402	427	436
110-119°	462	445	236	625	344	361	580	308	243	382
120-129°	237	235	190	227	152	479	364	76	274	468
130-139°	408	387	386	209	300	334	393	509	302	354
140-149°	180	321	405	390	313	405	201	451	283	606
150-159°	128	343	463	314	372	304	358	318	317	407
160-169°	255	437	431	126	285	344	503	343	401	353
170-179°	144	654	501	558	495	306	377	303	423	323
Sum	6074	8831	7461	7292	7170	8380	7533	7417	6739	8406

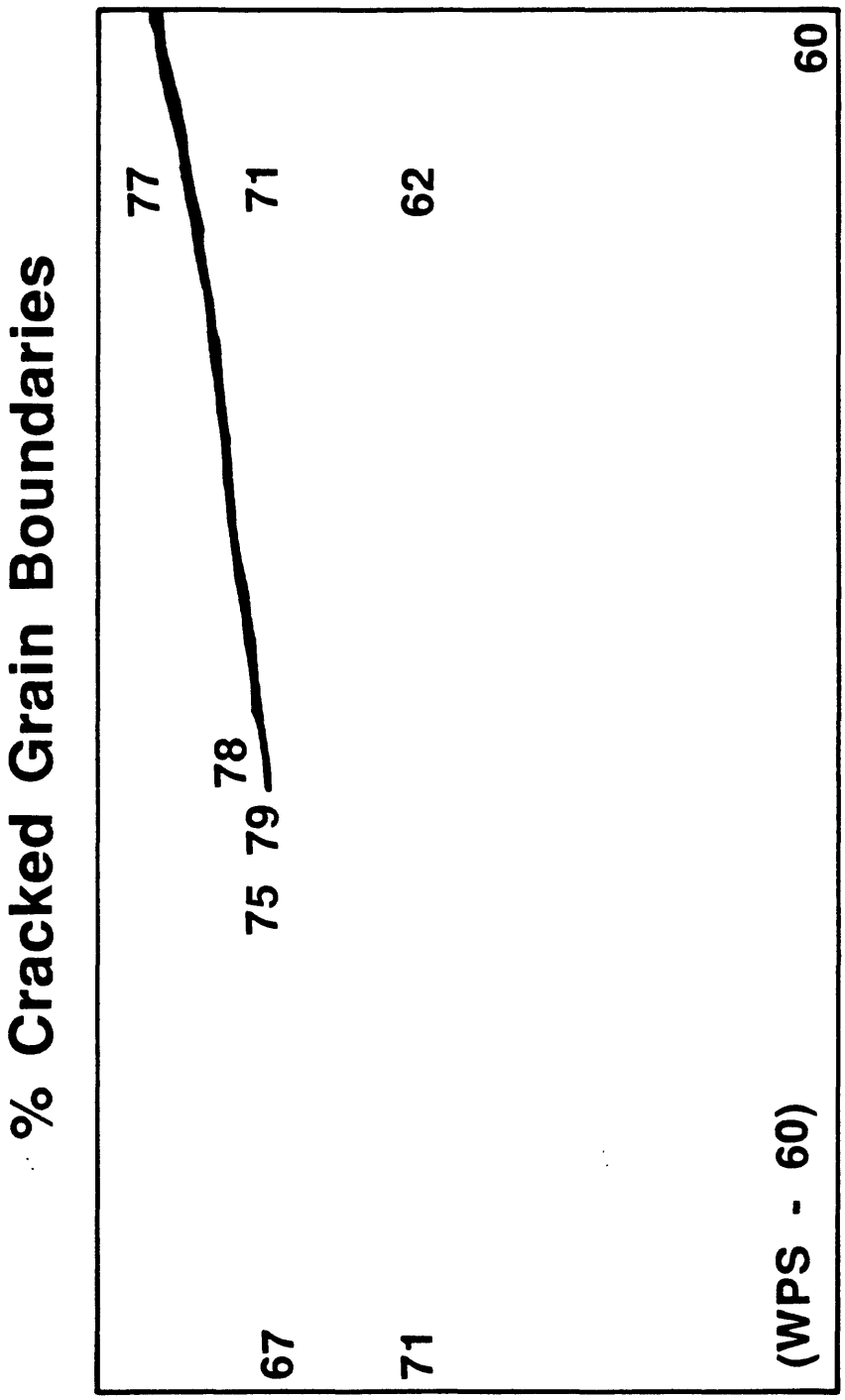

Figure 13. Sketch of part of the faulted cylinder, showing how the proportions of grain boundaries that are cracked vary with the position of a given image relative to the shear. Image locations are as shown in Figure 1; the value for the undeformed sample, WPS, is included in the lower left corner. The numbers above the shear fracture are for the 2 images (A-1 and B-1) that cross the fracture. Overall, the percentage of cracked grain boundaries increases with decreasing distance from the shear.

sections from the two cylinders may differ by perhaps only a few degrees. Rose diagrams of the stressed and unstressed samples can therefore be safely compared.

Figure 14 is a rose diagram of the summed grain-boundary lengths of Table 3. It shows the 50-60° trend of the flow structure, along with 2 other maxima at 0-20° and 90-100°. The majority of the grain-boundary length is correspondingly in the range 0-100°. The 90° orientation is the horizontal direction at the quarry and 0/180° is the vertical direction (Moore and Lockner, in preparation). The 2 maxima with these approximate orientations may represent equant crystals that settled flat in the pluton. Some good examples of the 0° and 90° trends in the grain-boundary orientations are found in A-3 (Figure 6) and A-4 (Figure 7).

The distributions of cracked and uncracked grain boundaries in each image are presented in Figures 15 to 24. There is considerable sample-to-sample variation, making direct comparisons difficult. However, comparison of WPS (Figure 15) with the stressed sample as a whole (Figure 25) suggests that much of the increase in grain-boundary cracking during the experiment was concentrated within about ±30° of the cylinder axis. As indicated above, attempts to identify preferred orientations of stress-induced cracking are best made by considering percentages of the total grain-boundary length in a given direction. The grouped data for samples far from the fracture ('far field', consisting of A-3, A-4, and C-1) and close to it ('near field', consisting of A-1, A-2, A-5, B-1, and B-2) are compared to WPS in Figure 26. In WPS, grain boundaries oriented at a large angle to the cylinder axis are preferentially cracked, whereas the percentage rose diagram for the far-field samples has almost no directionality. The percentage rose diagram for the near-field images has a slight preferred orientation centered at about 155°.

The cracking associated with the initial, disseminated stage of acoustic emission (Figure 2a) can be isolated in a rough manner by subtracting the rose diagram for the undeformed rock WPS from the one for the far-field samples. In the same way, cracking associated with the shear fracture itself can be separated by subtracting the far-field rose diagram from the near-field diagram. The degree of cracking in the two images containing the shear fracture (A-1 and B-1) is no higher than in the process-zone images; the cracking at these sites may therefore be principally inherited from the earlier passage of the process zone (Figure 2b). The results of these operations are shown in Figure 27. The stress-induced grain-boundary cracking in the far-field samples has a predominantly axial trend. For the near-field samples, there is an additional axial component of increase, but the greatest change is in the range 130-150°. These results are generally consistent with the proposed trends in crack orientation illustrated in Figure 2. Among the uncracked grain boundaries in the large cylinder prior to the start of the experiment, those making the smallest angles to the locally predominant stress fields tended to crack preferentially.

Grain-boundary cracking is a function of mineralogy (Table 4) as well as the imposed stresses. Grain boundaries involving quartz are the ones most likely to be cracked in both the stressed and unstressed samples. Boundaries between two feldspars have a lower percentage of cracking in both cylinders; among these, boundaries between plagioclase and K-feldspars are less commonly cracked than those between like feldspars. Just over 10% of plagioclase-K-feldspar boundaries in WPS are cracked, and the percentage increases only to 40% in the stressed sample. The growth relationships between plagioclase and K-feldspar can explain the relatively small degree of grain-boundary cracking between them. K-feldspar commonly forms a mantle around plagioclase. This mantling relationship can be seen in all the images, but especially good examples are in WPS (Figure 3), A-1 (Figure 4), and A-4 (Figure 7). By comparison with similar textures in Barre granite (Chayes, 1950), the overgrowths may be a late-stage igneous crystallization process, with the K-feldspar finding a preferred nucleation site on the plagioclase. The plagioclase core and the K-feldspar mantle are in crystallographic

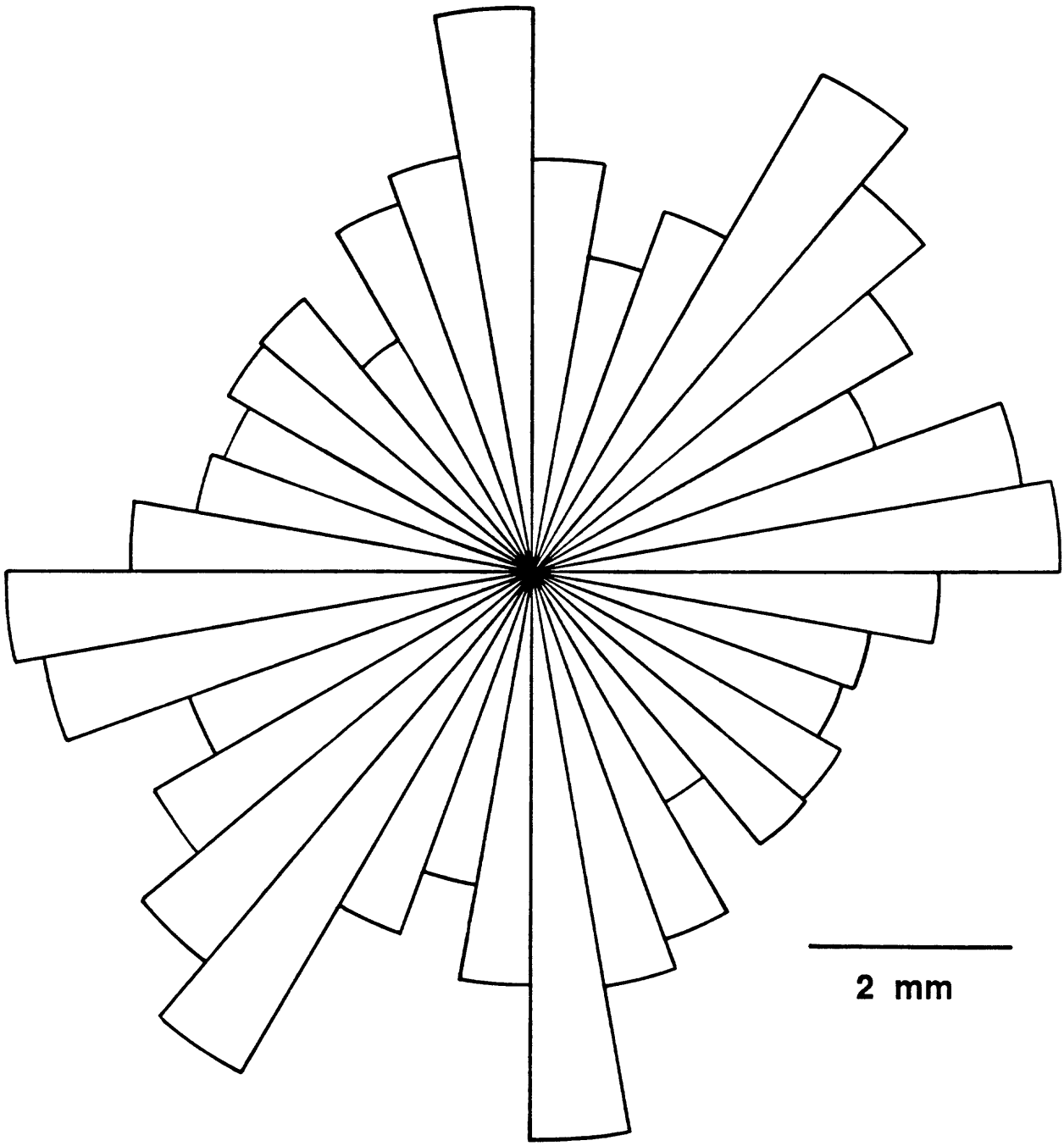

Summed Grain Boundaries

Figure 14. Rose diagram of the summed grain-boundary lengths of the 10 images. The mineral outlines show a moderately preferred alignment, with the majority oriented in the range 0-100° and 3 maxima in this range at 0-20°, 50-60°, and 90-100°. The 50-60° maximum corresponds to the igneous flow structure described in the text. In this and all other rose diagrams, the scale bar applies to the angular range 0-180°.

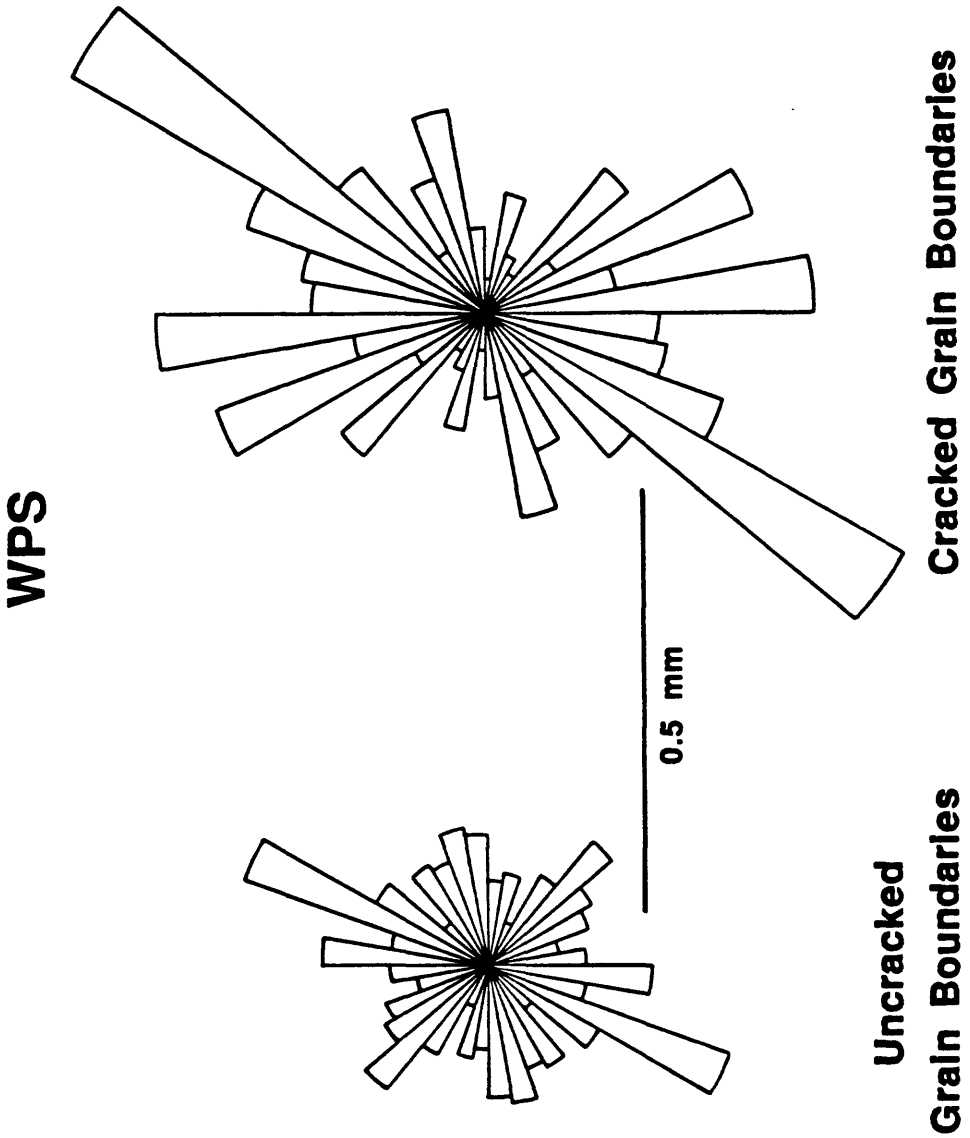

Figure 15. Rose diagrams of cracked and uncracked grain boundaries in the undeformed sample, WPS. The well-developed flow structure in this image produces a prominent spike in both diagrams.

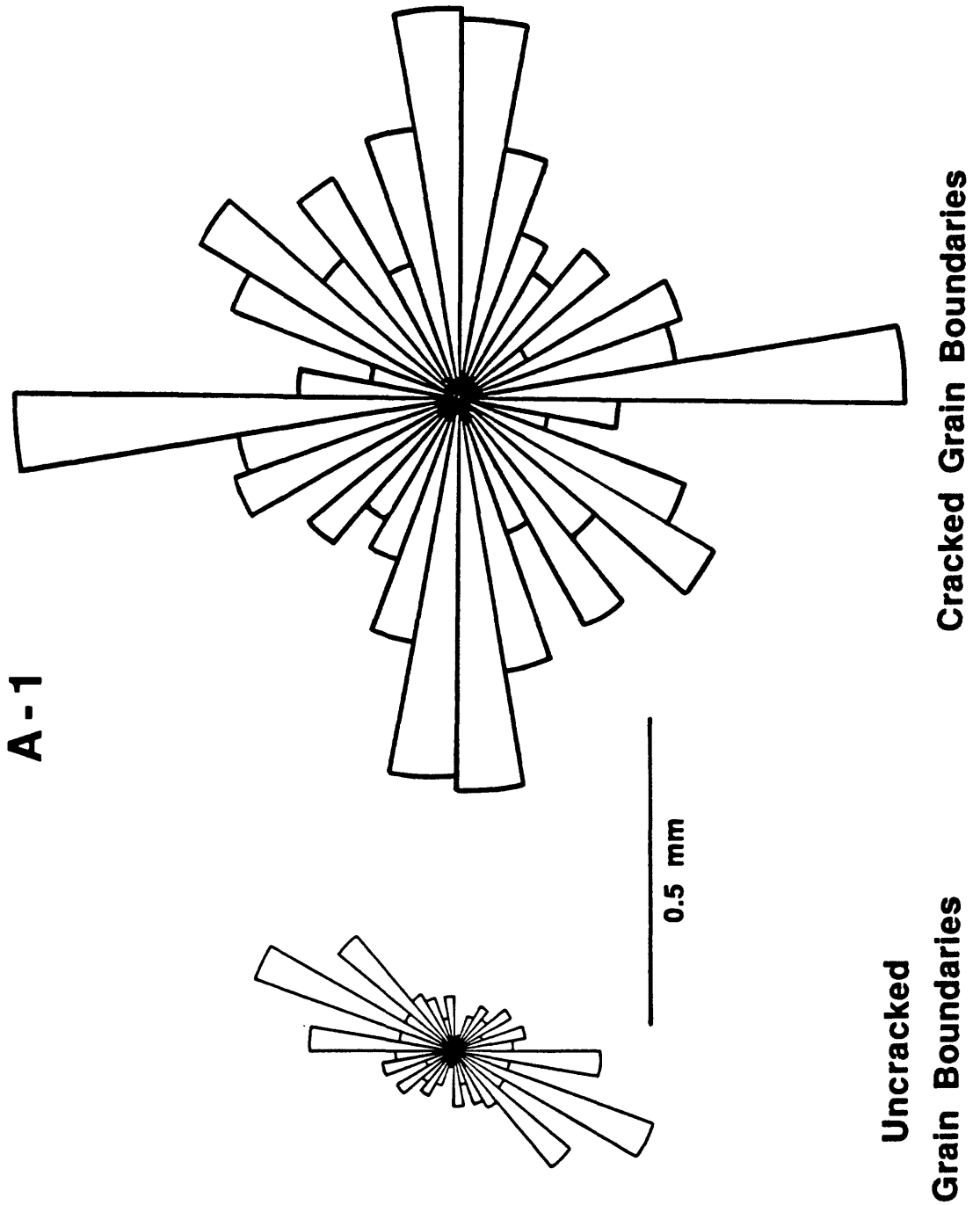

Figure 16. Rose diagrams of cracked and uncracked grain boundaries in image A-1, at the fracture tip. The few uncracked grain boundaries in this sample are concentrated in the range 40-90°.

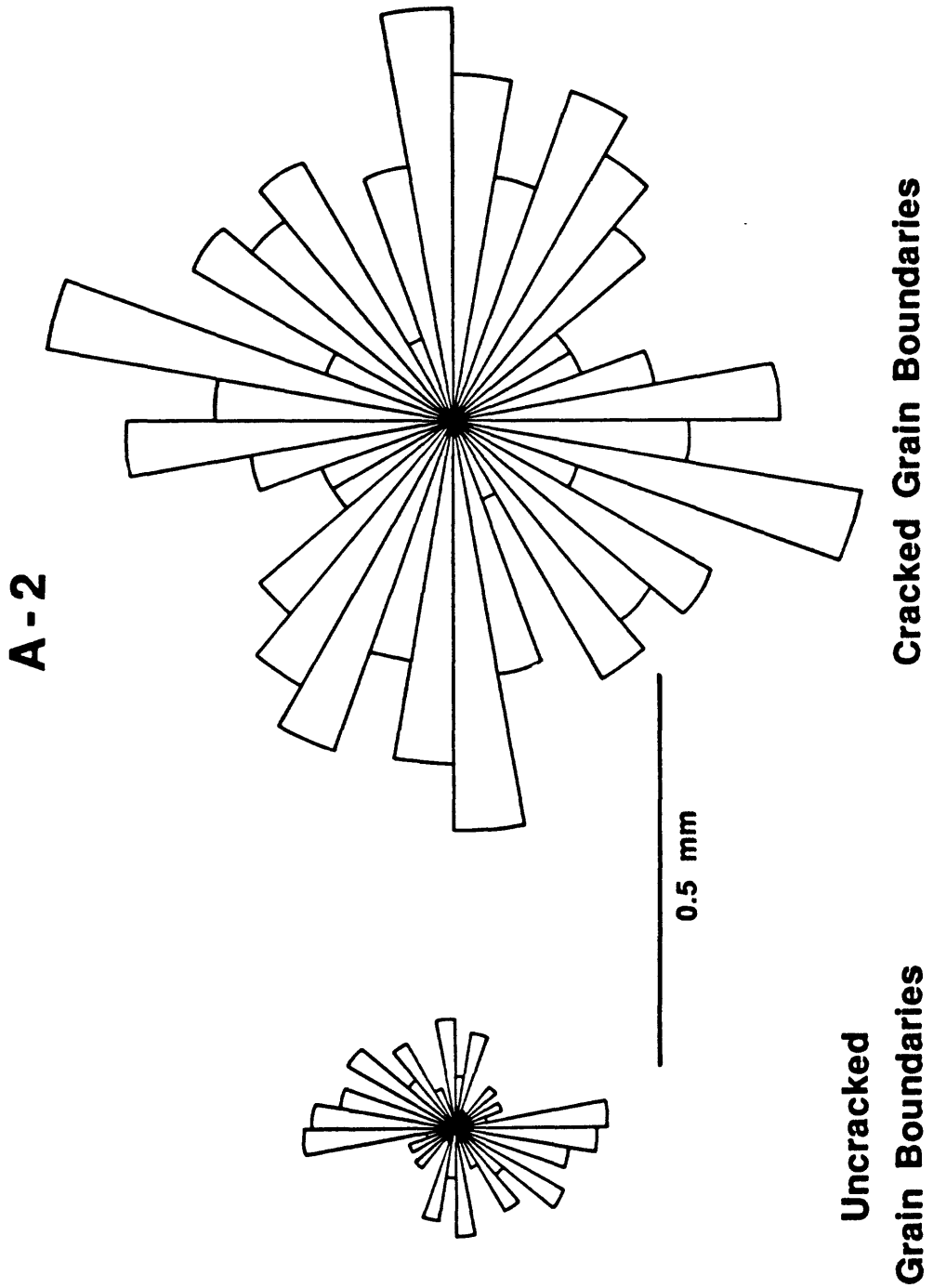

Figure 17. Rose diagrams of cracked and uncracked grain boundaries in image A-2 of the process zone. Very few uncracked grain boundaries remain in the range 100-160°.

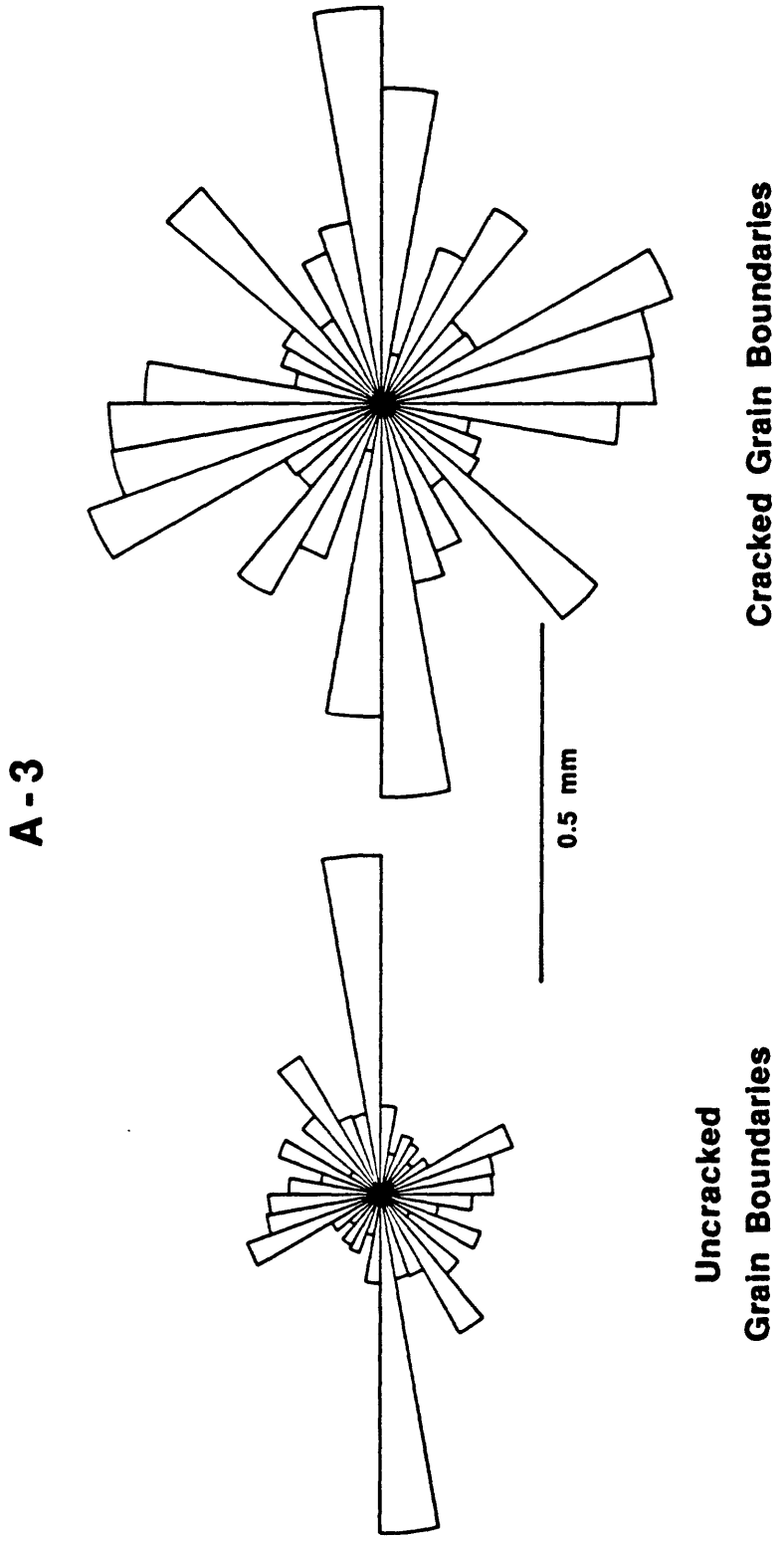

Figure 18. Rose diagrams of cracked and uncracked grain boundaries in far-field image A-3. A prominent spike at 0-10° appears in both plots.

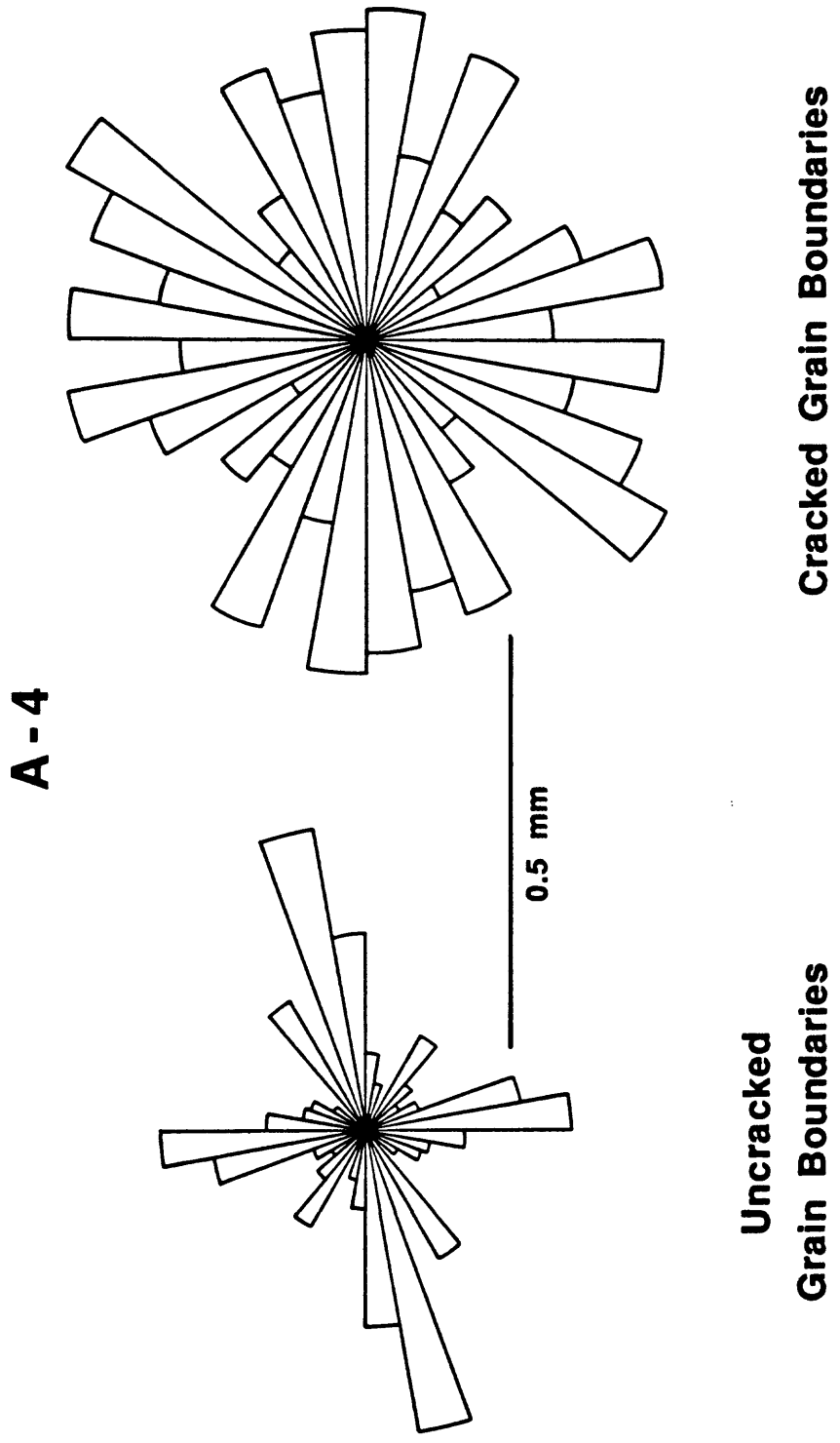

Figure 19. Rose diagrams of cracked and uncracked grain boundaries in far-field image A-4. The cracked grain boundaries have essentially no preferred orientation.

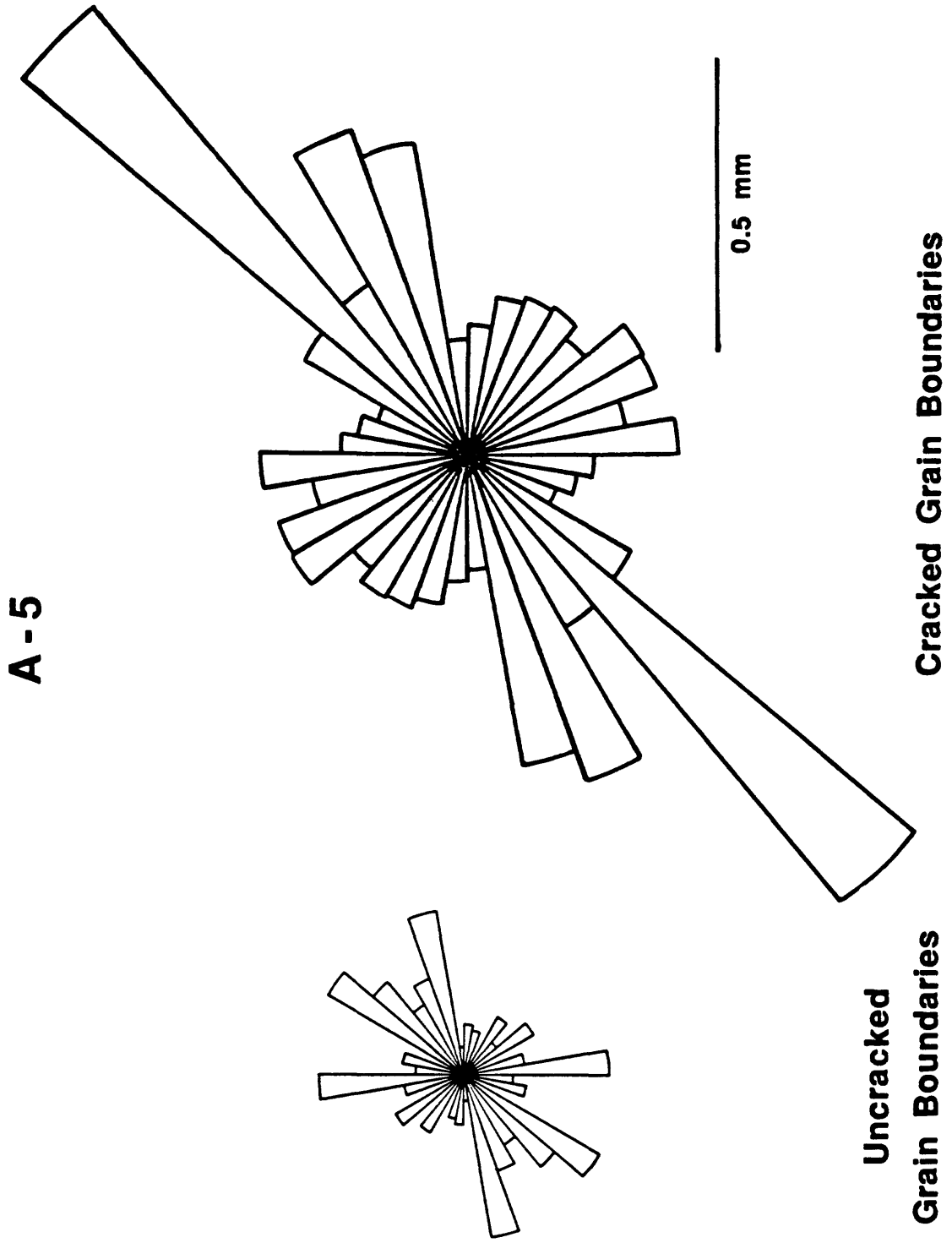

Figure 20. Rose diagrams of cracked and uncracked grain boundaries in image A-5 of the process zone. The aligned tabular crystals that are prominent in the image (Figure 8) produce a large spike in the rose diagram of cracked grain boundaries. The great majority of the uncracked grain boundaries are oriented between 10° and 100°.

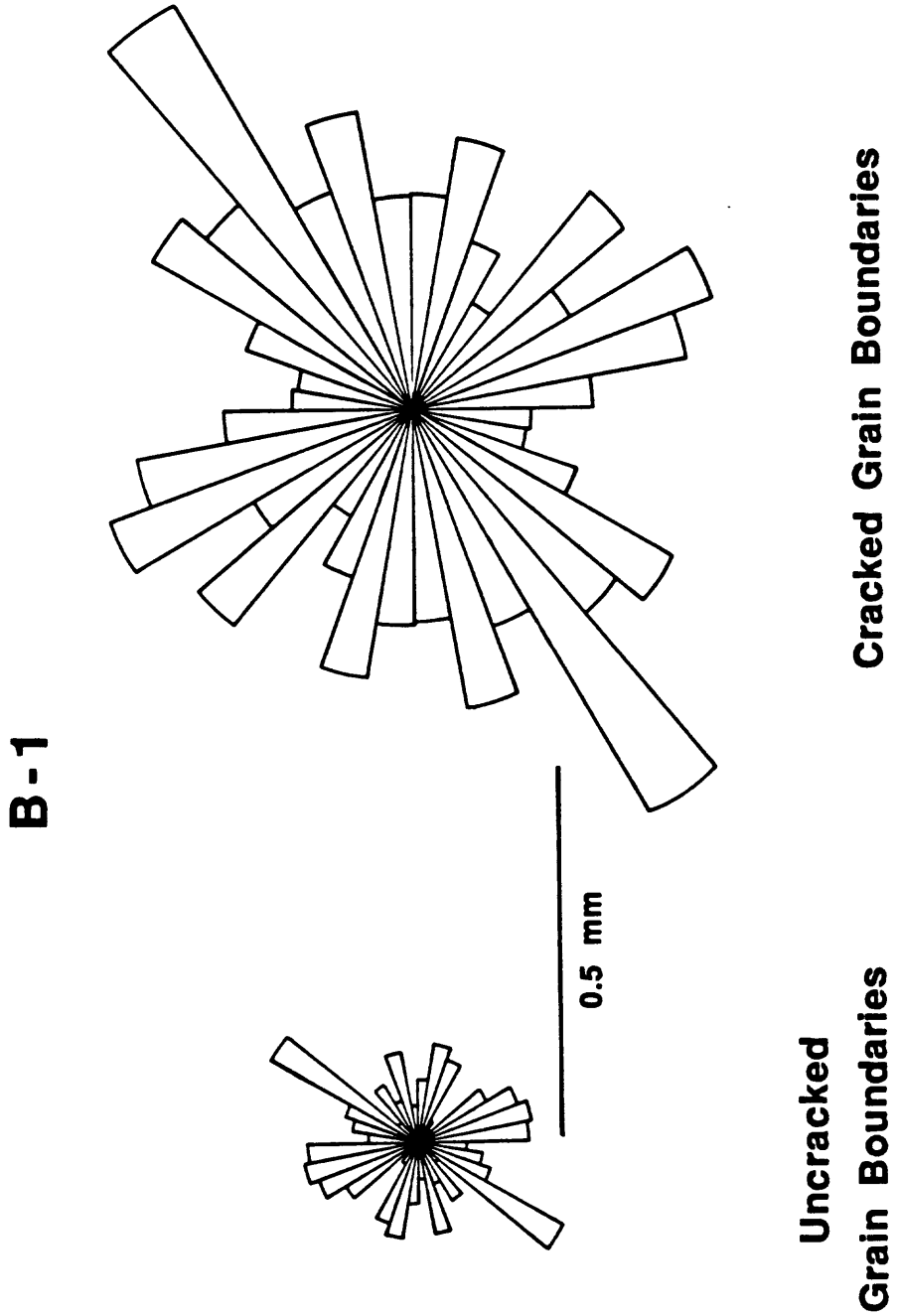

Figure 21. Rose diagrams of cracked and uncracked grain boundaries in B-1, which straddles the shear fracture. The flow structure produces a spike in both plots.

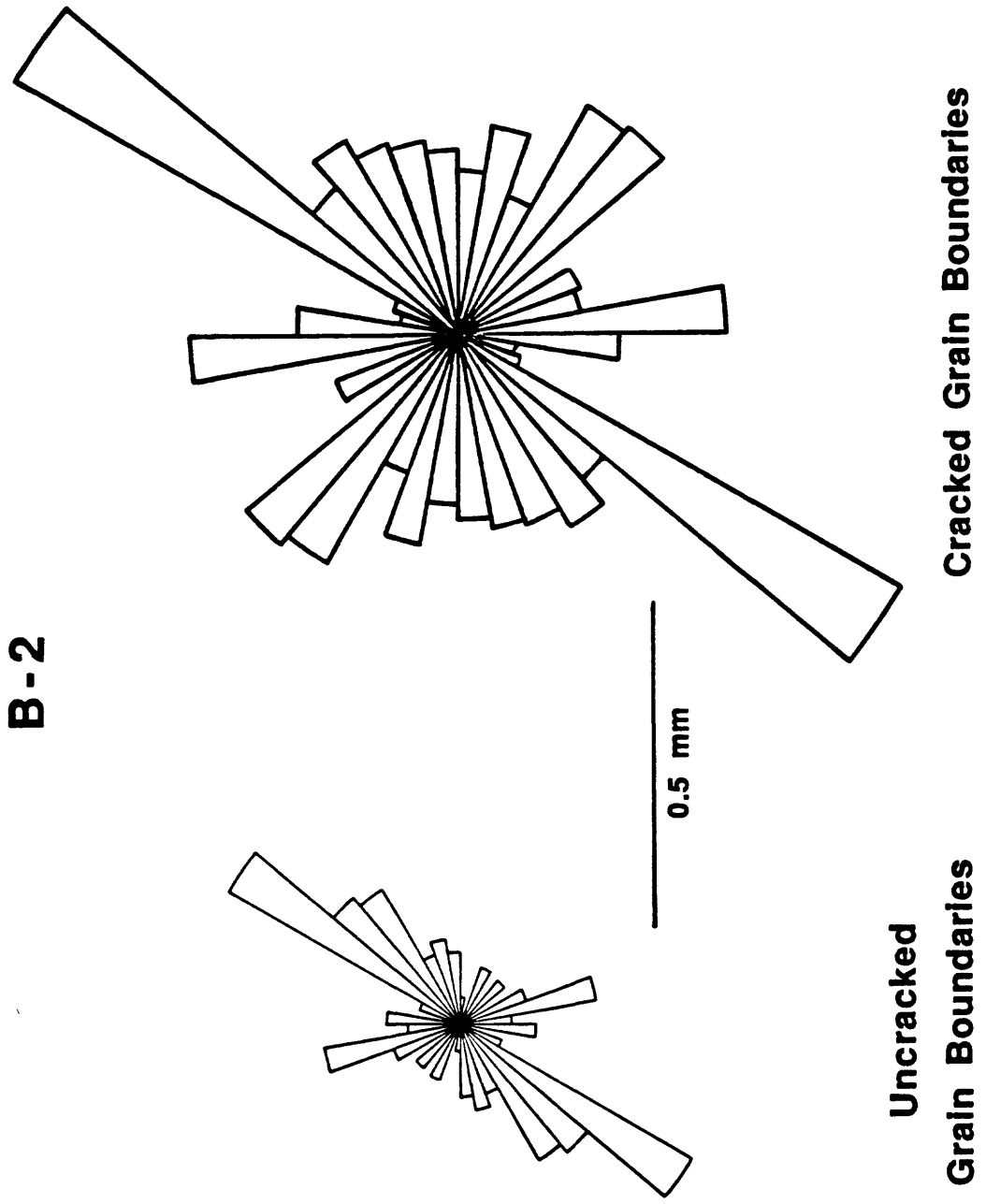

Figure 22. Rose diagrams of cracked and uncracked grain boundaries in image B-2, to one side of the shear. The igneous flow structure is prominent in both diagrams.

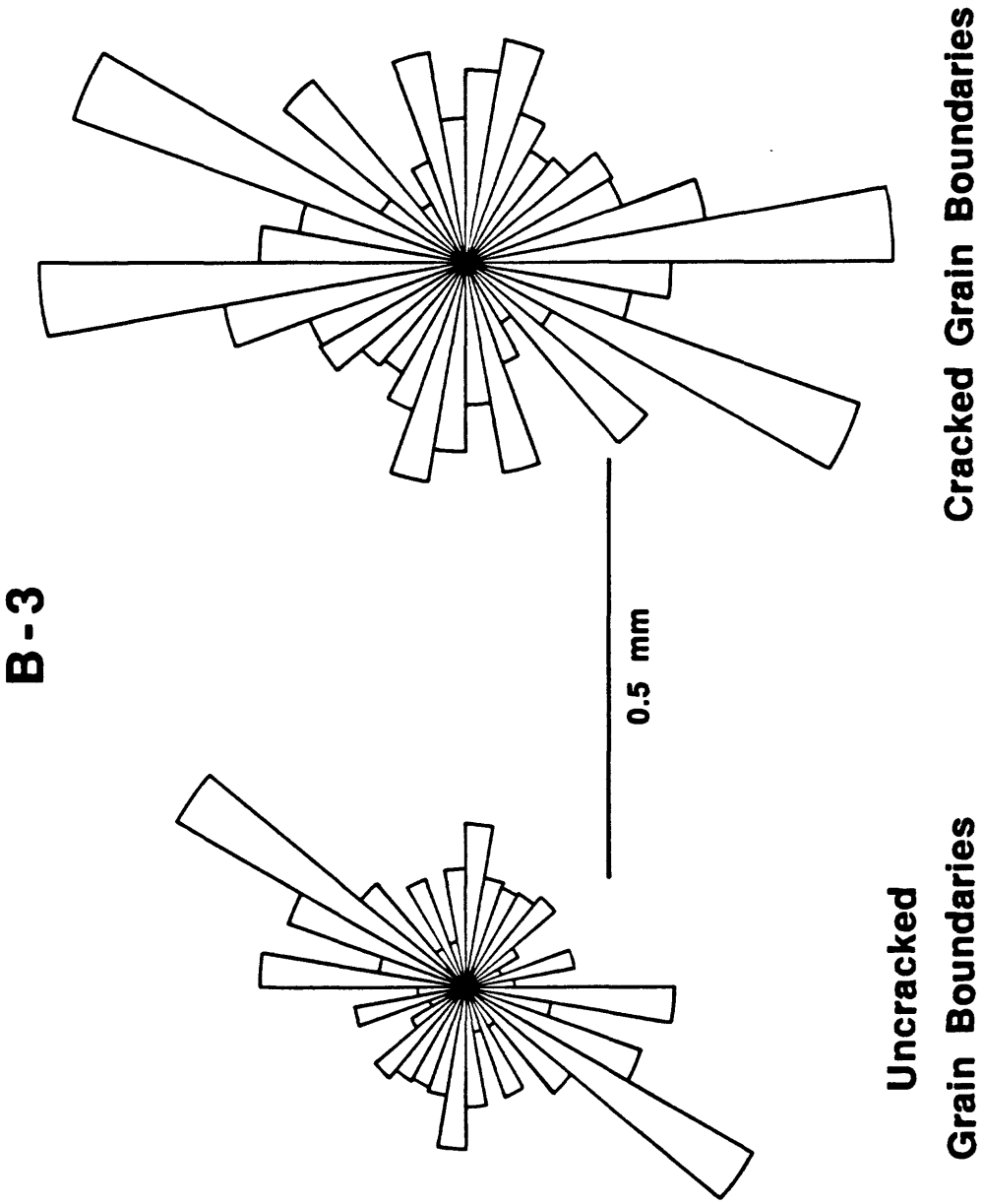

Figure 23. Rose diagrams of cracked and uncracked grain boundaries in image B-3, located about 8 mm to the side of the shear fracture. The rose diagram of uncracked grain boundaries has a preferred orientation of 50-60°.

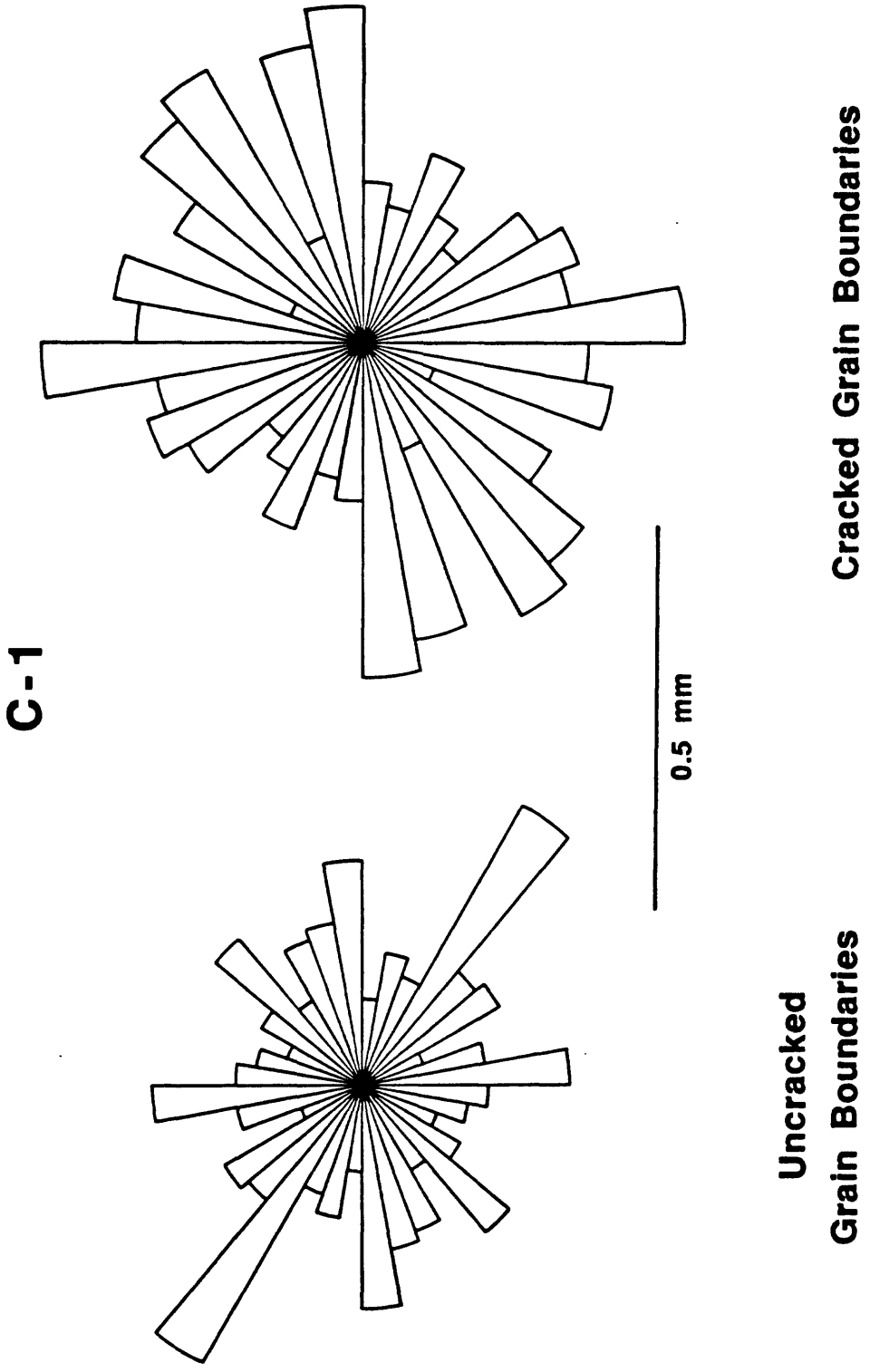

Figure 24. Rose diagrams of cracked and uncracked grain boundaries in far-field image C-1. Compared to WPS (Figure 15), the plot of cracked grain boundaries has filled out roughly parallel to the cylinder axis.

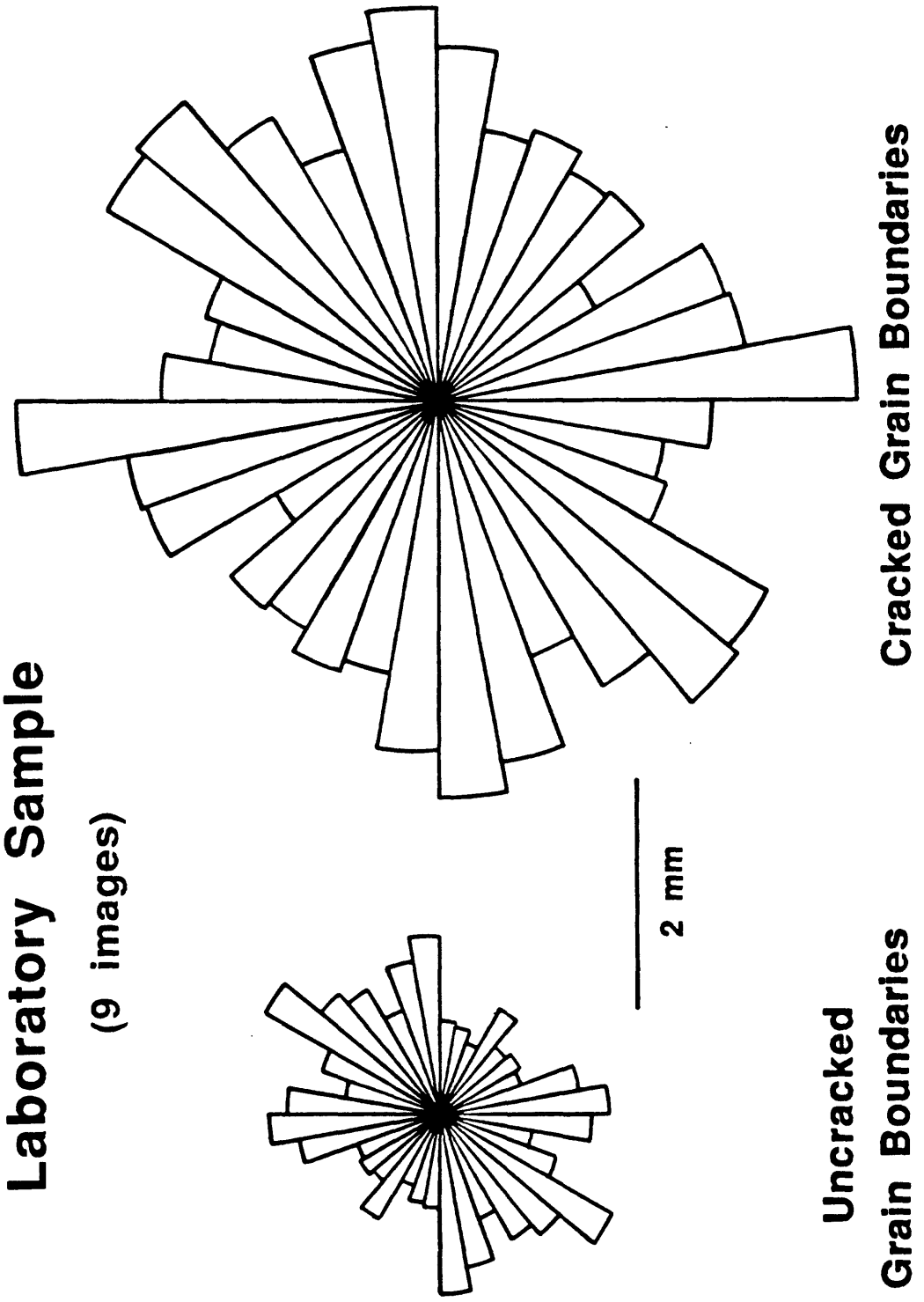

Figure 25. Rose diagrams of cracked and uncracked grain boundaries for the combined images of the stressed sample. Compared to the undeformed sample (Figure 15), the large cylinder shows a relative increase in the amount of cracking of grain boundaries with a roughly axial orientation. The minimum length of uncracked grain boundaries occurs in the range 110-180°.

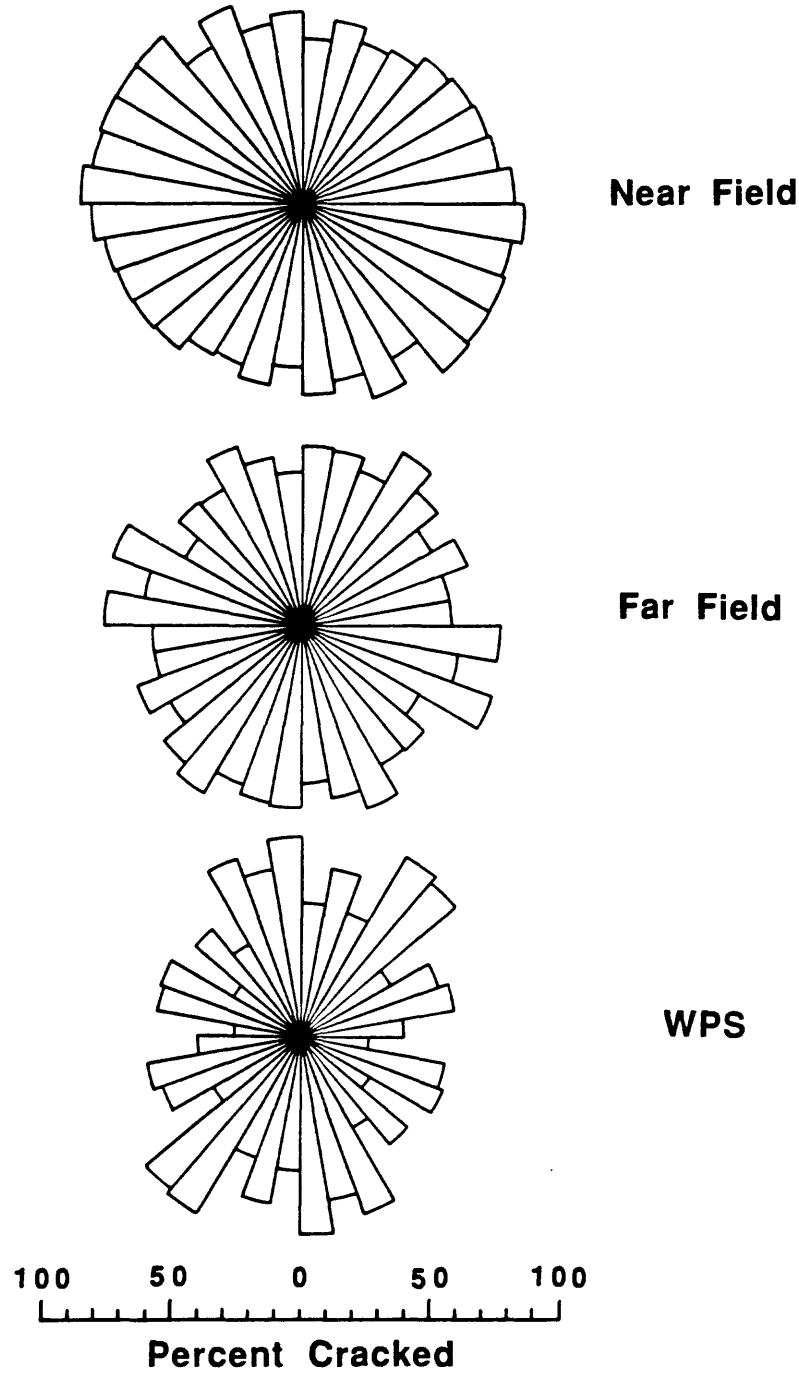

Figure 26. Rose diagrams of cracked grain boundaries as the percentage of the total grain-boundary length in a given direction. The far-field images are A-3, A-4, and C-1, which are located well away from the shear fracture. The near-field images are A-1, A-2, A-5, B-1, and B-2; they are all situated within a few mm of the shear fracture. Compared to WPS, the far-field rose diagram has a more circular shape, whereas the near-field rose diagram has a more ellipsoidal outline with the major axis at about 155°.

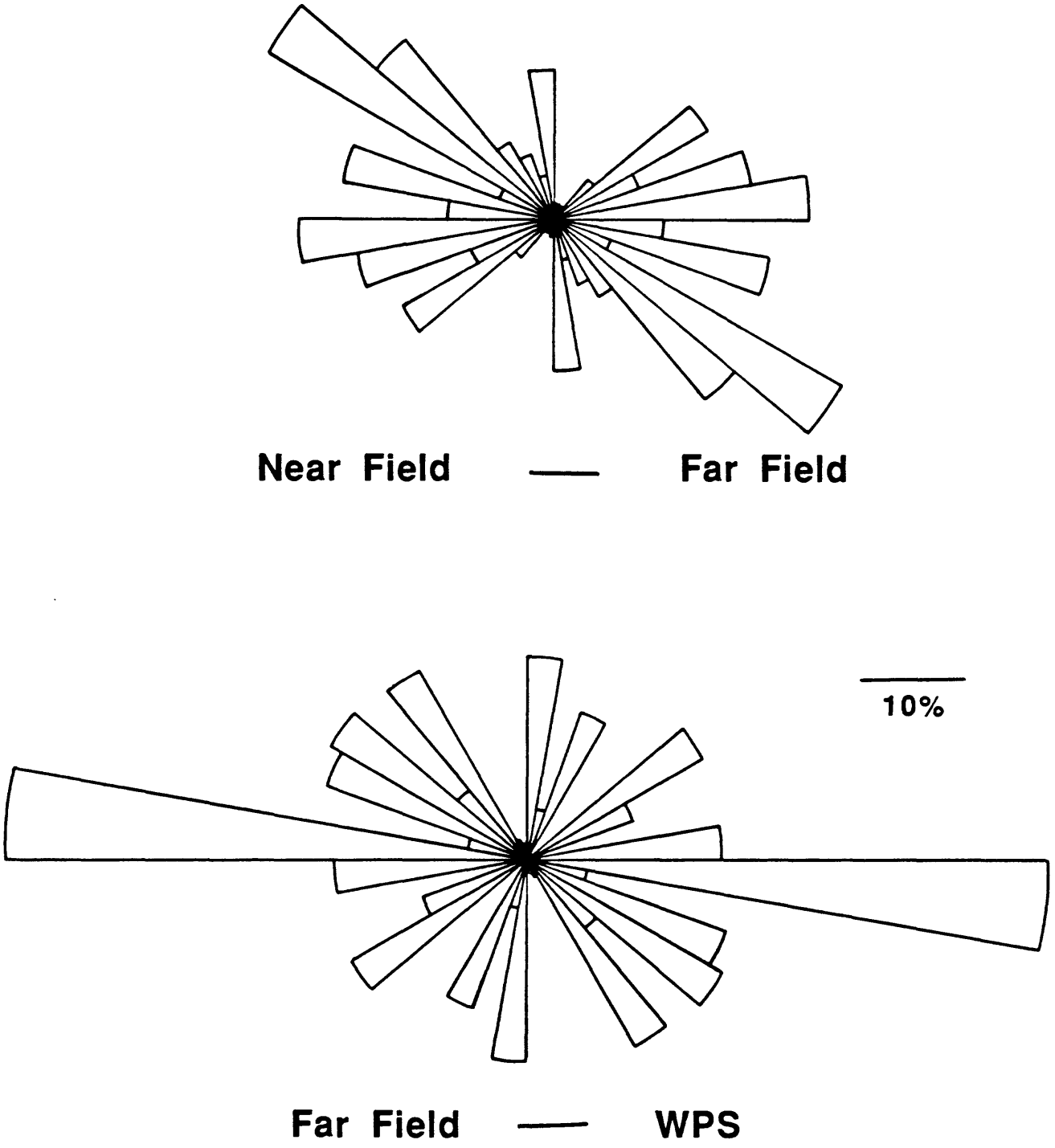

Figure 27. Rose diagrams showing the increases in the amount of cracking moving from the undeformed rock to the far-field areas, where by far the largest increase was at 170-180°, and from the far-field to near-field areas, where the greatest increase occurred at 140-150°.

Table 4.
Percent Cracked
Grain Boundaries

Minerals at Boundary	Starting Material (WPS)	Laboratory Sample (9 images)
Qtz - Qtz	90%	97%
Qtz - Plag	72%	90%
Qtz - Kspr	76%	90%
Plag - Plag	29%	68%
Kspr - Kspr	60%	66%
Plag - Kspr	12%	41%

continuity, and at least some local replacement of plagioclase by K-feldspar appears to have occurred. Such crystallographically controlled boundaries should be stronger than those produced by the random impingement of separately growing crystals and, indeed, the mantled plagioclase-K-feldspar boundaries are the ones least likely to be cracked. In effect, cracking such boundaries would be almost the same as forming an intragranular crack in feldspar.

MICROCRACK MAPS

Maps of all the microcracks identified in each image (Figures 28-37) illustrate the progressive increase in microcrack density going from the undeformed sample WPS to the highly deformed areas along the shear fracture. Nevertheless, only at the sites immediately adjacent to the shear fracture can a continuous path be traced along the microcracks both horizontally and vertically across the entire image. Except for the shear fracture itself, the degree of connectivity at all sites is largely a function of the continuity of the grain-boundary cracking (compare corresponding mineral and crack maps). The nearly 80% grain-boundary cracking near the shear fracture is what provides the fairly continuous, open network of cracks in that part of the sample. In contrast, many of the intragranular cracks either appear isolated, at least within the plane of the thin section, or they extend only a short distance into a crystal from a grain-boundary.

Comparison of the microcrack maps in Figures 28-37 with the mineral maps in Figures 3-12 also suggests that the longest individual microcracks follow grain boundaries, cleavage traces, or simple twin planes. The longest crack in WPS is a 350 μm grain-boundary crack, whereas the longest cracks in the large cylinder reach nearly 600 μm. Only rarely does a single crack cross a grain boundary and extend into an adjoining crystal. The maximum crack length is less than the average crystal diameter in Westerly. Many of the new cracks in the far-field areas and the process zone are quite short, whereas the crack lengths are greater alongside the shear fracture and within the shear at the tip.

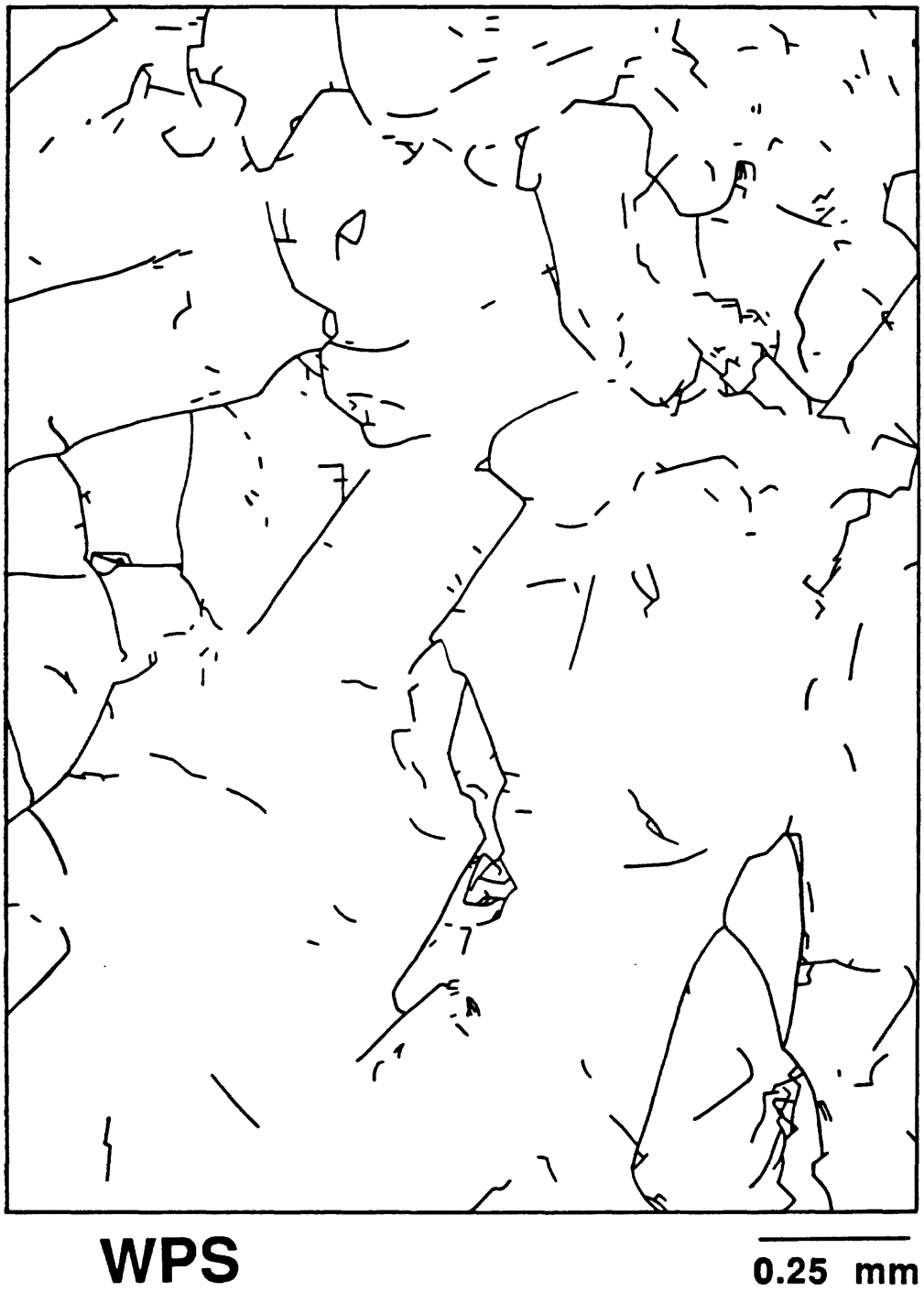

Figure 28. Microcrack map of the undeformed sample WPS. The longest cracks in this sample are grain-boundary cracks, and linked grain-boundary cracks form the most continuous crack network in the sample.

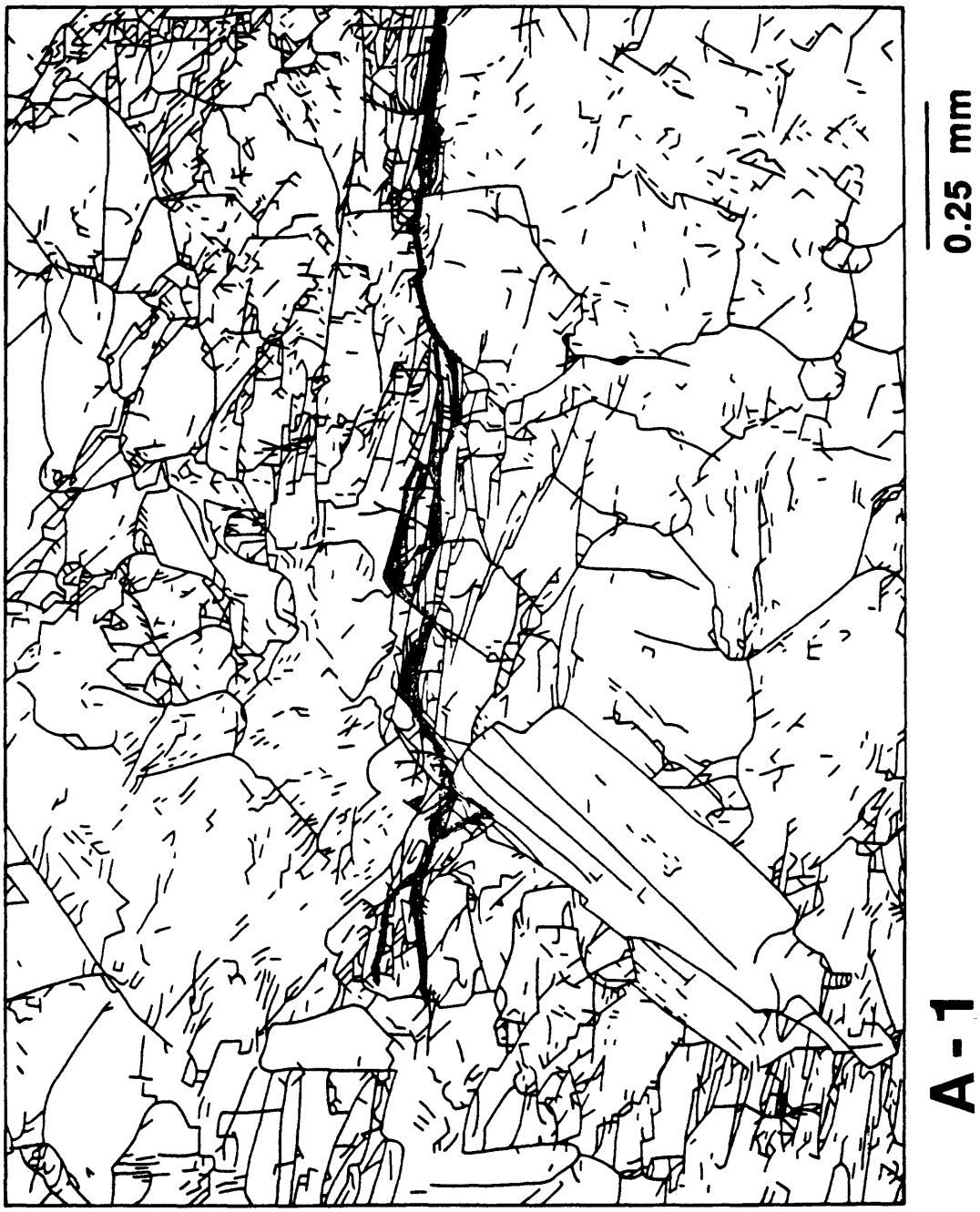

Figure 29. Microcrack map of image A-1 at the fracture tip. The shear fracture is delimited by the heavy line. The crack density is clearly greater above the shear fracture, but the cracks are also irregularly distributed on both sides.

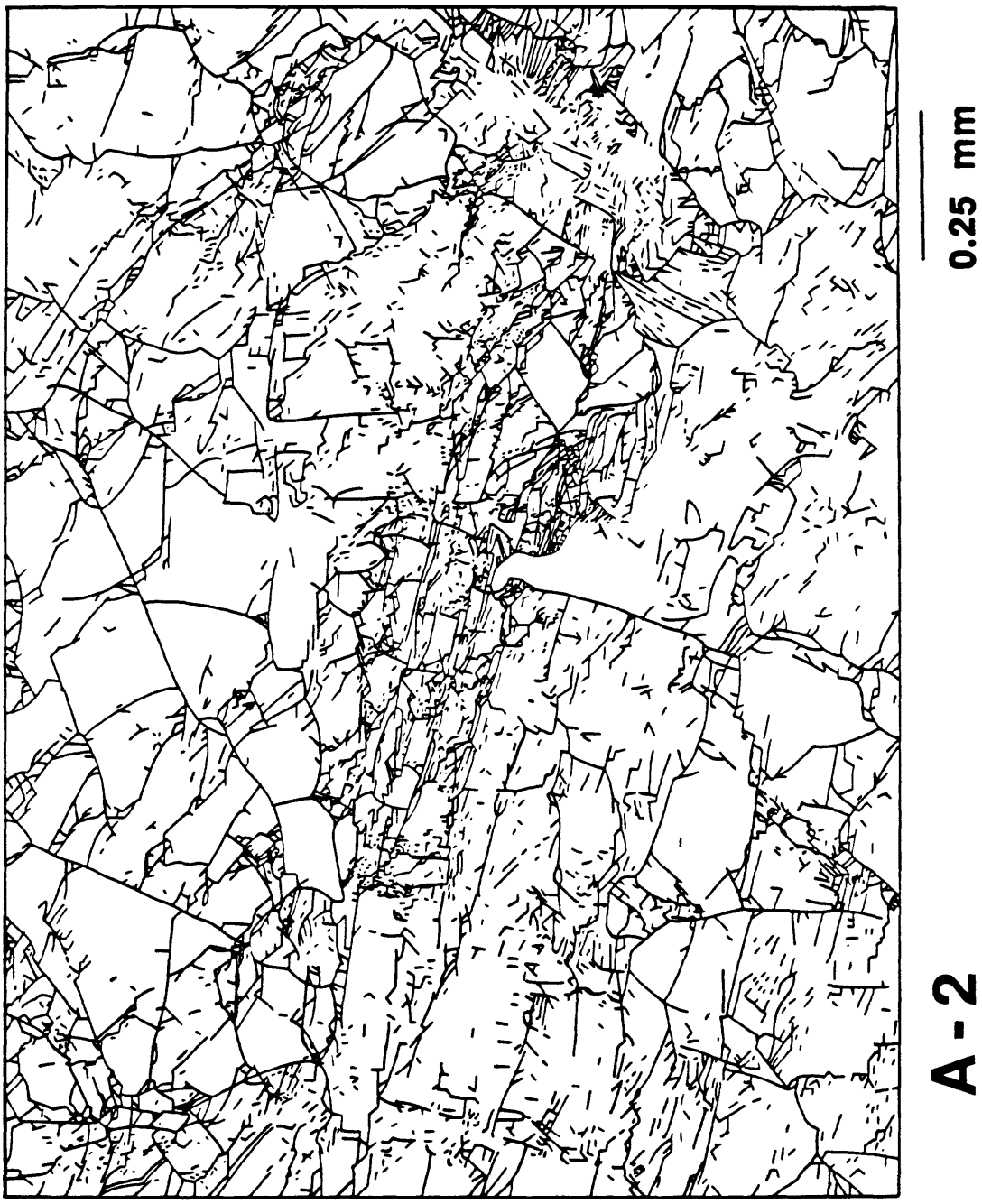

Figure 30. Microcrack map of image A-2, of the process zone. Crack densities are highest across the center of the image, and many of them are close to the 3μm measuring limit.

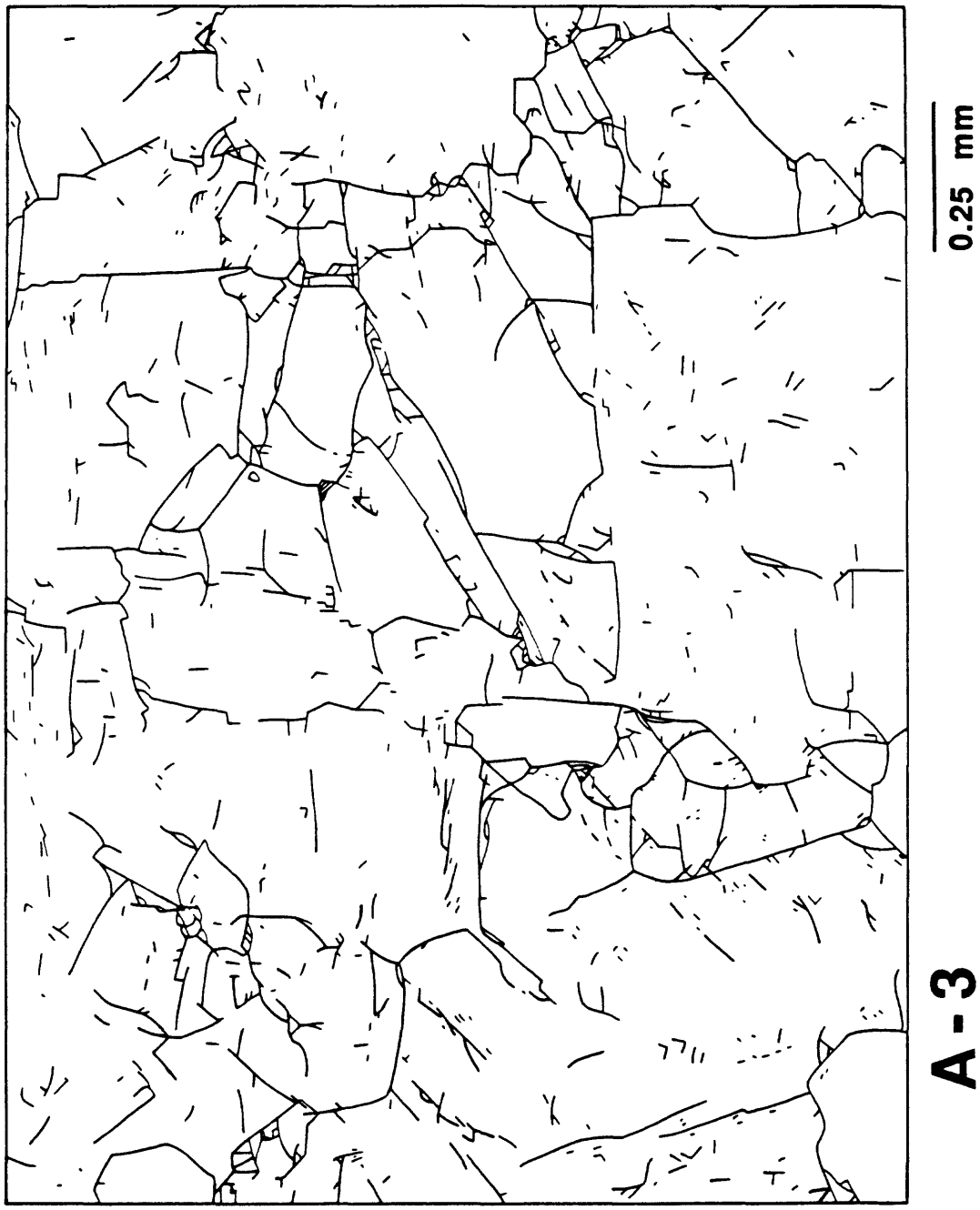

Figure 31. Microcrack map of far-field image A-3. The intragranular cracks tend to be relatively short and isolated, compared to the grain-boundary cracks.

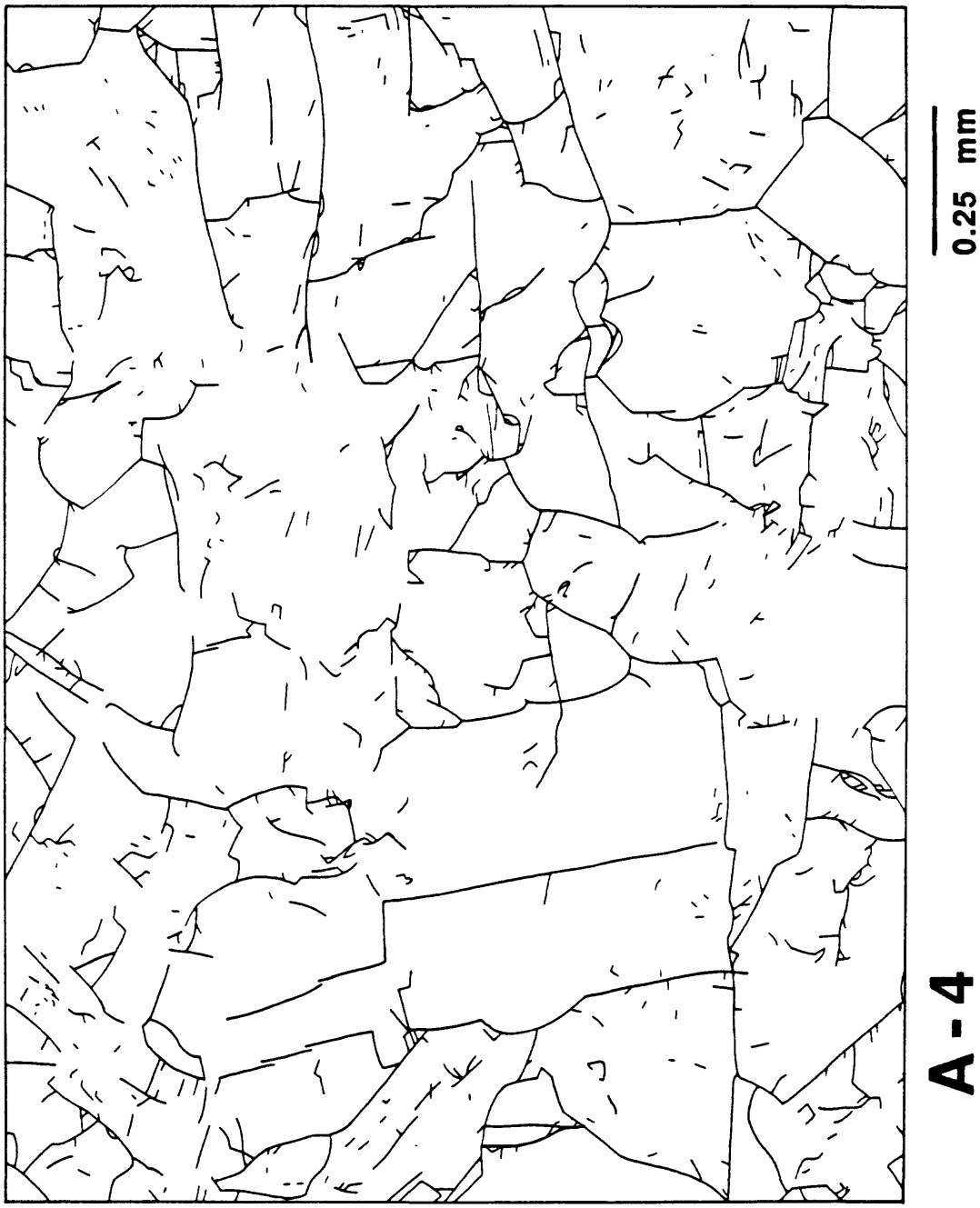

Figure 32. Microcrack map of far-field image A-4. The intragranular cracks appear to be better connected to each other and to grain boundaries than they are in A-3 (Figure 31).

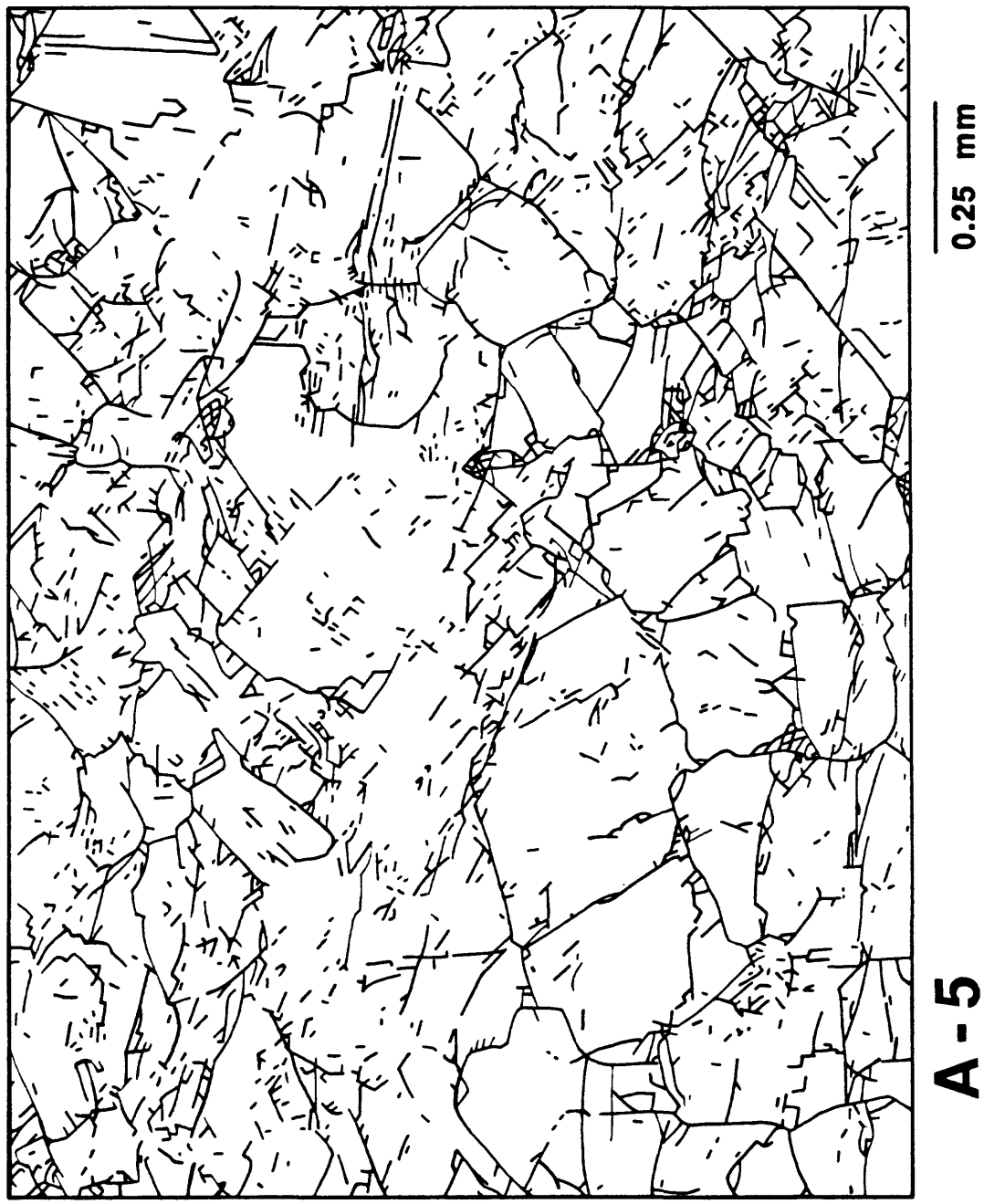

Figure 33. Microcrack map of process-zone image A-5. Crack densities are substantially higher than in the far-field images. Many of the cracks are very short and occur in parallel groupings suggestive of cleavage cracking.

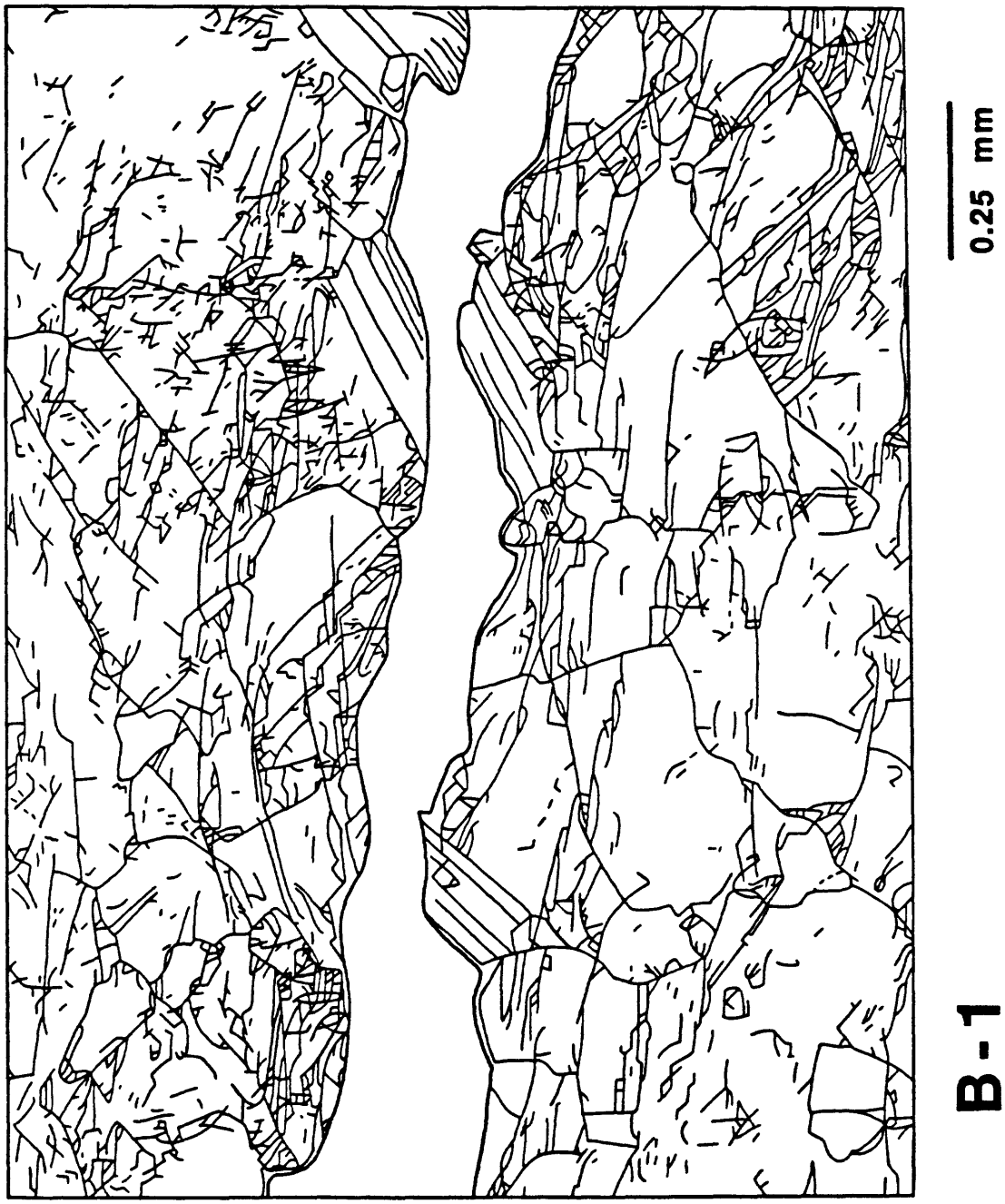

Figure 34. Microcrack map of image B-1 across the shear fracture. Intragranular cracks adjacent to the shear are relatively long and connected to each other.

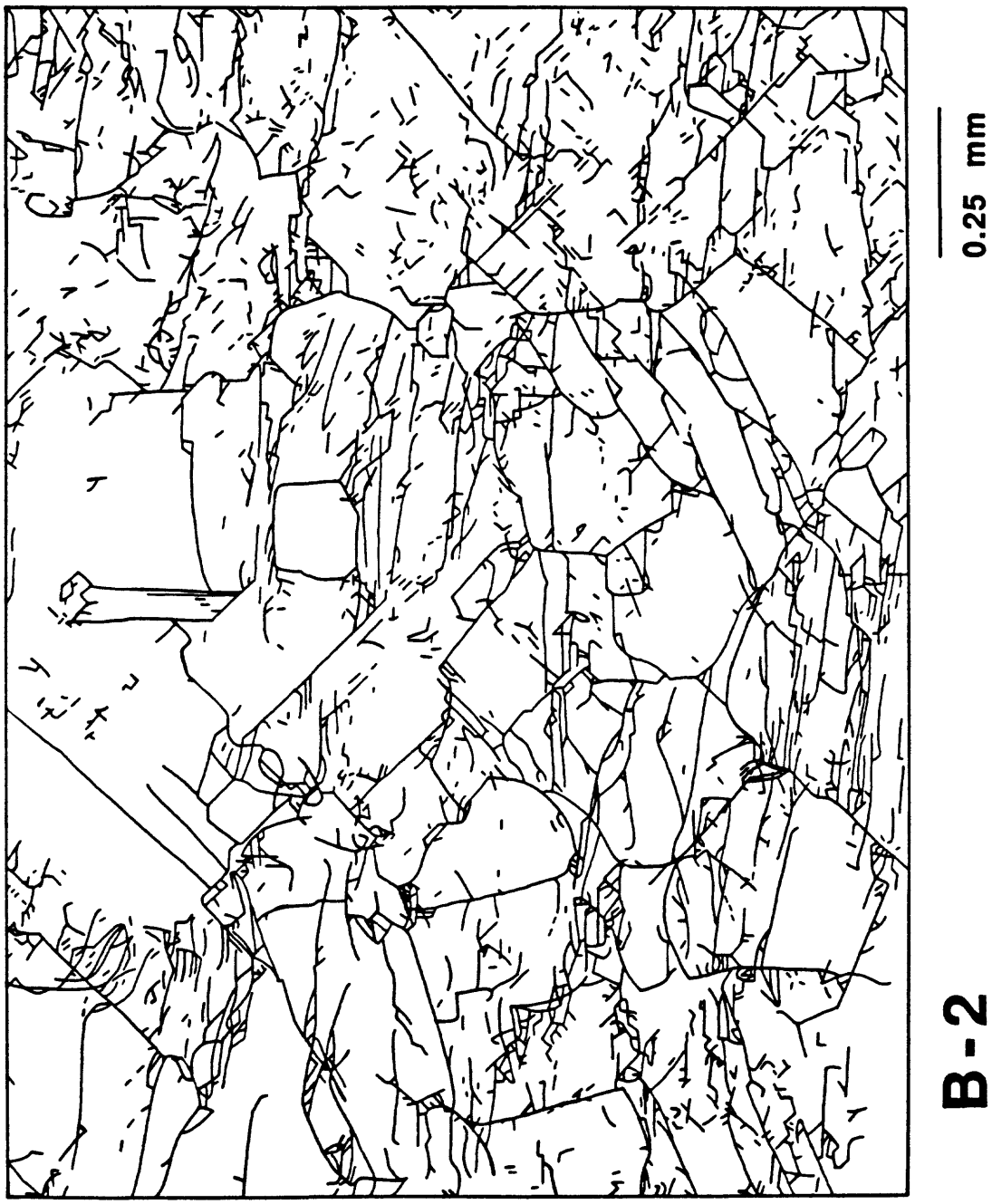

Figure 35. Microcrack map of image B-2, located 3 mm to the side of the shear fracture. Crack densities vary markedly from crystal to crystal.

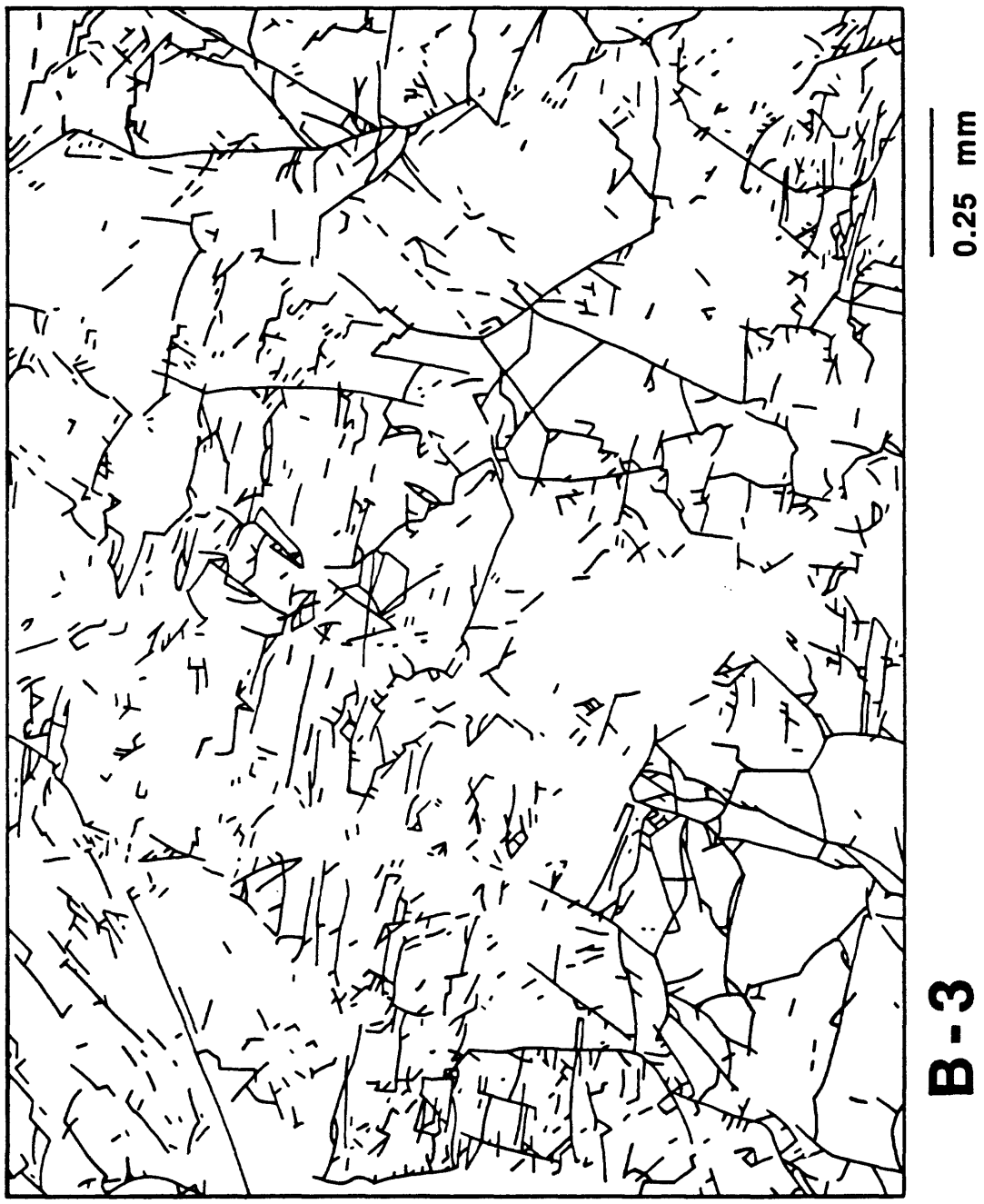

Figure 36. Microcrack map of image B-3, located about 8 mm to the side of the shear fracture. Parts of the image are essentially crack-free, whereas others are heavily cracked.

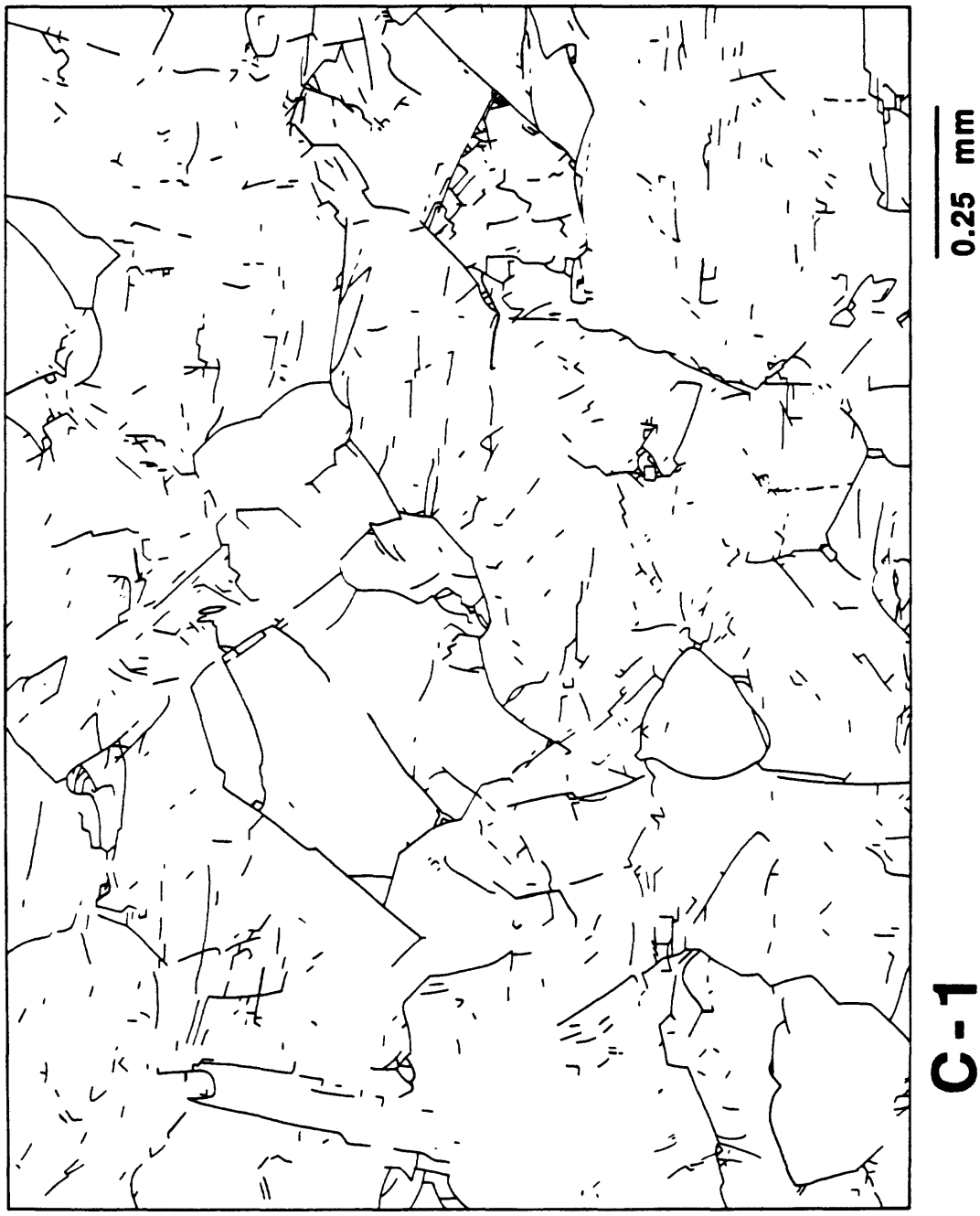

Figure 37. Microcrack map of far-field image C-1, characterized by numerous short, intragranular cracks.

TOTAL CRACK DENSITIES AND ORIENTATIONS

Tables 5 and 6 present the intragranular and total crack lengths relative to orientation. Images A-1, A-2, and B-1, which are closest to the shear fracture, have the highest crack densities. The crack populations in these three images were separated into subzones, as illustrated in Figures 4b, 5b, and 9, to look for trends across them (Tables 7 and 8). The variations in total crack density among the images, from Table 6, are illustrated in Figure 38. The far-field areas contain about twice the microcrack density of the starting material, and the densities increase progressively as the shear fracture is approached. The highest crack densities in the process zone are found in the rock directly in front of the fracture tip, and the fracture tip itself has over an order of magnitude increase in cracking over the undeformed rock (Table 8). The zone I portions of images A-1, B-1, and A-2, which are situated on the dilational side of the shear, have 11-35% higher crack densities than their zone III counterparts on the compressional side.

The data in Tables 5-8 are plotted in Figures 39-48. Grain-boundary cracks comprise about half the total crack length in WPS, about one third of the far-field cracks, and a considerably smaller proportion of the near-field cracking. The great increases in crack density in the process zone and along the shear fracture, therefore, are principally attributable to new intragranular cracks. The microcrack orientations vary among the different images. WPS has a preferred orientation centered around 90°, with the flow structure forming a spike at 50-60°. This 90° fabric, which is in the horizontal plane at the quarry, probably represents stress-relief cracking accompanying unroofing of the pluton (Moore and Lockner, in preparation). In contrast, the far-field samples A-3, A-4, and C-1 have a modest alignment centered around the cylinder axis. The rose diagrams of the process zone have a stronger microcrack fabric trending about 150°. Microcracks surrounding the fracture at B-1 have a more subdued version of the orientations in the process zone, trending up to the left overall, but at an angle of 160-170°.

In order to isolate the two stages of stress-induced cracking (Figure 2), the total crack content of WPS was subtracted from an average of the 3 far-field samples, and the far-field average was in turn subtracted from image A-2 of the process zone (Figure 49). This procedure is the same as that used on the grain boundary cracks in Figure 27. A far-field rose diagram was subtracted from the subdivided images near the shear fracture, to produce Figures 50-52. These plots reveal the predominantly axial trend of the early, pre-failure cracks and the inclined orientations of the cracks in the process zone. Both sets of cracks correspond overall to tensile cracks formed in response to the locally prevailing stresses. The subdivided images of A-1 and A-2 show that the cracks on the dilational side of the shear (zones I) make a larger angle to the cylinder axis than those on the compressional side (zones III), consistent with the calculated stress fields around the fracture tip (Figure 2b; Pollard and Segall, 1987). The central subzones (zones II) of A-1 and A-2 contain an added component of lower-angle cracks that serve to link up the tension cracks, eventually allowing a through-going rupture to form, as at A-1 (Moore and Lockner, in preparation; see also Cox and Scholz, 1988). Fault-widening processes at B-1 have an added component of cracking subparallel to the shear fracture; these cracks are prominent alongside the shear in Figure 34.

TABLE 5.

Intragranular Cracks
[Length (μm) per square millimeter]

Orientation	WPS	A-1	A-2	A-3	A-4	A-5	B-1	B-2	B-3	C-1
0-9°	173	2379	2468	726	938	2034	4570	3651	1832	830
10-19°	183	1280	1388	722	706	1247	1563	1733	918	593
20-29°	154	681	1756	471	441	877	1594	1619	874	526
30-39°	158	889	1403	949	399	743	1954	1309	853	413
40-49°	148	1171	1197	661	422	1346	1097	1185	1300	450
50-59°	216	1283	1242	477	420	746	924	1041	826	353
60-69°	212	916	1156	330	322	419	394	480	516	373
70-79°	324	748	1023	709	371	334	577	405	548	407
80-89°	268	623	913	554	276	587	466	450	871	224
90-99°	241	1120	1267	450	191	549	729	597	360	379
100-109°	321	1056	999	339	599	502	1146	513	426	418
110-119°	213	812	1258	178	750	483	827	596	680	413
120-129°	286	963	2217	317	487	976	1115	792	490	586
130-139°	318	1921	3322	383	444	1529	2846	1610	1532	677
140-149°	79	2208	2963	447	713	2034	2532	1670	1270	442
150-159°	178	2297	3488	282	619	2236	2564	1091	1039	557
160-169°	176	3497	5029	688	734	1865	4286	2490	1998	823
170-179°	237	5096	4116	675	637	2700	4698	4982	3333	878
Sum	3885	28940	37205	9358	9469	21207	33882	26214	19666	9342

TABLE 6.

Total Crack Lengths
[Length (μm) per square millimeter]

Orientation	WPS	A-1	A-2	A-3	A-4	A-5	B-1	B-2	B-3	C-1
0-9°	273	3021	2989	1273	1315	2232	4857	3940	2002	1264
10-19°	425	1736	1711	973	1012	1793	1973	2039	1173	984
20-29°	326	915	1864	690	790	1468	1908	1934	1002	673
30-39°	246	1309	1780	1083	600	1084	2588	1655	937	820
40-49°	372	1465	1526	1048	563	2345	1459	1478	1584	824
50-59°	780	1782	1620	635	834	1070	1329	1833	942	634
60-69°	509	1319	1327	480	673	586	632	586	1013	472
70-79°	542	900	1542	833	624	529	735	498	751	735
80-89°	472	890	1213	883	632	808	630	702	1118	518
90-99°	625	1857	1680	826	416	908	977	1017	867	794
100-109°	477	1425	1258	718	959	775	1525	707	718	690
110-119°	547	1209	1432	608	1027	831	1263	799	879	710
120-129°	382	1092	2391	470	591	1325	1365	824	691	849
130-139°	537	2242	3642	535	670	1791	3227	2032	1693	837
140-149°	134	2446	3349	757	894	2327	2699	2080	1423	634
150-159°	252	2580	3930	509	986	2527	2805	1320	1229	816
160-169°	319	3909	5340	756	960	2135	4656	2821	2267	1002
170-179°	282	5724	4552	1111	1038	2923	4990	5244	3562	1087
Sum	7500	35821	43146	14188	14584	27457	39618	31509	23851	14343

TABLE 7.

Intragranular Cracks - Subdivided Images
[Length (μm) per square millimeter]

Orientation	A - 1			A - 2			B - 1	
	I	II	III	I	II	III	I	III
0-9°	2033	10432	1562	1507	3793	2518	5301	3912
10-19°	1170	3554	1060	1310	2005	988	1925	1238
20-29°	710	1047	607	2066	1880	1304	1808	1400
30-39°	1420	1709	347	1982	1458	695	2244	1694
40-49°	1244	2204	972	1160	1380	1093	1460	770
50-59°	684	1617	1724	984	1345	1458	737	1093
60-69°	569	2232	1019	1020	954	1473	397	392
70-79°	905	1275	550	780	1218	1146	706	461
80-89°	713	1041	494	847	1005	916	600	345
90-99°	1102	1487	1086	994	2210	830	992	493
100-109°	1521	2152	530	1042	1615	462	1531	799
110-119°	957	1064	660	1513	1649	655	1087	593
120-129°	1080	1167	841	2546	3174	1079	1489	779
130-139°	2541	4410	1079	3970	3698	2281	3090	2628
140-149°	3039	3025	1422	3340	3938	1758	2135	2888
150-159°	3491	2579	1290	3383	4552	2764	2646	2489
160-169°	2978	9146	3148	3376	7677	4823	3821	4705
170-179°	3543	25432	3584	3006	7231	2916	3951	3568
Sum	29700	75573	21975	34826	50782	29159	35920	30247

TABLE 8.

Total Crack Lengths - Subdivided Images
[Length (μm) per square millimeter]

Orientation	A - 1			A - 2			B - 1	
	I	II	III	I	II	III	I	III
0-9°	2700	10432	1998	1976	3911	3128	5568	4216
10-19°	1448	4827	1396	1452	2192	1256	2149	1815
20-29°	1072	1047	770	2196	1906	1422	2164	1675
30-39°	2138	1709	532	2181	1989	1034	2853	2350
40-49°	1546	2204	1261	1651	1577	1284	2138	849
50-59°	959	1988	2349	1355	1557	1954	1009	1616
60-69°	913	2232	1403	1243	1150	1575	771	508
70-79°	1031	1275	716	1035	1712	1869	891	595
80-89°	1109	1041	650	1172	1369	1135	672	592
90-99°	1909	3482	1515	1281	2451	1526	1084	881
100-109°	2117	3037	644	1429	1681	705	1831	1250
110-119°	1484	1501	935	1740	1861	739	1528	1025
120-129°	1098	2102	951	2624	3425	1280	1896	889
130-139°	2585	4410	1656	4081	3949	2876	3438	3038
140-149°	3421	3404	1488	3982	4006	1953	2338	3022
150-159°	3725	2579	1567	3681	5173	3219	2980	2646
160-169°	3459	9146	3390	3465	7709	5415	4294	4982
170-179°	4336	25707	3951	3189	7537	3576	4324	5588
Sum	37050	82123	27172	39733	55155	35946	41928	37537

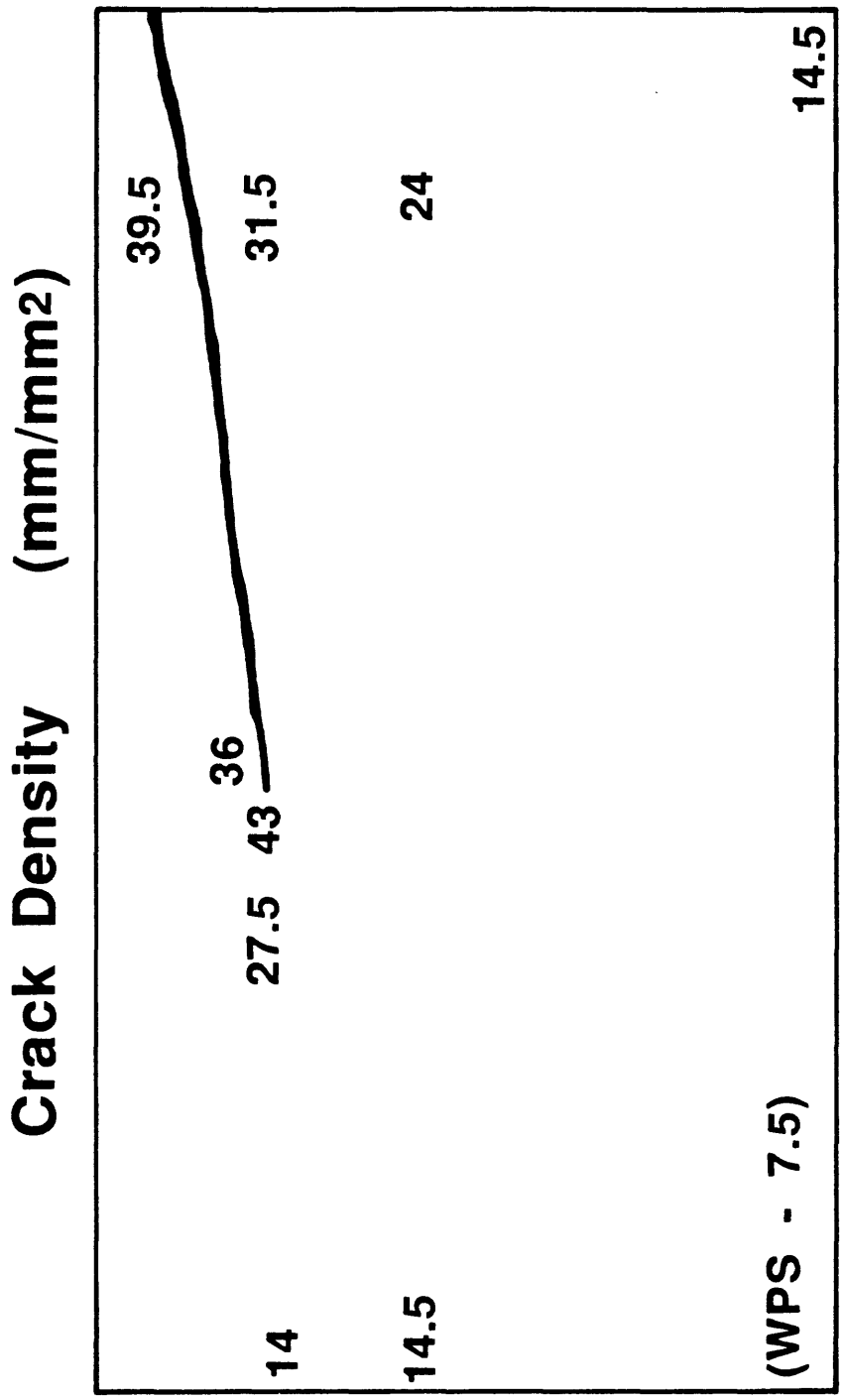

Figure 38. Sketch of part of the faulted cylinder, showing how the total crack density varies with position relative to the shear (see Figure 13). The crack density of the undeformed sample, WPS, is included in the lower left corner. Crack densities at the far-field locations are nearly identical and about double the density of WPS. The greatest density of cracking occurs in the process zone immediately adjacent to the fracture tip.

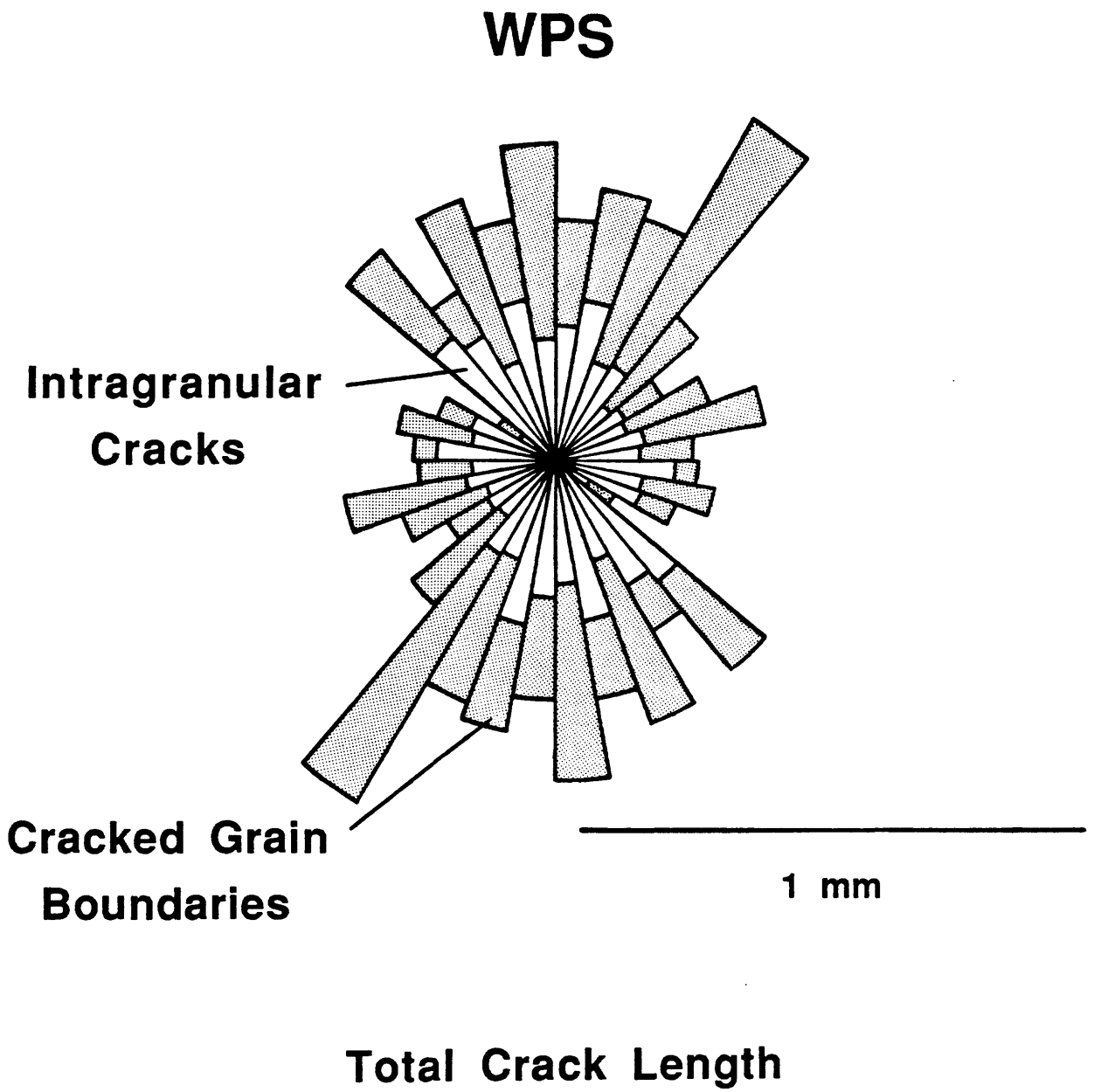

Figure 39. Rose diagram of total crack density in the undeformed sample WPS, showing the nearly equal contributions of intragranular and grain-boundary cracks. The same stippled pattern indicating grain-boundary crack lengths is also used in Figures 40-48.

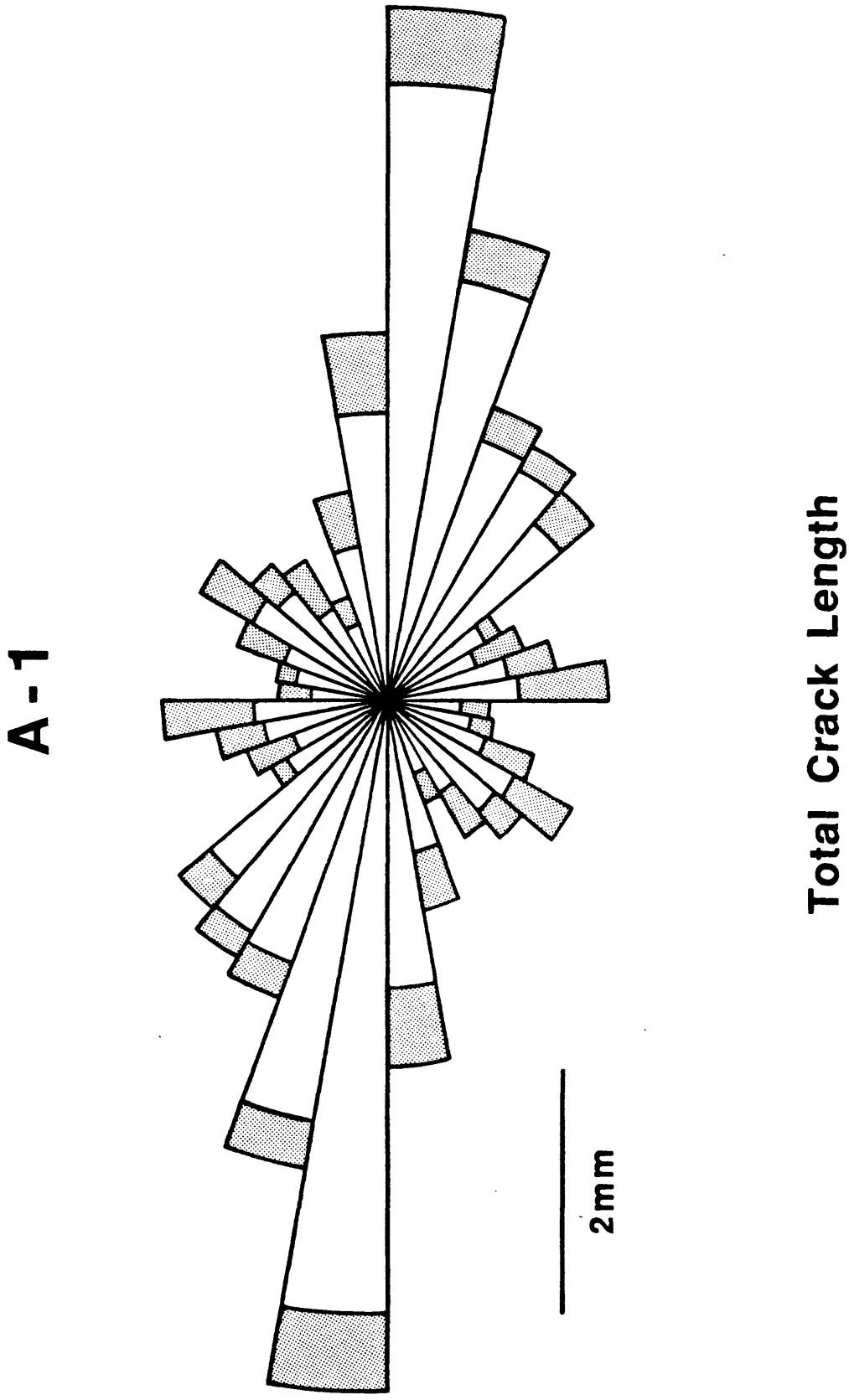

Figure 40a. Rose diagram of total crack density in image A-1 at the fracture tip. The maximum crack length is at 170-180°. Grain-boundary cracks make up a small proportion of the total crack length.

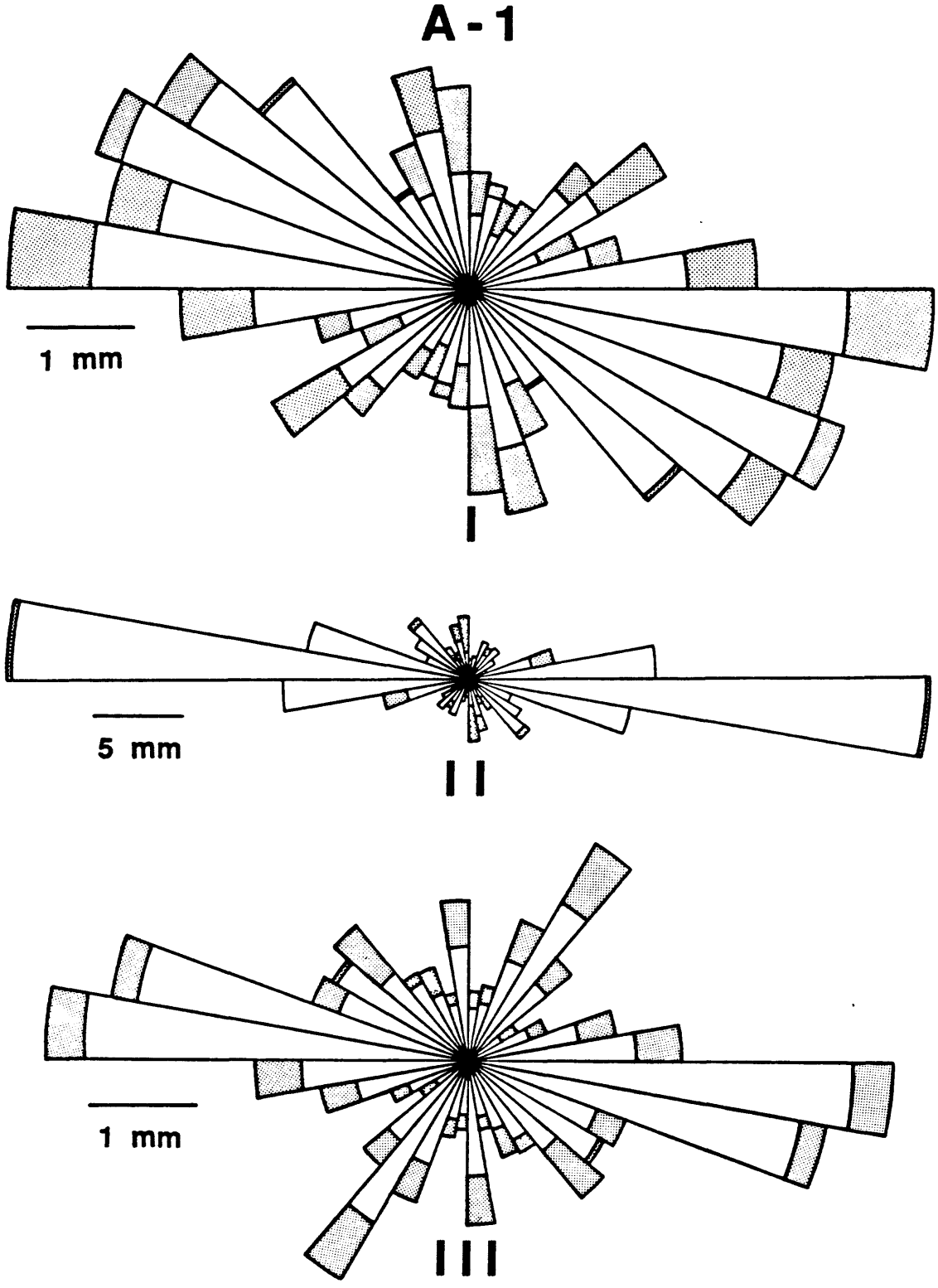

Figure 40b. Rose diagrams of the 3 subzones of A-1 (Figure 4b). The microcracks in zone II have a strong preferred orientation of 170-180°.

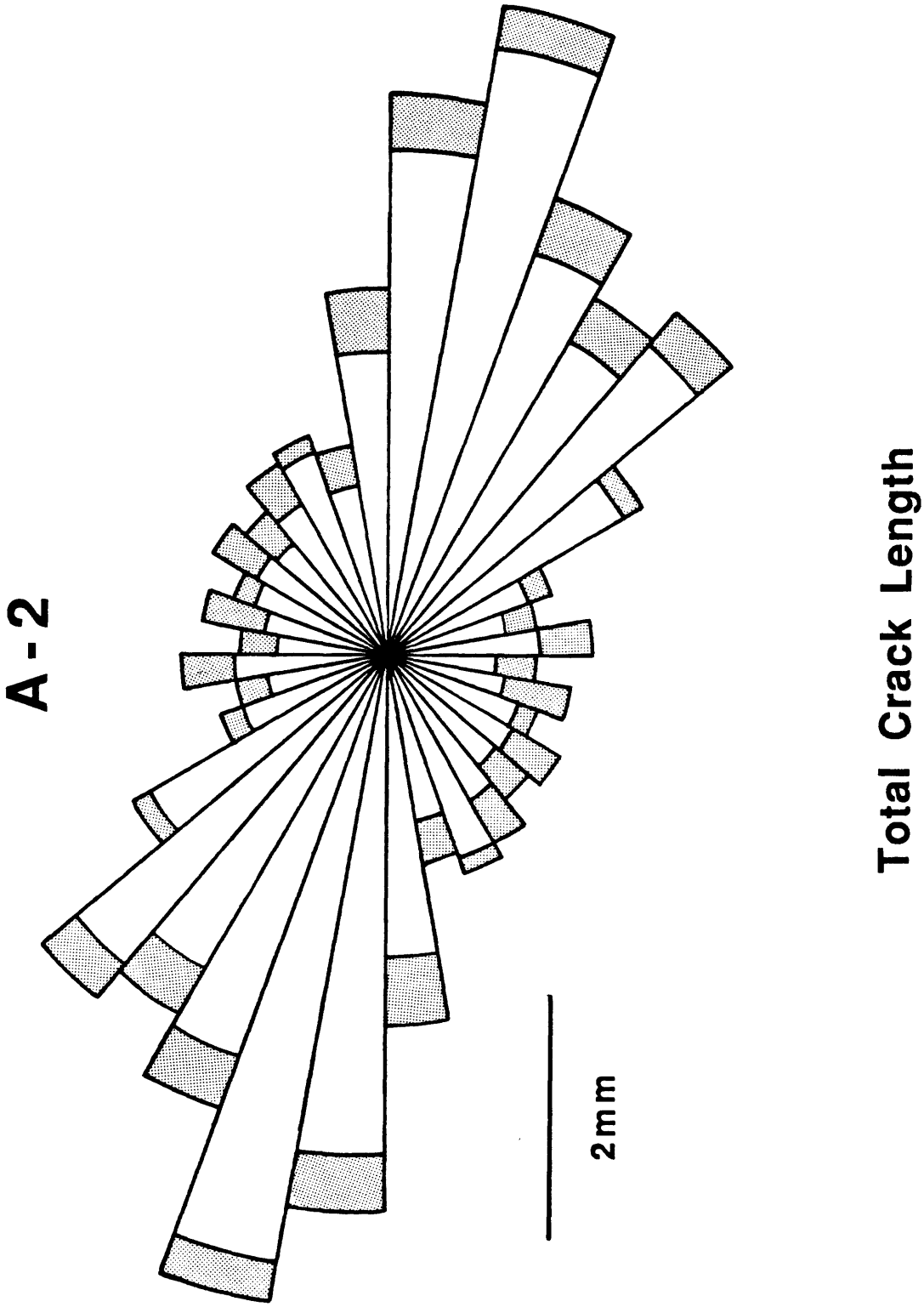

Figure 41a. Rose diagram of total crack density in image A-2.

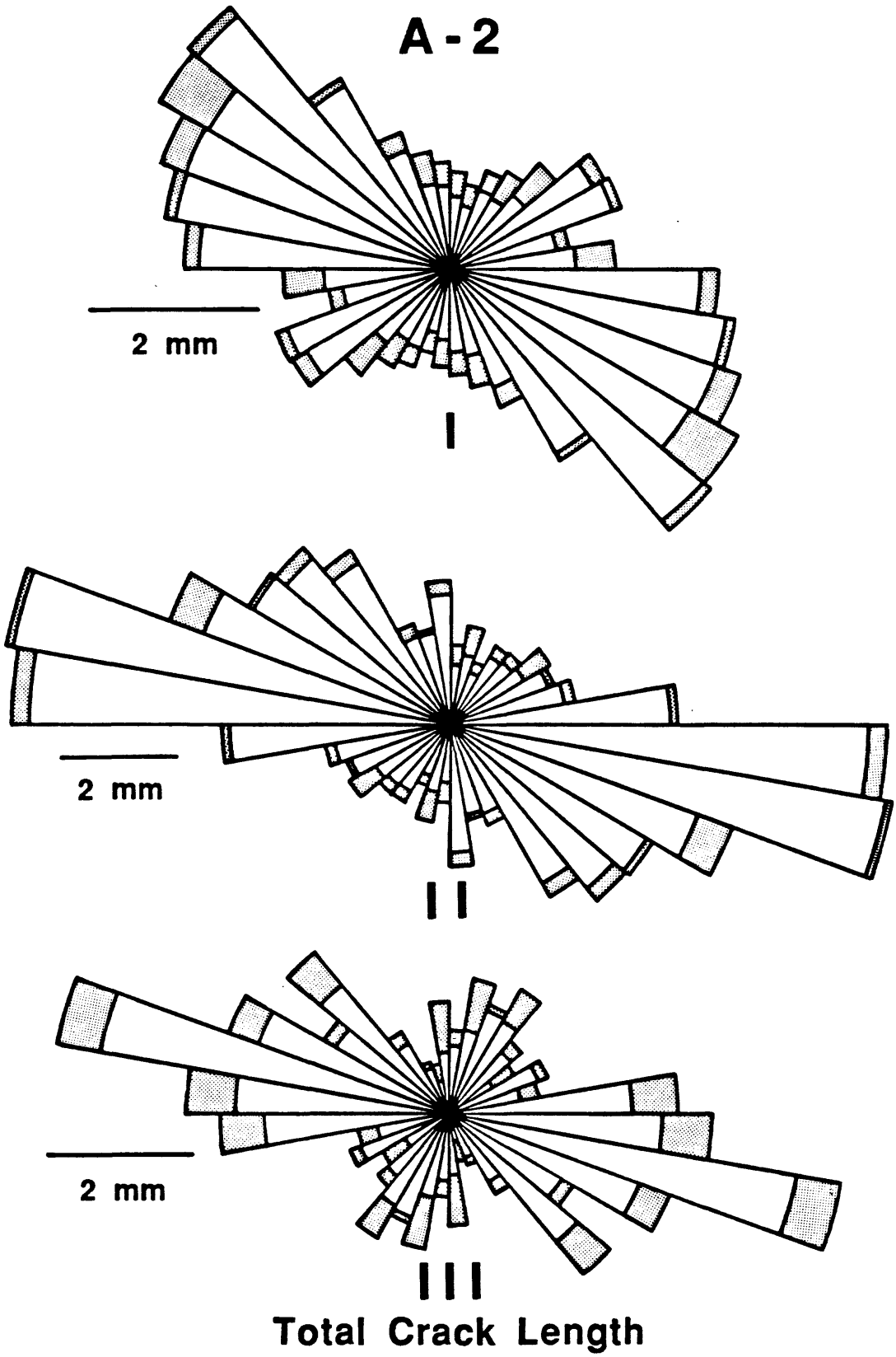

Figure 41b. Rose diagrams for the 3 subzones of A-2 (Figure 5b). The preferred crack orientations in all 3 diagrams are at an angle to the cylinder axis; the angle is largest for zone I and smallest for zone II.

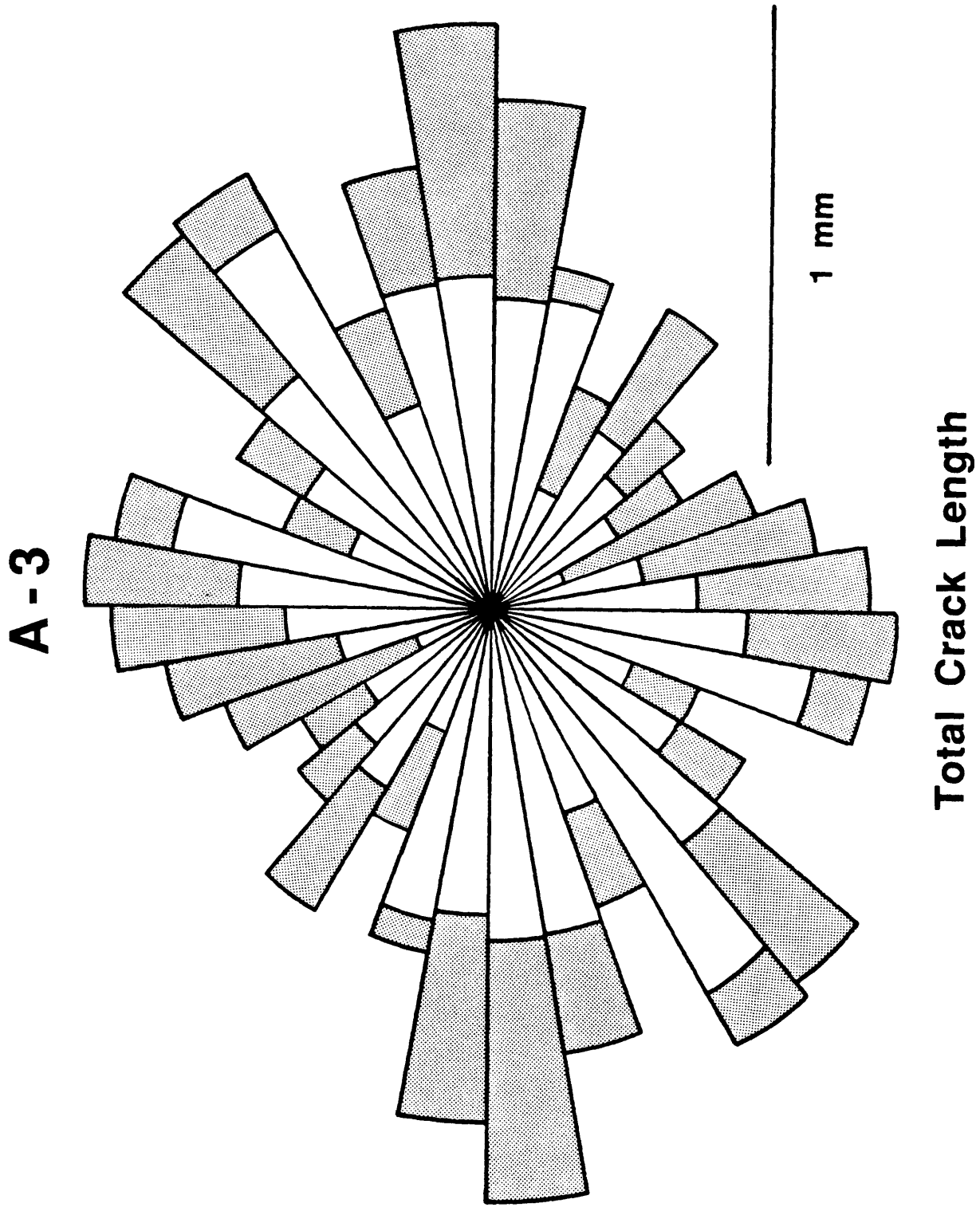

Figure 42. Rose diagram of total crack density in far-field image A-3. Grain-boundary cracks comprise about one-third the total crack length in this image.

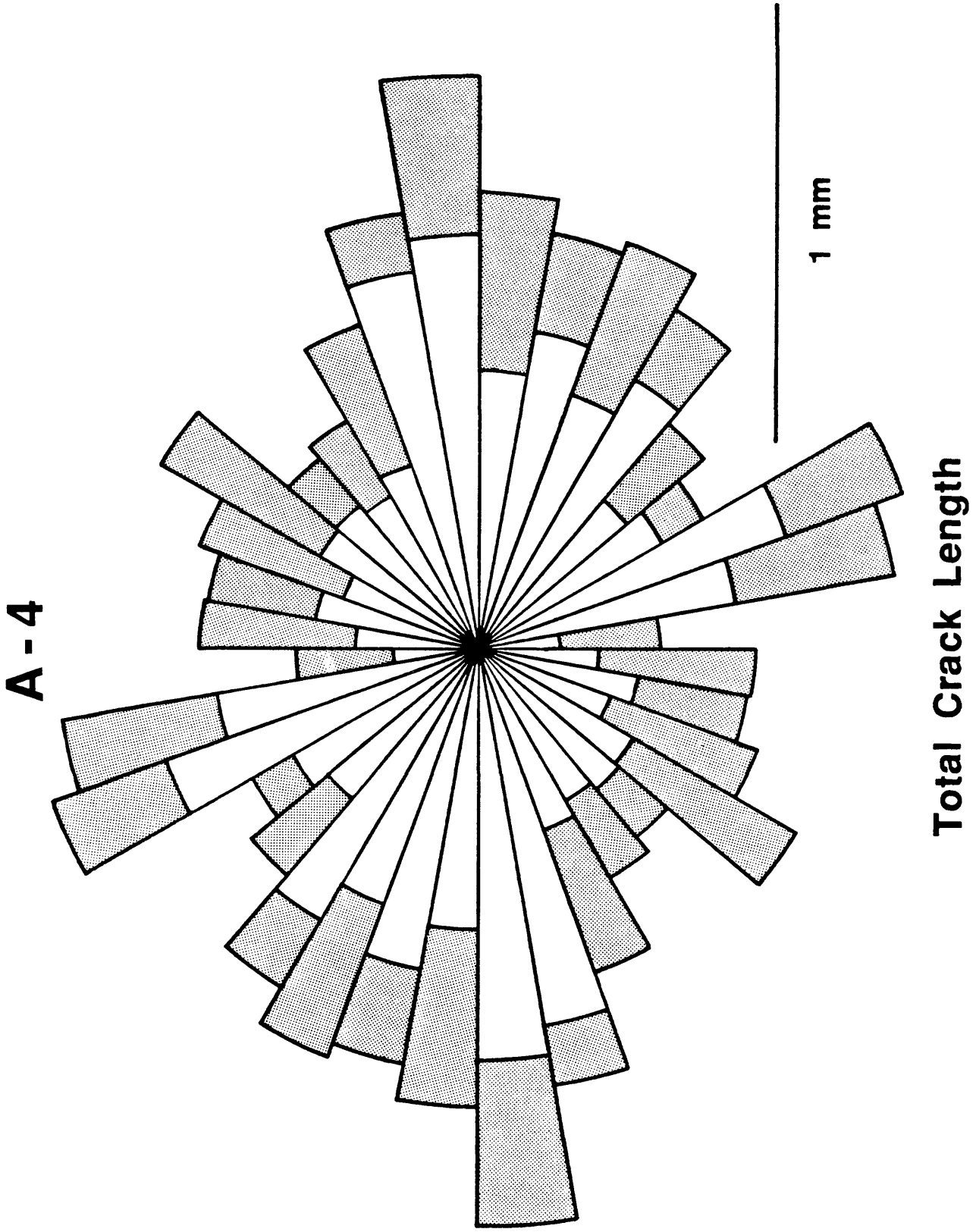

Figure 43. Rose diagram of total crack density for far-field image A-4. The cracks have a modest axial preferred orientation.

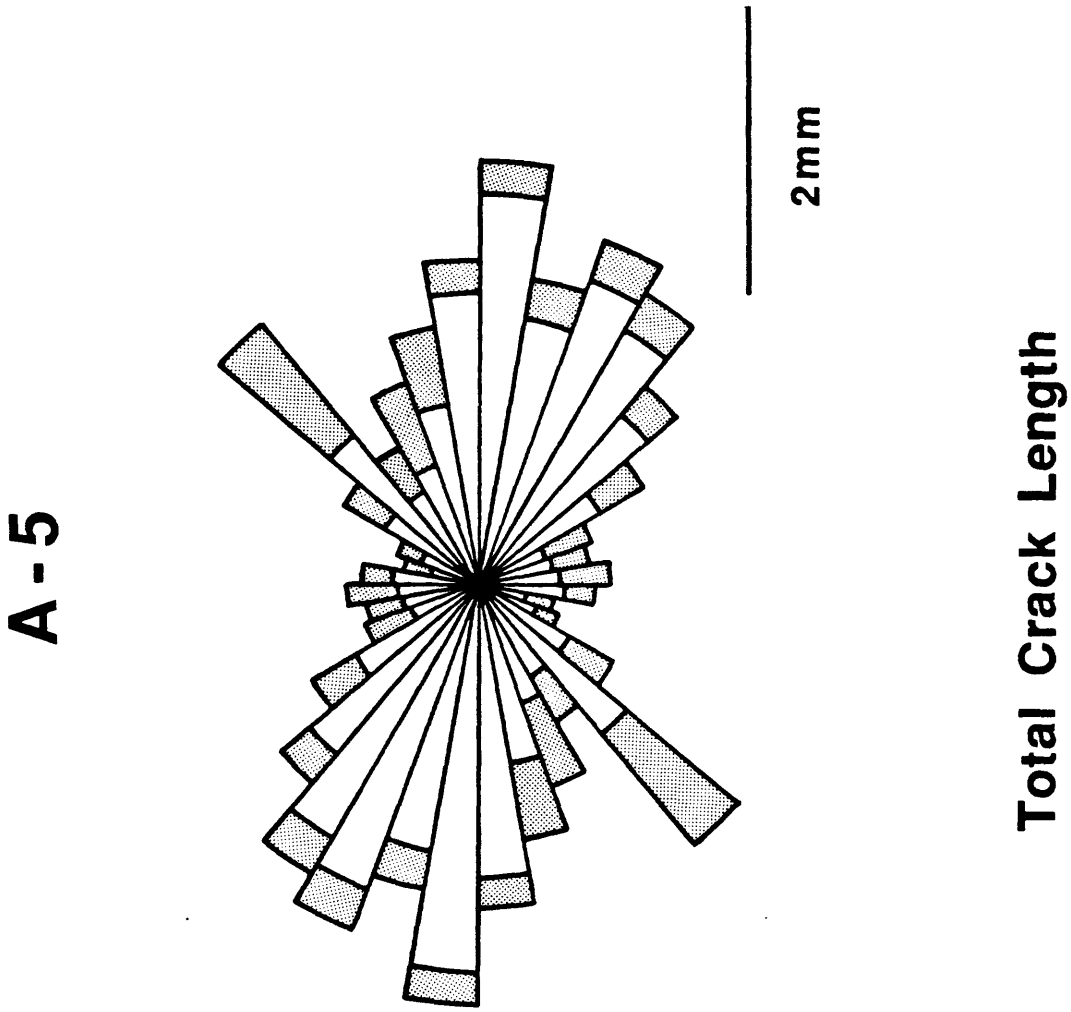

Figure 44. Rose diagram of total crack density for process-zone image A-5. Grain-boundary cracks comprise only a small proportion of the total crack length in this sample, although the igneous flow structure at 40-50° is clearly visible because of the large component of grain-boundary cracking. The preferred orientation of the cracks is centered at about 150°.

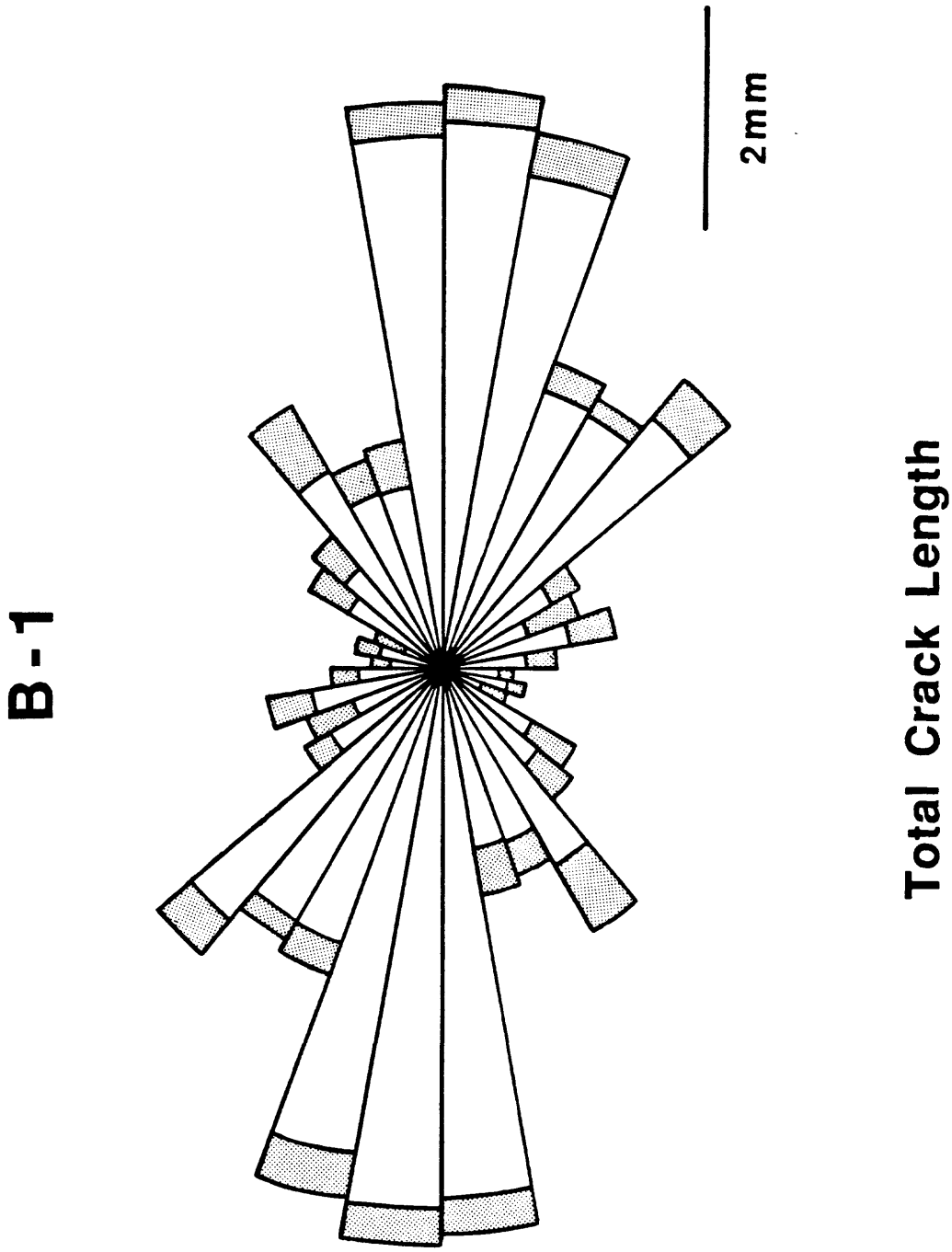

Figure 45a. Rose diagram of total crack density in image B-1, along the shear fracture. The alignment of the cracks is nearly axial.

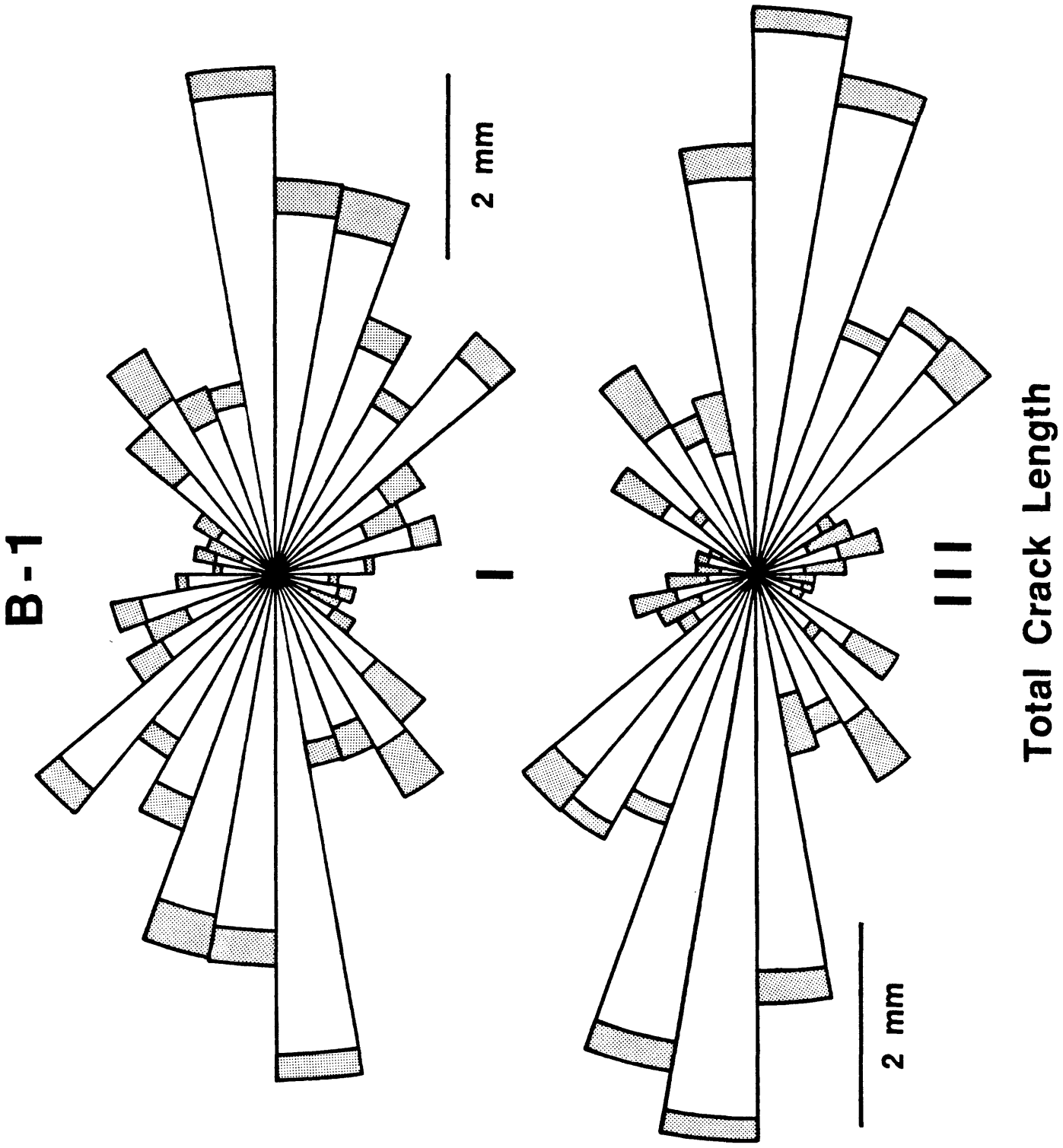

Figure 45b. Rose diagrams of total crack density for the subzones of image B-1 (Figure 9). The 2 diagrams are very similar overall.

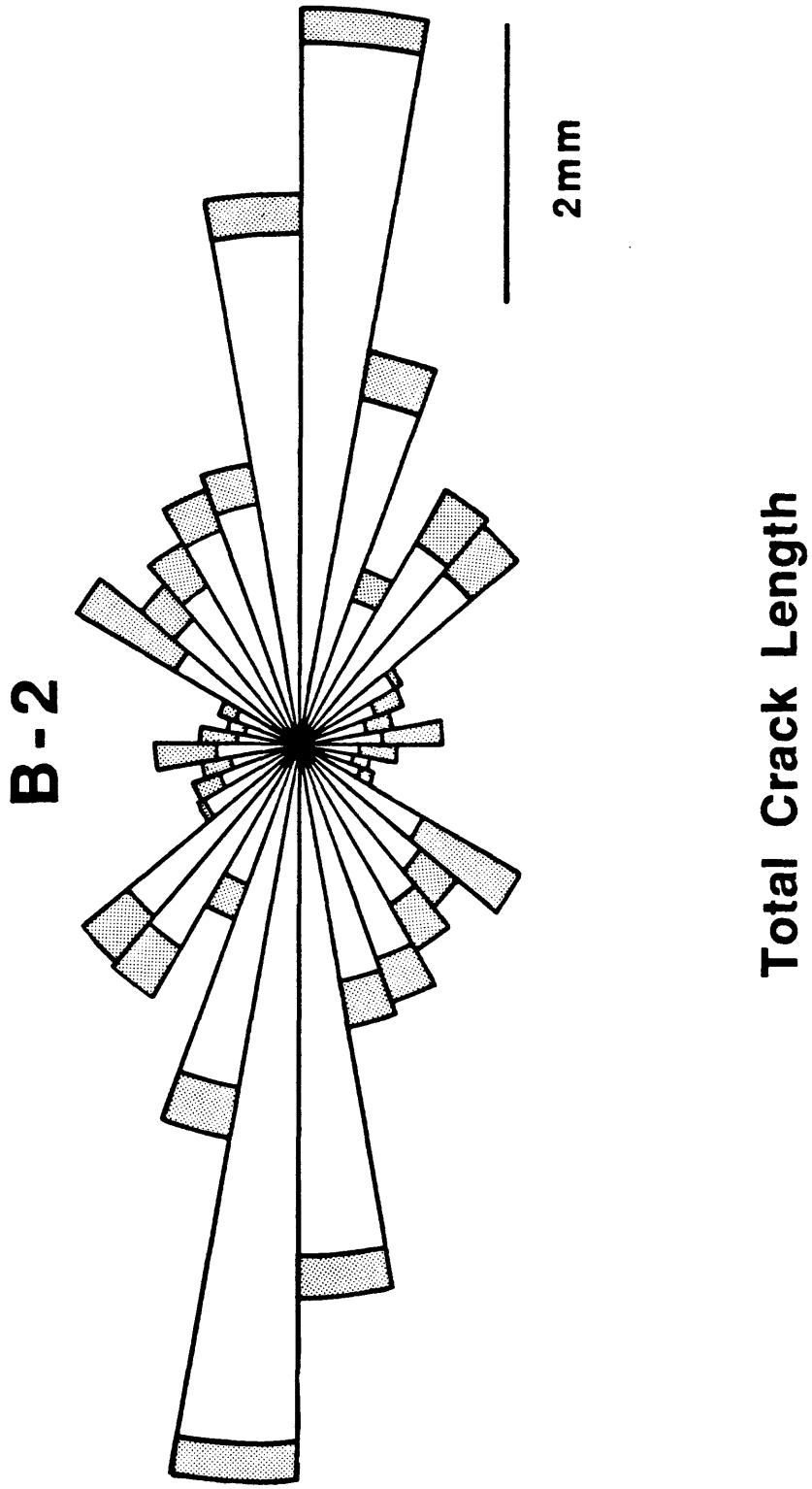

Figure 46. Rose diagram of total crack density for image B-2, close to the shear. The preferred crack orientation in this image is nearly axial, at 170-180°.

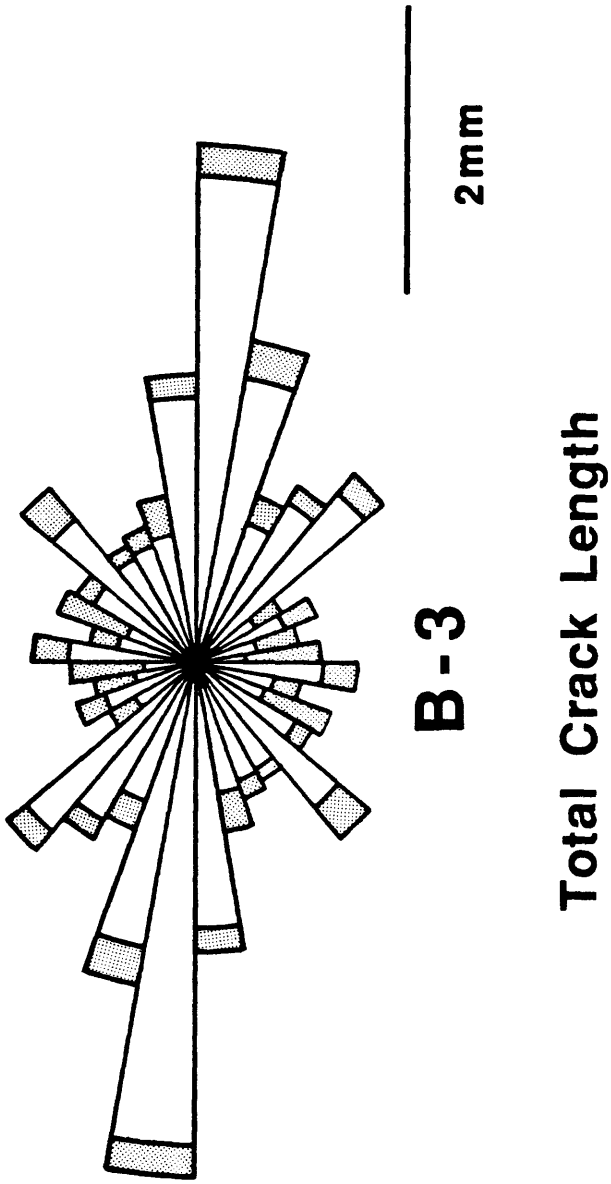

Figure 47. Rose diagram of total crack density in image B-3. The overall shape of the rose diagram is very close to that of B-2, but it encompasses less crack length.

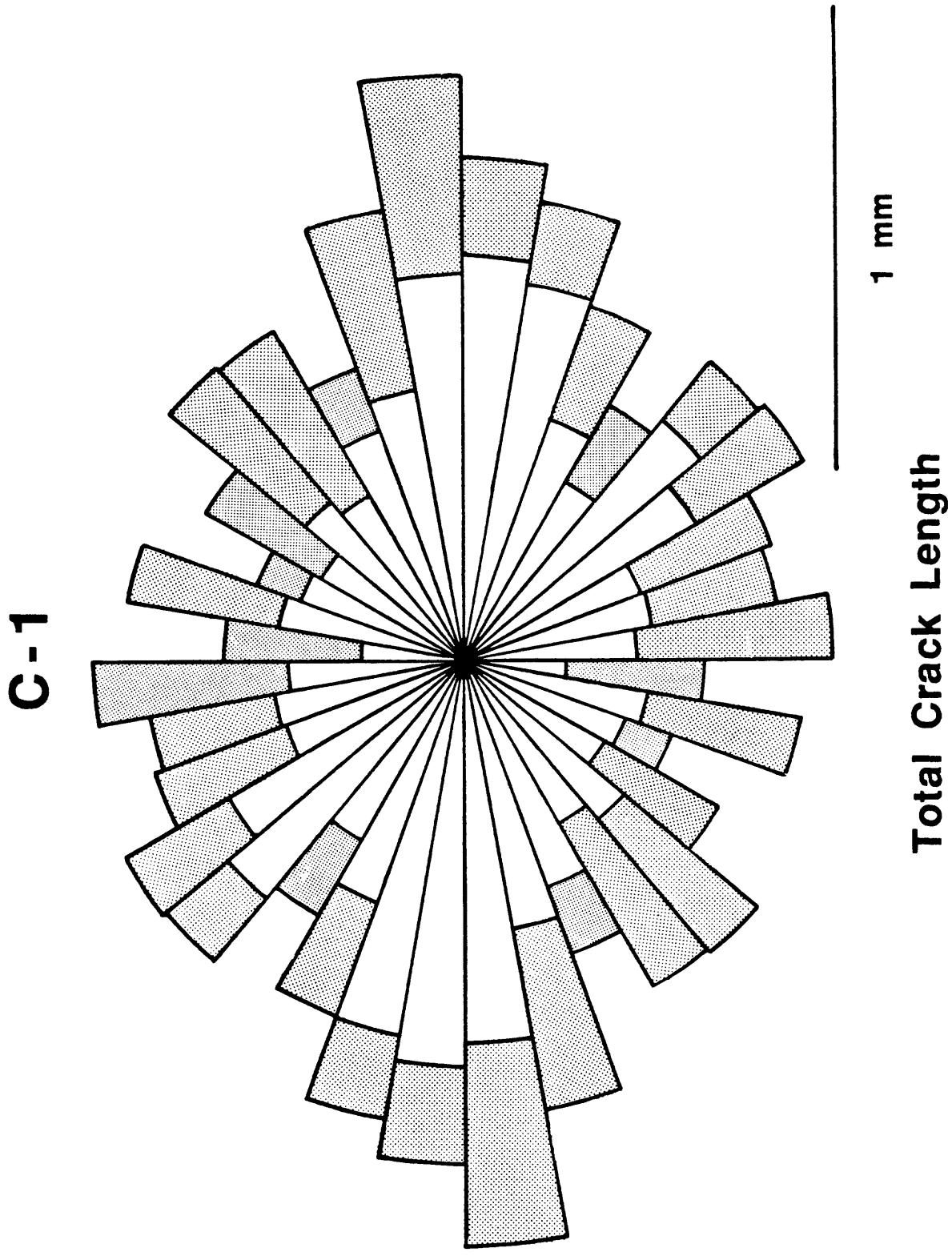

Figure 48. Rose diagram of total crack density for image C-1. Grain-boundary cracks are more evenly distributed by orientation than the intragranular cracks, which have a predominantly axial trend.

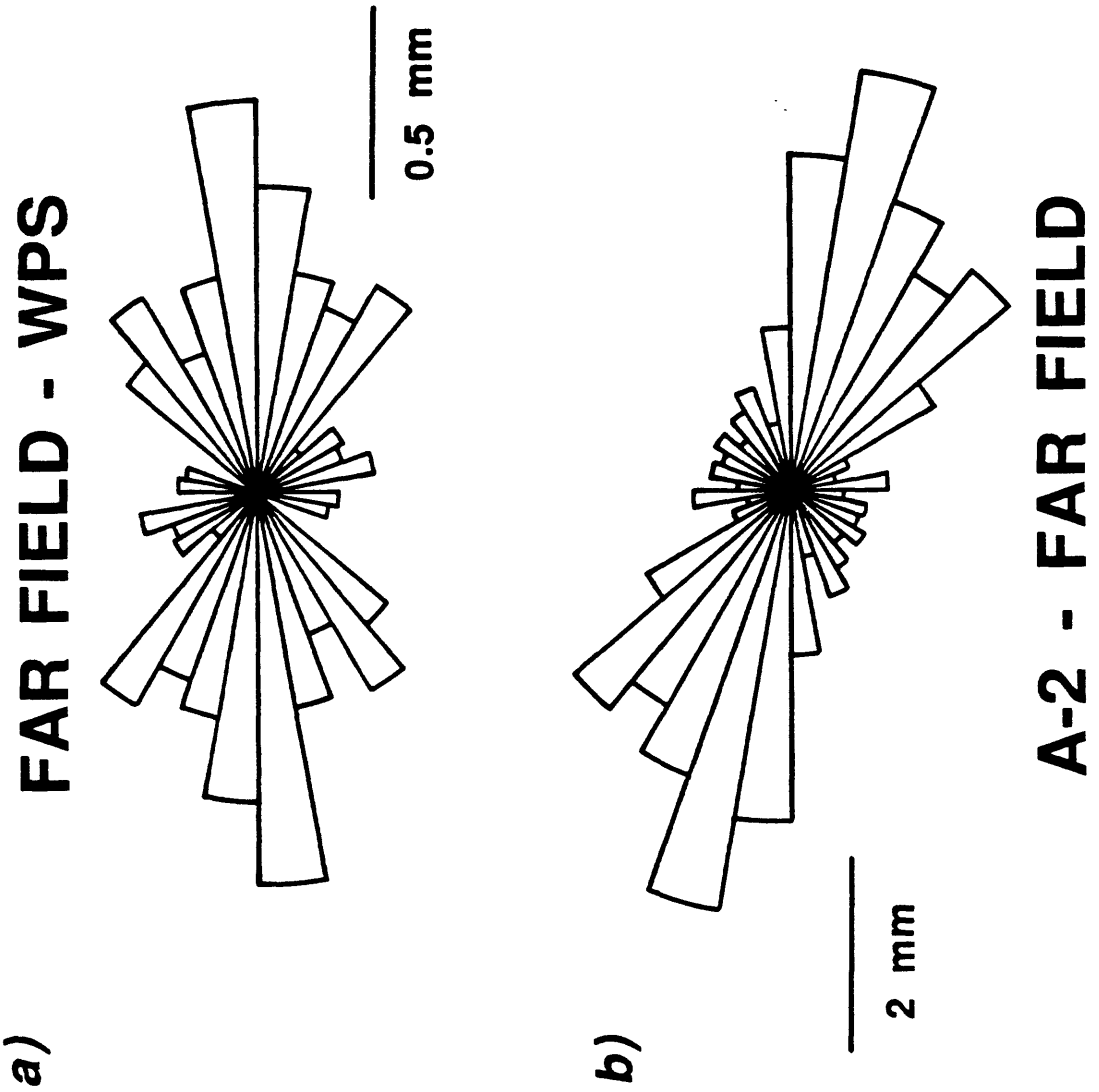

Figure 49. a). Rose diagram obtained by subtracting the total crack density of the undeformed sample WPS from representative far-field image A-3. The remaining cracks, considered to represent the stress-induced cracks formed prior to sample failure, have a predominantly axial trend consistent with the proportional orientations in Figure 2. b). Rose diagram obtained by subtracting the total crack density of far-field image A-3 from process-zone image A-2. The remaining cracks are the ones that were generated in the process zone; they have a preferred orientation centered at about 155°.

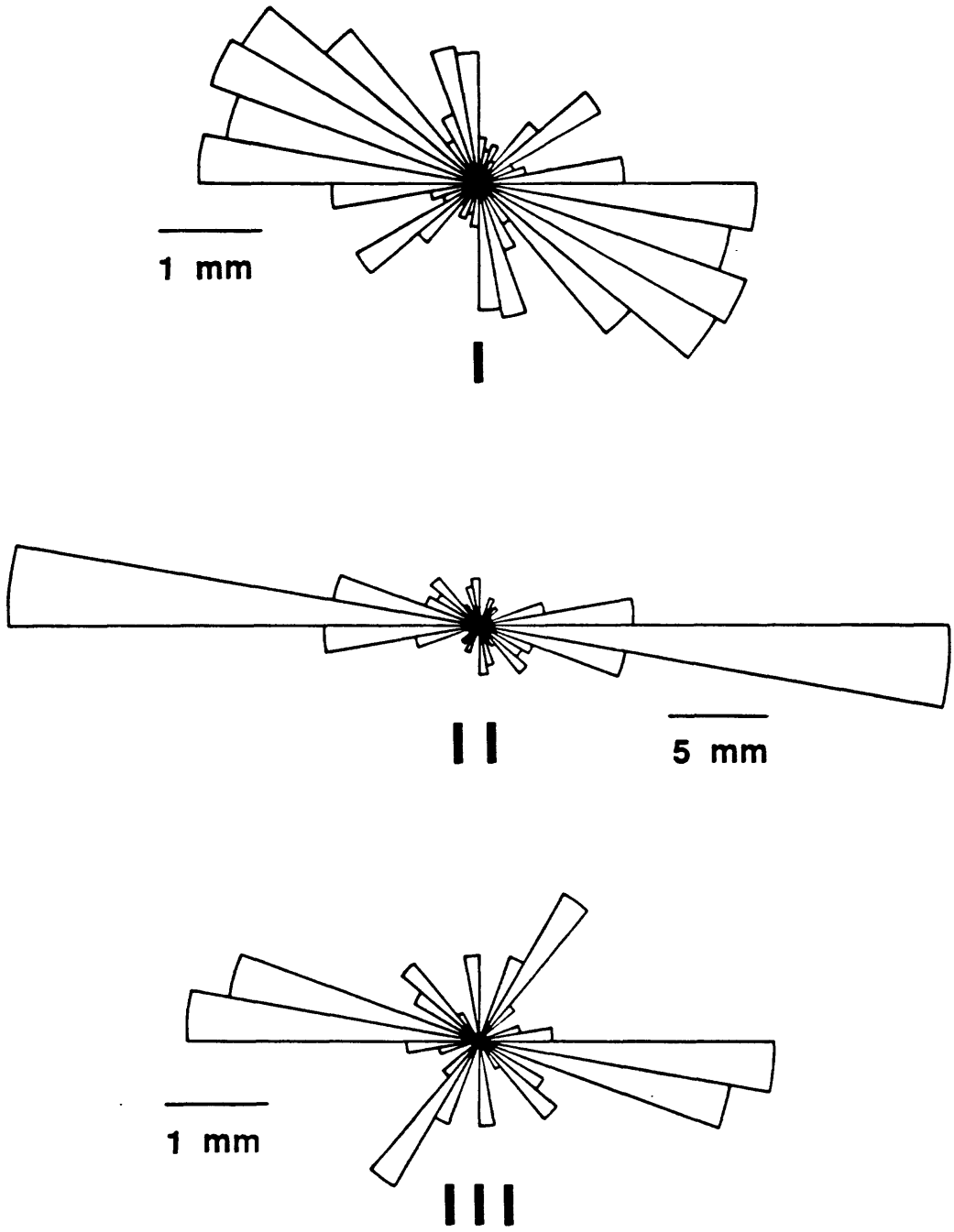

A-1 (subdivided) - Far Field

Figure 50. Rose diagrams obtained by subtracting the total crack lengths of the far-field image from those of the subzones of image A-1. The remaining cracks in zone II are mostly oriented in the range 170-180°. The cracks in zone I make the largest angles to the cylinder axis, on average, of the 3 zones. The cracks in zones I and III are principally holdovers from the previous position of the process zone.

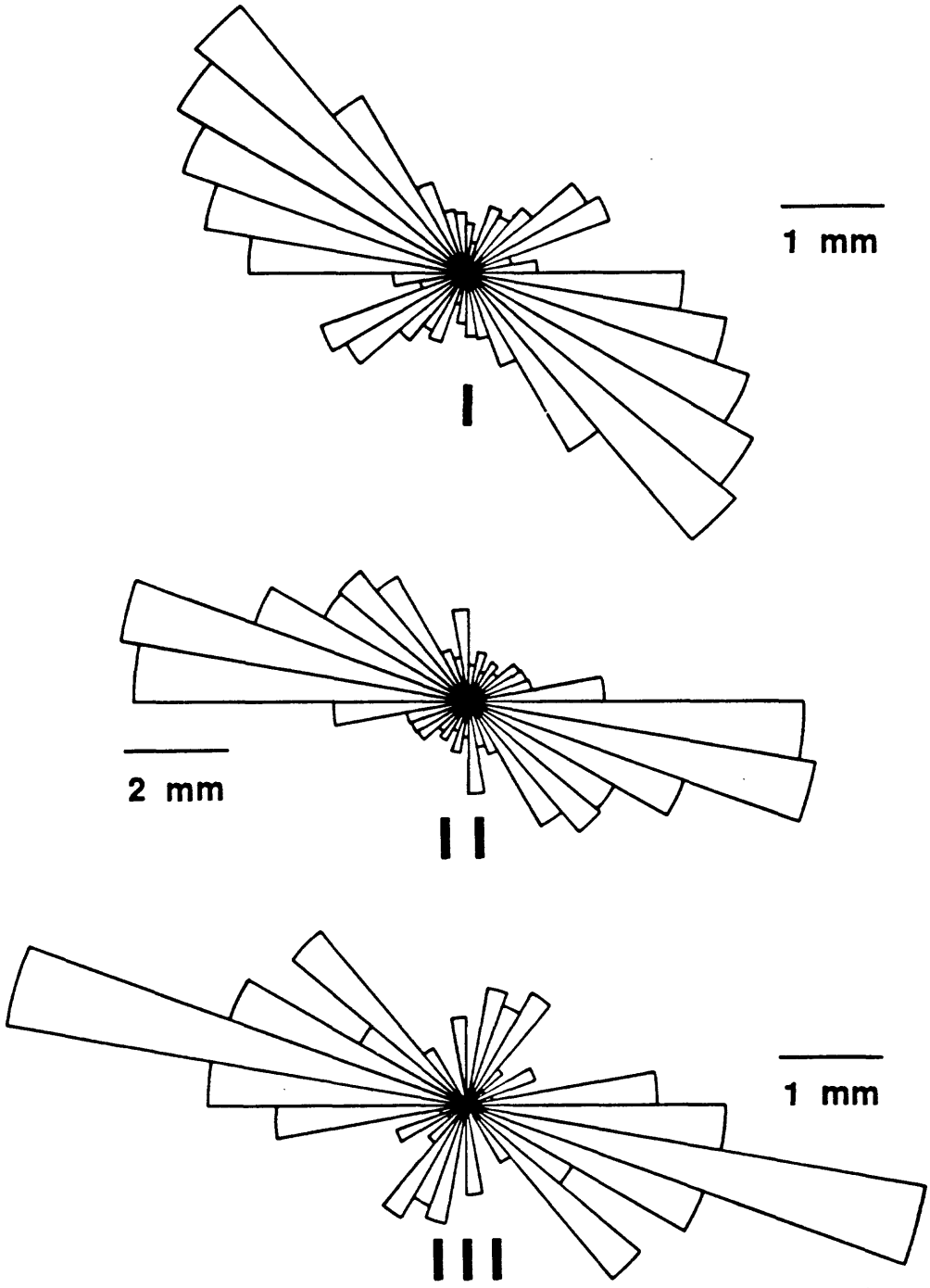

A-2 (subdivided) - Far Field

Figure 51. Rose diagram obtained by subtracting the total crack lengths of the far-field image from those of the subzones of image A-2. The cracks in zone I make the largest angles to the cylinder axis, on average, and those in zone II make the smallest angles.

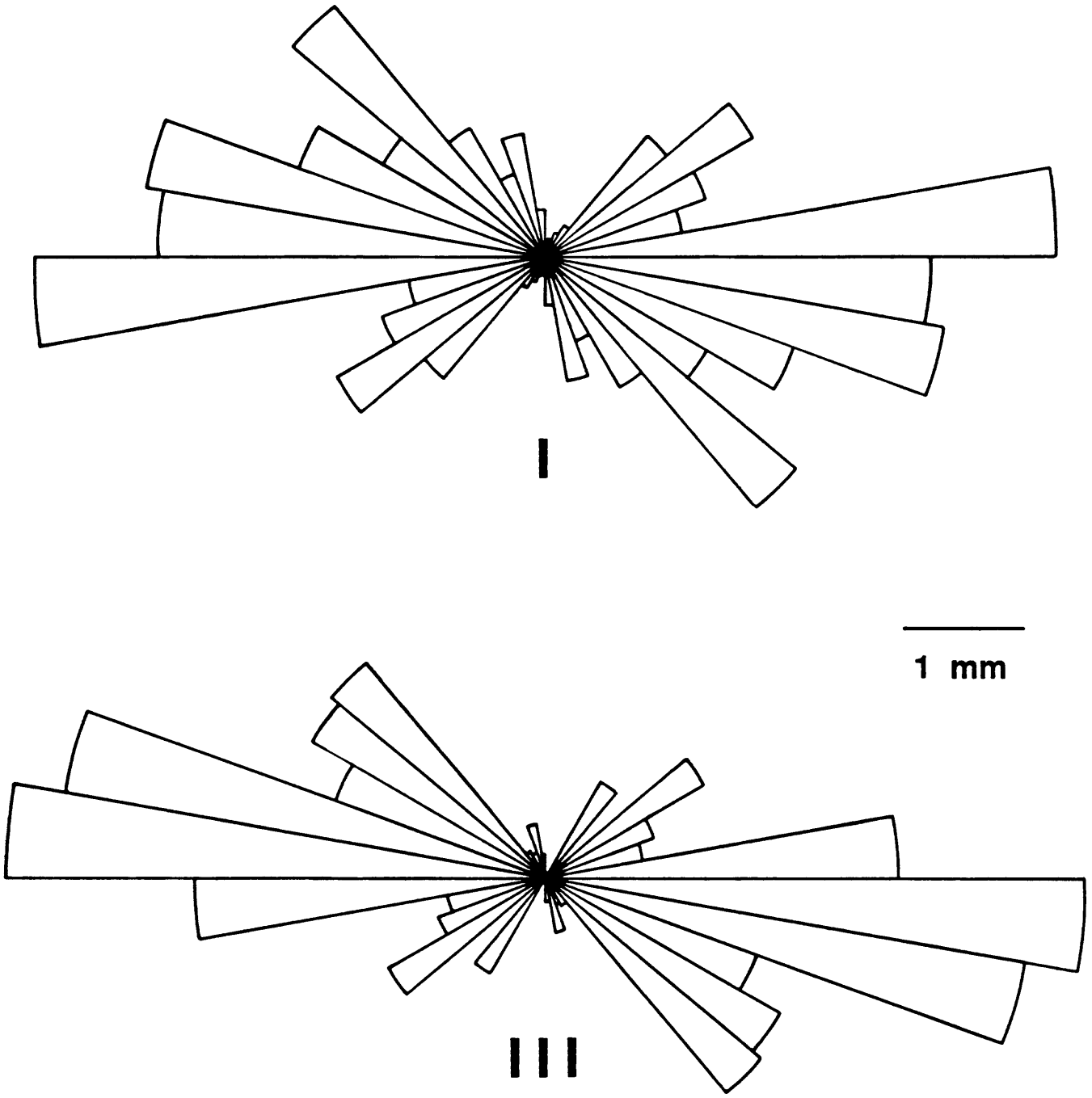

B-1 (subdivided) - Far Field

Figure 52. Rose diagrams obtained by subtracting the total crack lengths of the far-field image from those of the subzones of image B-1. The axes of both rose diagrams are at about 160-170°. Many of these cracks formed in association with widening and smoothing of the shear fracture.

MINERALOGICAL CONTROLS ON INTRAGRANULAR CRACKING

Variations in the intragranular crack densities of quartz, plagioclase, and K-feldspar in the stressed sample are plotted in Figures 53-55, respectively; values for the undeformed sample, WPS, are included in the lower left corner of each figure. As was found with the grain-boundary cracking, intragranular cracking in WPS is concentrated in quartz. The proportional differences in microcrack density in quartz and the feldspars decrease in the laboratory sample, but the relative order changes. In the far-field areas of the stressed sample (A-3, A-4, C-3), intragranular cracks are still concentrated in quartz, although the differences between quartz and the feldspars have diminished. In the near-field area, however, crack densities in K-feldspar commonly surpass those of quartz by 15-20%, whereas those in quartz and plagioclase are about the same, on average. The overall crack densities for a given mineral do vary somewhat from image to image.

Even the most intensely cracked sites contain areas of relatively low crack density. Comparison of the mineral and microcrack maps reveals that the density variations are correlated with specific crystals. For example, two quartz crystals in zone II of image A-2 (Figure 5b) contain only a few cracks concentrated around their edges (Figure 30), whereas the K-feldspar crystal that partly surrounds them is highly cracked. The orientation of a given crystal lattice relative to the stress field probably controls the extent to which it will crack and thereby accounts for the variable crack densities in Figures 53-55. The cleavage planes in the feldspars should render them particularly anisotropic with respect to stress-induced cracking (Wong, 1982), although the secondary alteration in plagioclase may somewhat reduce the effectiveness of cleavage cracking in that mineral (Moore and Lockner, in preparation).

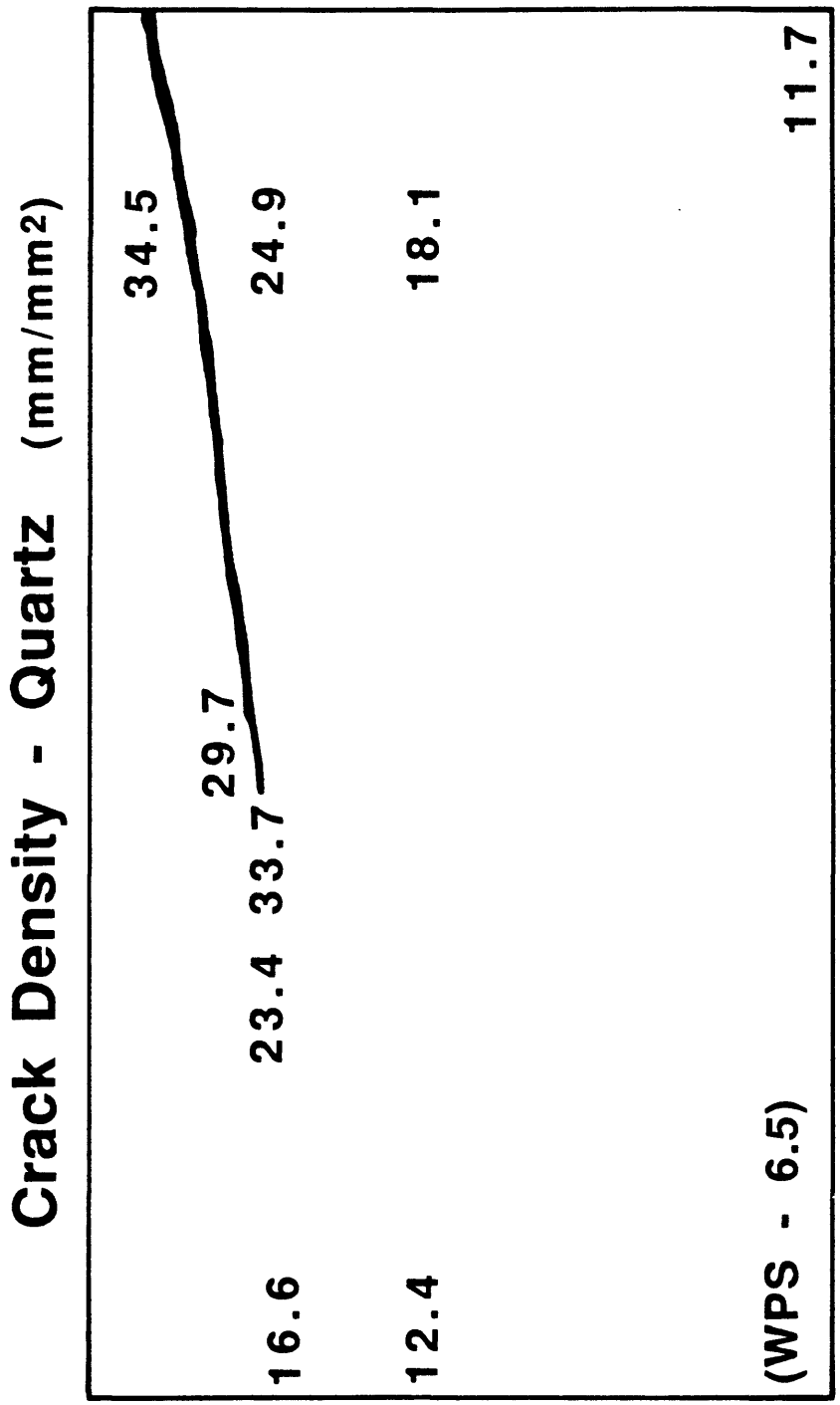

Figure 53. Sketch of part of the faulted cylinder, showing how the intragranular crack density of quartz varies with position around the shear. The value for the undeformed sample, WPS, is included in the lower left corner. The highest densities come from the images closest to the shear fracture.

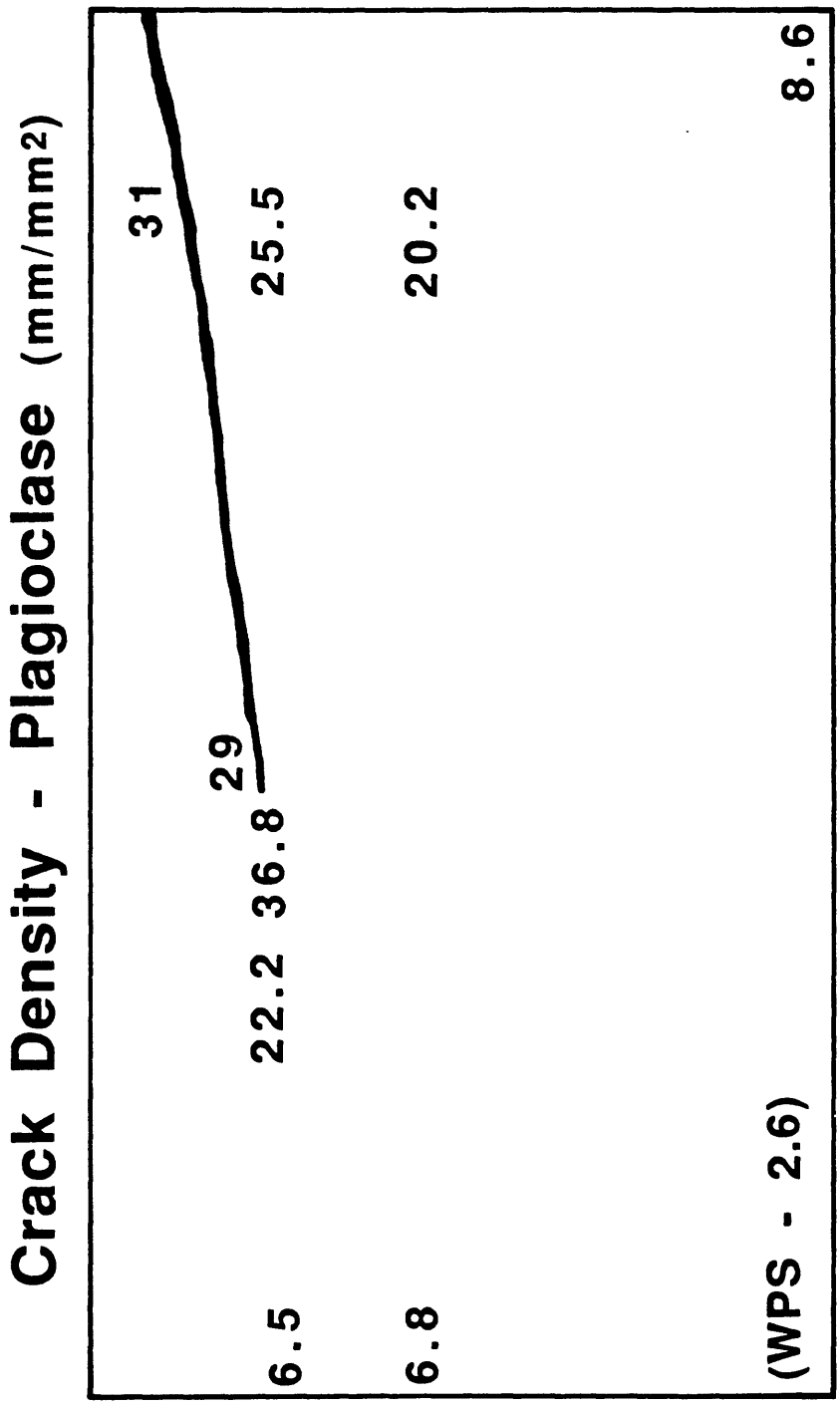

Figure 54. Variations in the intragranular crack density of plagioclase relative to position around the shear fracture.

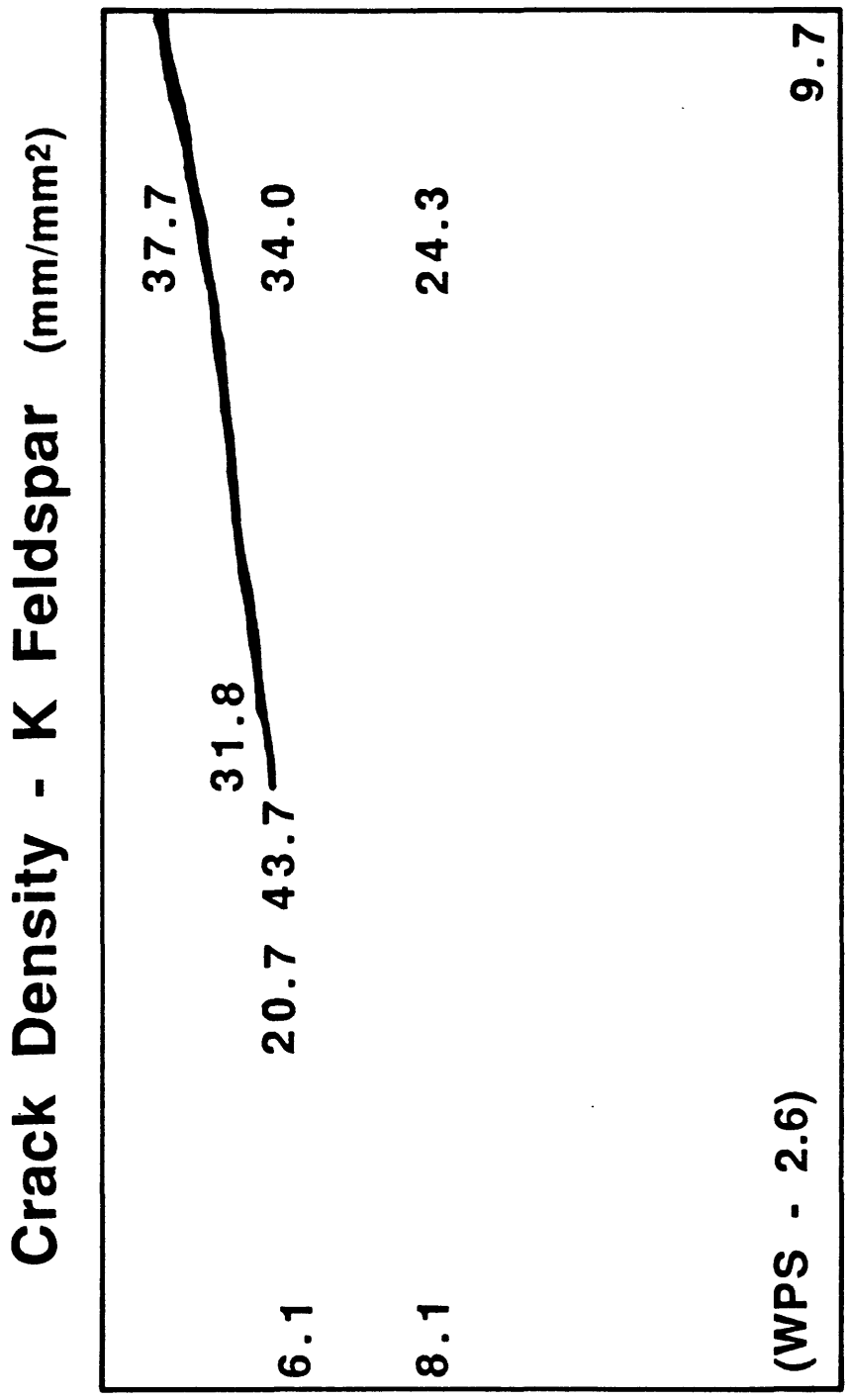

Figure 55. Variations in the intragranular crack density of K-feldspar relative to position around the shear fracture. The maximum of 43.7 mm/mm^2 is larger than was found for either quartz or plagioclase.

CRACK COUNTS

Most of the microcrack data in this study have been presented in terms of crack lengths per unit area. However, crack numbers are important to models of fracture initiation and growth (Madden, 1983; Lockner et al., 1992b). For this purpose, crack counts were also determined and sorted relative to lengths, following the groupings used by Madden (1983). The results are presented in Table 9, wherein N_X refers to microcracks oriented within 45° of the cylinder axis (0-45° and 135-180°) and N_Z represents cracks making angles larger than 45° (46-134°) to the cylinder axis.

Microcrack counts are a function of the assumptions made in defining what constitutes a single crack. In order to make these results as representative as possible, the counting conventions used in this study correspond overall to those of previous investigators (e.g., Hadley, 1976; Kranz, 1979, 1983). One slight difference is caused by the separation of grain-boundary and intragranular cracks, because a few grain-boundary cracks extend continuously into the interiors of adjoining crystals. However, the numbers of such composite cracks are so small that their separation does not noticeably affect the crack counts. Another potential problem concerns the microcracks that continue beyond the edges of the image, because the recorded lengths of such cracks are less than their true lengths. The possible extent of this effect was investigated for image A-5, whose crack density is roughly in the middle of the examined range. Various types of correction can be attempted for those cracks. One possibility is to remove the cut-off cracks from the counts and adjust the image area for their loss. The cut-off crack population is skewed towards the longer crack lengths relative to the total crack population, because of the numerous grain-boundary cracks that extend beyond the image boundaries. Removing these cracks will consequently have the greatest effect on the larger size categories: the 100-300 μm crack counts in A-5 are reduced by 10%, the 30-100 μm counts are 4-5% lower, and the 10-30 and 3-10 μm categories are reduced by less than 1%. Another possible correction is to measure the true lengths of the cut-off cracks and increase the sample area accordingly. This correction was not attempted, because the area to be measured lies outside the digitized image. Considered qualitatively, though, the adjustment should increase the various size categories by lesser percentages than the decreases observed with the other method, because not all the cut-off cracks would shift to a larger size category. Changes of at most 10% in the counts due to the cut-off cracks should have little effect on any model that uses the counts. Sample-to-sample variations will exceed this error, as indicated by the three far-field images (A-3, A-4, and C-1) in Table 9.

The crack counts made by Hadley (1976), as presented in Table 1 of Madden (1983), provide the only direct comparison to the crack counts in Table 9. Two parts of Madden's (1983) Table 1 require correction, however. The sample listed as being stressed to 65% of the failure strength was actually stressed nearly (~95%) to failure; it corresponds to sample T5 of Tapponnier and Brace (1976). This incorrect sample description was first noted by Wong (1985); Madden's table repeats the original error made by Hadley. The second correction involves the crack counts for the undeformed sample of Westerly. Hadley (1976) reports a crack density of 380/mm^2 for that sample, whereas the summed cracks in Madden's table come to 758/mm^2. The numbers in Madden's table lead to the incorrect conclusion that the unstressed sample is more highly cracked than the stressed sample T5. The crack numbers for the unstressed sample in Madden's table yield a mean crack length consistent with that reported by Hadley (1976), which suggests that the crack counts for the unstressed sample are uniformly high by a factor of 2. For comparison with WPS, the numbers presented by Madden for the unstressed sample should be divided by 2.

TABLE 9. Crack Counts

Whole Images

(area examined is 3mm^2 unless otherwise noted)

WPS

Crack Length	N_x	N_x/mm^2	N_z	N_z/mm^2
3-10μm	40	13.3	23	7.7
10-30	75	25.0	103	34.3
30-100	77	25.7	134	44.7
100-300	15	5.0	26	8.7
300-1000	1	0.3	3	1.0

A-1

Crack Length	N_x	N_x/mm^2	N_z	N_z/mm^2
3-10μm	290	96.7	322	107.3
10-30	840	280.0	675	225.0
30-100	608	202.7	299	99.7
100-300	123	41.0	45	15.0
300-1000	5	1.7	4	1.3

A-2

Crack Length	N_x	N_x/mm^2	N_z	N_z/mm^2
3-10μm	887	295.7	958	319.3
10-30	1406	468.7	946	315.3
30-100	737	245.7	359	119.7
100-300	101	33.7	30	10.0
300-1000	3	1.0	3	1.0

A-3

Crack Length	N_x	N_x/mm^2	N_z	N_z/mm^2
3-10μm	85	28.3	83	27.7
10-30	315	105.0	197	65.7
30-100	192	64.0	150	50.0
100-300	49	16.3	37	12.3
300-1000	1	0.3	4	1.3

A-4

Crack Length	N_x	N_x/mm^2	N_z	N_z/mm^2
3-10μm	69	23.0	62	20.7
10-30	217	72.3	161	53.7
30-100	177	59.0	128	42.7
100-300	60	20.0	50	16.7
300-1000	3	1.0	3	1.0

A-5

Crack Length	N_x	N_x/mm^2	N_z	N_z/mm^2
3-10μm	297	99.0	270	90.0
10-30	821	273.7	499	166.3
30-100	528	176.0	222	74.0
100-300	71	23.7	32	10.7
300-1000	1	0.3	- -	- -

B-1 (area= 2.62 mm^2)

Crack Length	N_x	N_x/mm^2	N_z	N_z/mm^2
3-10μm	87	33.2	144	55.0
10-30	610	232.8	453	172.9
30-100	648	247.3	246	93.9
100-300	178	67.9	43	16.4
300-1000	4	1.5	- -	- -

B-2

Crack Length	N_x	N_x/mm^2	N_z	N_z/mm^2
3-10μm	262	87.3	237	79.0
10-30	728	242.7	450	150.0
30-100	554	184.7	196	65.3
100-300	136	45.3	36	12.09
300-1000	8	2.7	3	1.0

B-3

Crack Length	N_x	N_x/mm^2	N_z	N_z/mm^2
3-10μm	85	28.3	80	26.7
10-30	586	195.3	360	120.0
30-100	429	143.0	207	69.0
100-300	71	23.7	49	16.3
300-1000	2	0.7	2	0.7

C-1

Crack Length	N_x	N_x/mm^2	N_z	N_z/mm^2
3-10μm	151	50.3	171	57.0
10-30	413	137.7	339	113.0
30-100	209	69.7	170	56.7
100-300	31	10.3	19	6.3
300-1000	1	0.3	- -	- -

Subdivided Images

(counts rounded off to whole numbers)

A-1 I (area = 1.25 mm^2)

Crack Length	N_x	N_x/mm^2	N_z	N_z/mm^2
3-10μm	156	125	171	137
10-30	420	336	332	265
30-100	275	220	133	107
100-300	42	34	14	11
300-1000	1	1	- -	- -

A-1 II (area = 0.21 mm^2)

Crack Length	N_x	N_x/mm^2	N_z	N_z/mm^2
3-10μm	21	100	40	191
10-30	102	487	84	401
30-100	83	393	35	166
100-300	34	163	3	15
300-1000	3	15	- -	- -

A-1 III (area = 1.54 mm^2)

Crack Length	N_x	N_x/mm^2	N_z	N_z/mm^2
3-10μm	113	73	111	72
10-30	318	206	259	168
30-100	251	163	131	85
100-300	47	30	28	18
300-1000	1	- -	4	2

A-2 I (area = 1.17 mm^2)

Crack Length	N_x	N_x/mm^2	N_z	N_z/mm^2
3-10μm	218	186	248	212
10-30	458	392	310	265
30-100	255	218	151	129
100-300	47	40	15	13
300-1000	2	2	2	2

A-2 II (area = 0.81 mm^2)

Crack Length	N_x	N_x/mm^2	N_z	N_z/mm^2
3-10μm	466	575	537	663
10-30	566	698	343	423
30-100	265	327	103	127
100-300	29	36	6	7
300-1000	- -	- -	1	1

A-2 III (area = 1.02 mm^2)

Crack Length	N_x	N_x/mm^2	N_z	N_z/mm^2
3-10μm	203	199	173	170
10-30	382	375	293	287
30-100	217	213	105	102
100-300	26	25	9	9
300-1000	- -	- -	1	1

B-1 I (area = 1.24 mm^2)

Crack Length	N_x	N_x/mm^2	N_z	N_z/mm^2
3-10μm	43	35	96	77
10-30	357	288	262	211
30-100	331	267	142	115
100-300	71	57	18	15
300-1000	3	2	- -	- -

B-1 III (area = 1.38 mm^2)

Crack Length	N_x	N_x/mm^2	N_z	N_z/mm^2
3-10μm	44	32	48	35
10-30	253	183	191	138
30-100	317	230	104	75
100-300	107	78	25	18
300-1000	1	1	- -	- -

Hadley's unstressed sample contained 160 cracks/mm^2 that are 3 μm or more in length, whereas WPS has 165/mm^2. These totals are very similar, although the distributions among the size categories are a little different. Hadley also found many cracks less than 3 μm in length in that sample, which nevertheless contribute very little to the total crack length. The sample (T5) stressed nearly to failure contained 372 cracks/mm^2, as reported by Madden (1983), or 420 ± 40 cracks/mm^2, as reported by Hadley (1976). Madden's numbers may represent the actual crack counts normalized to a unit sample area, whereas Hadley's may incorporate some error corrections. The far-field samples should be most comparable to T5, and the average crack density for the three images is 394/mm^2, which is consistent with Hadley's results. The individual far-field counts range from 310 to 501, illustrating the marked sample-to-sample variations. In sample T5, N_Z is slightly greater than N_X, whereas in the far-field images N_X is slightly greater than N_Z. Hadley examined a third sample that was stressed beyond its peak strength but not allowed to rupture. This sample yielded a crack count of 737/mm^2 (Madden) or 880 ± 90/mm^2 (Hadley), which comes closest to the counts for images B-2 (871/mm^2) and B-3 (613/mm^2). N_X significantly outnumbers N_Z in each of these latter three samples.

The crack densities for the various images in the stressed sample are plotted in Figure 56, and the crack-count and crack-length data are combined in Figure 57 to produce an average crack length for each image. Because the undeformed sample probably contains numerous cracks shorter than the 3 μm measuring limit of this study (Sprunt and Brace, 1974; Hadley, 1976; Madden, 1983), data for WPS are not included in Figures 56 and 57. The largest number of cracks and the minimum crack length are both found in the process zone directly in front of the fracture tip. After the fracture has passed through a particular position of the process zone, the microcracks that are now adjacent to the shear fracture increase their lengths. The microcrack maps in Figures 28-37 illustrate these trends. These results present a more complicated picture of stress-induced cracking in the granite than previous assertions that the average crack length increases in a rock subjected to laboratory stress tests (Sprunt and Brace, 1974; Hadley, 1976). The earlier investigations did not have data for process zones, however. The very large number of cracks counted at the lower measuring limit in image A-2 of the process zone suggests that even shorter microcracks may be present. The crack counts for the process zone, particularly that part of it closest to the fracture tip, should therefore be considered as minimum values.

SUMMARY

Open microcracks in undeformed Westerly granite are concentated within and along the edges of quartz crystals. Crack densities associated with plagioclase and K-feldspar in the undeformed rock are less than half the densities in quartz. These microcracks have a preferred orientation parallel to the horizontal direction at the quarry, and they probably formed as a result of uplift and exposure of the granite pluton. Applying an axial load to a granite cylinder under confining pressure leads to increases in crack density in all minerals and reduces the proportional differences in crack density between them. Close to the shear fracture that was generated in the stressed sample, microcracks tend to be somewhat more numerous in K-feldspar overall.

Despite continuing effects of mineralogy, the orientations of microcracks generated in the laboratory sample are consistent with tension cracks that formed under changing stress

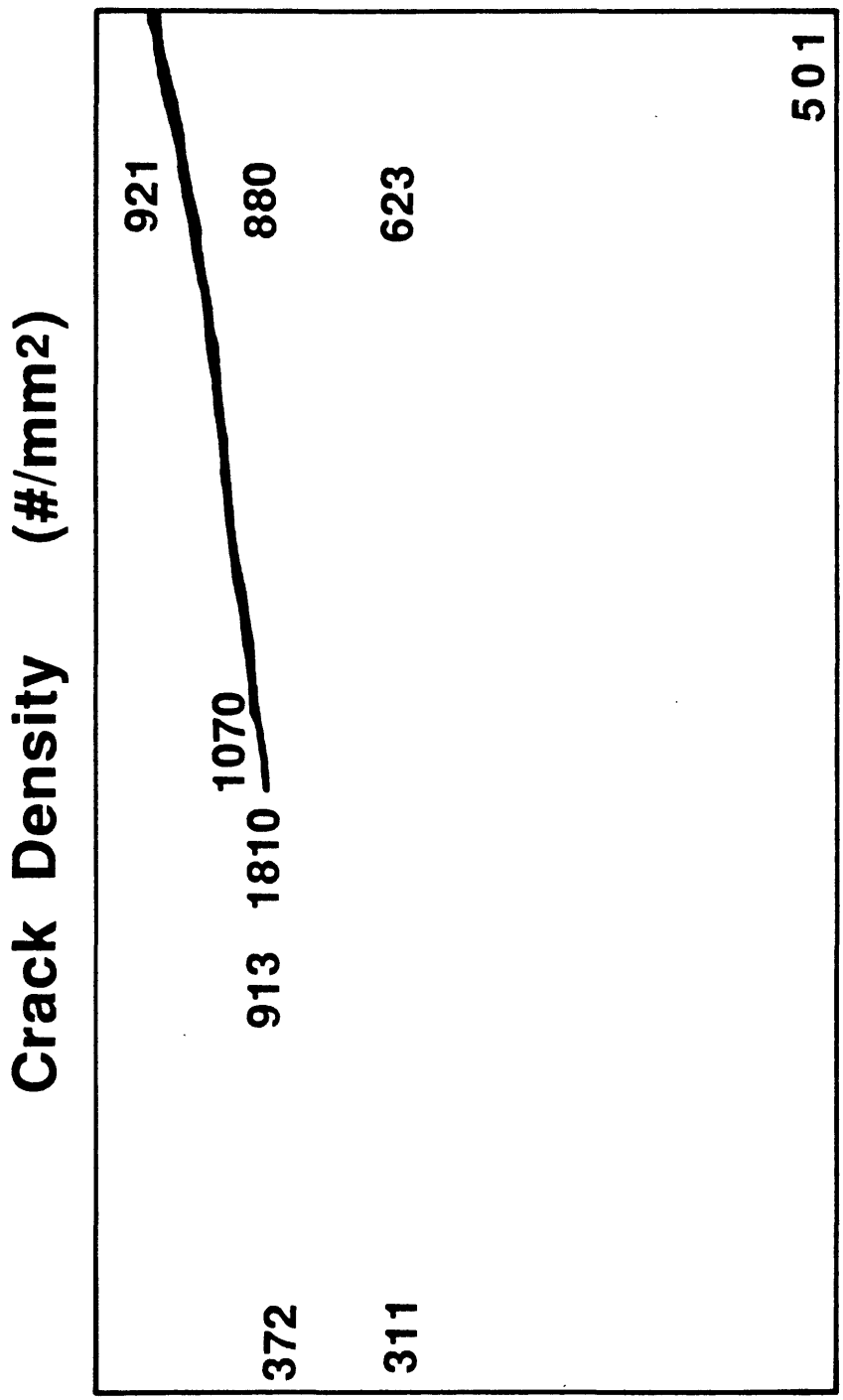

Figure 56. Crack densities expressed as numbers per unit area relative to position in the stressed sample. By far the largest number of cracks are in that part of the process zone closest to the shear fracture.

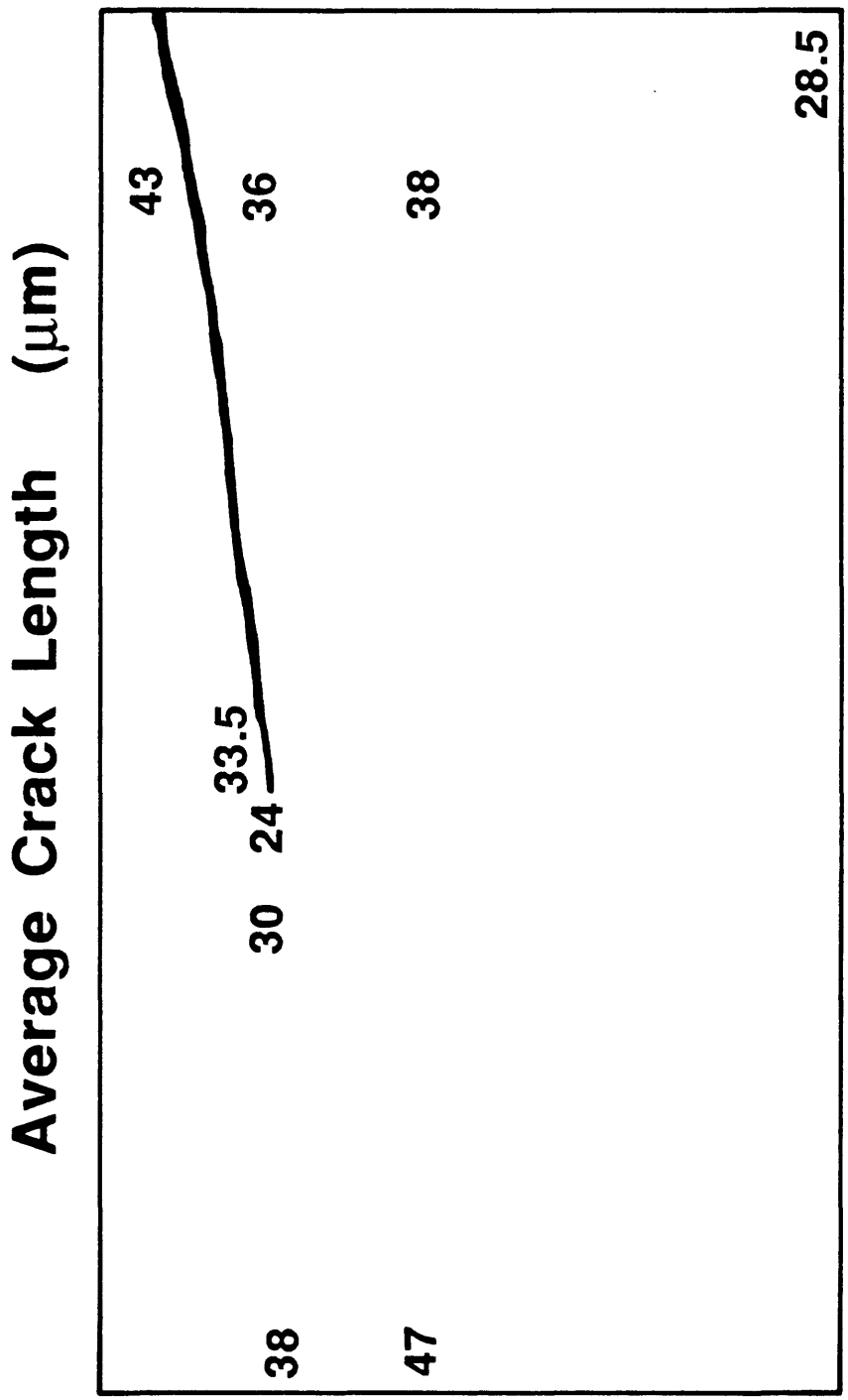

Figure 57. Average crack length at various positions around the shear fracture. The minimum crack length was found in the process zone adjacent to the fracture tip.

conditions, as predicted in models of faulting behavior. Prior to sample failure, new microcracks form throughout the cylinder, and they have a roughly axial orientation. Following initiation of the shear fracture, microcracking becomes concentrated in a process zone extending out in front of the fracture tip, and these microcracks are oriented, on average, at 30-40° to the fault strike. Some lower-angle microcracks concentrated along the future path of the shear may serve as linking cracks that help to form a through-going rupture. Along the fracture, fault-widening processes are associated with the production of microcracks that are subparallel to the strike of the fault.

REFERENCES

Chayes, F. (1950). On a distinction between late-magmatic and post-magmatic replacement reactions. American Journal of Science, 248(1), 22-36.

Cox, S. J. D., & Scholz, C. H. (1988). On the formation and growth of faults: an experimental study. Journal of Structural Geology, 10, 413-430.

Dale, T. N. (1923). The Commercial Granites of New England. U. S. Geological Survey Bulletin 738, 499 p.

Fredrich, J. T., & Wong, T.-f. (1986). Micromechanics of thermally induced cracking in three crustal rocks. Journal of Geophysical Research, 91(B12), 12743-12764.

Hadley, K. (1976). Comparison of calculated and observed crack densities and seismic velocities in Westerly granite. Journal of Geophysical Research, 81(20), 3484-3494.

Howarth, D. F. (1987). The effect of pre-existing microcavities on mechanical rock performance in sedimentary and crystalline rocks. International Journal of Rock Mechanics and Mining Sciences and Geomechanics Abstracts, 24(4), 223-233.

Kranz, R. L. (1979). Crack growth and development during creep of Barre granite. International Journal of Rock Mechanics and Mining Sciences and Geomechanics Abstracts, 16, 23-35.

Kranz, R. L. (1983). Microcracks in rocks: a review. In M. Friedman & M. N. Toksöz (Eds.), Continental Tectonics: Structure, Kinematics, and Dynamics. Tectonophysics, 100, 449-480.

Lockner, D. A., Byerlee, J. D., Kuksenko, V., Ponomarev, A., & Sidorin, A. (1992a). Observations of quasi-static fault growth from acoustic emissions. In B. Evans & T.-f. Wong (Eds.), Fault Mechanics and transport Properties of Rocks. San Diego: Academic Press, 3-31.

Lockner, D. A., Moore, D. E., & Reches, Z. (1992b). Microcrack interaction leading to shear fracture. In J. R. Tillerson & W. R. Wawersik (Eds.), 33rd U. S. Symposium on Rock Mechanics, 807-816.

Madden, T. H. (1983). Microcrack connectivity in rocks: a renormalization group approach to the critical phenomena of conduction and failure in crystalline rocks. Journal of Geophysical Research, 88(B1), 585-592.

Moore, D. E., Morrow, C. A., & Byerlee, J. D. (1983). Chemical reactions accompanying fluid flow through granite held in a temperature gradient. Geochimica et Cosmochimica Acta, 47, 445-453.

Moore, D. E., Morrow, C. A., & Byerlee, J. D. (1987). Fluid-rock interaction and fracture development in 'crystalline' rock types. U. S. Geological Survey Open-File Report, 87-279, 53 p.

Moore, D. E., & Lockner, D. A. (1993). The role of microcracks in shear-fracture propagation in granite. Journal of Structural Geology, in preparation.

Peng, S., & Johnson, A. M. (1972). Crack growth and faulting in cylindrical specimens of Chelmsford granite. International Journal of Rock Mechanics and Mining Sciences and Geomechanics Abstracts, 9, 37-86.

Pollard, D. D., & Segall, P. (1987). Theoretical Displacements and Stresses near Fractures in Rock: with Application to Faults, Joints, Veins, Dikes, and Solution Surfaces. In B. K. Atkinson (Ed.), Fracture mechanics of Rock. London: Academic Press, 277-349.

Sprunt, E. S., & Brace, W. F. (1974). Direct observation of microcracks in crystalline rocks. International Journal of Rock Mechanics and Mining Sciences and Geomechanical Abstracts, 11, 139-150.

Tapponnier, P., & Brace, W. F. (1976). Development of stress-induced microcracks in Westerly granite. International Journal of Rock Mechanics and Mining Sciences and Geomechanical Abstracts, 13, 103-112.

Wong, T.-F. (1982). Micromechanics of faulting in Westerly granite. International Journal of Rock Mechanics and Mining Sciences and Geomechanical Abstracts, 19, 49-64.

Wong, T.-f. (1985). Geometric probability approach to the characterization and analysis of microcracking in rocks. Mechanics of Materials, 4, 261-276.